

GEOLOGICAL MAPPING IN NORTHWEST BHUTAN
USING ASTER REMOTE SENSING DATA

Tara Muth

Submitted in Partial Fulfillment of the Requirements
For Degree of Bachelor of Sciences, Honours
Department of Earth Sciences
Dalhousie University, Halifax, Nova Scotia
March 2008



**DALHOUSIE
UNIVERSITY**

Inspiring Minds

Department of Earth Sciences

Halifax, Nova Scotia

Canada B3H 4J1

(902) 494-2358

FAX (902) 494-6889

DATE: 04/25/2008

AUTHOR: Tara Muth

TITLE: Geological Mapping in Northwest
Bhutan using ASTER Remote
Sensing Data

Degree: BSc Convocation: May Year: 2008

Permission is herewith granted to Dalhousie University to circulate and to have copied for non-commercial purposes, at its discretion, the above title upon the request of individuals or institutions.

Signature of Author

THE AUTHOR RESERVES OTHER PUBLICATION RIGHTS, AND NEITHER THE THESIS NOR EXTENSIVE EXTRACTS FROM IT MAY BE PRINTED OR OTHERWISE REPRODUCED WITHOUT THE AUTHOR'S WRITTEN PERMISSION.

THE AUTHOR ATTESTS THAT PERMISSION HAS BEEN OBTAINED FOR THE USE OF ANY COPYRIGHTED MATERIAL APPEARING IN THIS THESIS (OTHER THAN BRIEF EXCERPTS REQUIRING ONLY PROPER ACKNOWLEDGEMENT IN SCHOLARLY WRITING) AND THAT ALL SUCH USE IS CLEARLY ACKNOWLEDGED.

ABSTRACT

A klippe of low-grade metasediments is exposed in northwest Bhutan, the base of which forms the erosional remnant of South Tibetan Detachment (STD) system. This detachment is an orogen-wide normal-sense shear zone that forms the upper boundary of the Greater Himalayan Sequence (GHS), the exposed metamorphic core of the Himalayas. Field mapping in this region of Bhutan is hindered by many factors such as access, high terrain, climate and logistics, and expense. Thus, many geological boundaries are insufficiently mapped and constrained. Due to high elevation, lack of vegetation and good exposure, this area is well-suited for mapping using remote sensing data. Here we examine the use of ASTER (Advanced Spaceborne Thermal Emission and Reflection Radiometer) remote sensing data for geological mapping of a critical area of the Bhutan Himalaya. Several techniques of ASTER data analysis were tested. The one found to be most suitable for mapping in the region was a combination of band ratio images. The main lithologies mapped using ASTER are: gneiss, leucogranite, metapelite, metacarbonate and shale. The first two belong to the footwall block (i.e. GHS) and the other three units to the hanging wall block of the STD. A structural analysis of the field data from the area is used to help constrain remote sensing mapping, determine the complex synformal geometry of the klippe, and construct geological cross-sections of the study area. Using the procedure developed for NW Bhutan, the northern Sikkim, which has never been visited by geologists, was mapped using ASTER data. This study has improved the geological map of largely inaccessible, yet geologically significant regions of the Himalayas and highlights the effectiveness of using remote sensing data as a geological mapping tool.

Key Words: Himalayas, Bhutan, Sikkim, remote sensing, ASTER, structural analysis, GIS, mapping, STD, Chekha Formation

TABLE OF CONTENTS

ABSTRACT	i
TABLE OF CONTENTS	ii
I. TABLE OF FIGURES	iv
II. TABLE OF TABLES	vi
III. TABLE OF ACRONYMS USED	vii
ACKNOWLEDGEMENTS	ix
<u>CHAPTER 1</u>	1
1.0 Introduction	1
1.0.1 Problem	1
1.0.2 Location	1
1.0.3 Introduction to Methodology	2
1.1 Remote Sensing	4
1.1.1 History of Remote Sensing	4
1.1.2 ASTER Data	5
1.2 Geological Background	9
1.2.1 The Himalayas	9
1.2.2 Geology of the Study Areas	19
1.2.2.1 Bhutan	19
1.2.2.2 The Lingshi Klippe	26
1.2.2.3 Sikkim	26
1.3 Objectives	28
<u>CHAPTER 2</u>	29
2.0 ASTER Data Analysis	29
2.0.1 Basic Principles	29
2.0.2 Value of Multispectral Sensors	30
2.0.3 Attainment of ASTER Data	30
2.1 Methods	31
2.1.1 Image Selection	31
2.1.2 Pre-processing	33

2.1.3 Analytical Techniques	35
2.1.4 Processing Procedure	39
2.2 Results	52
2.2.1 Lingshi Syncline	52
2.2.2 Sikkim	55
<u>CHAPTER 3</u>	60
3.0 GIS Database	60
3.0.1 Introduction to GIS Database	60
3.1 Field Work	60
3.2 Projection of Data	61
3.2.1 Basemap	61
3.2.2 Organisation of Data	64
<u>CHAPTER 4</u>	71
4.0 Structural Analysis of Lingshi Klippe	71
4.1 Categorization of Data	72
4.2 Density Contouring and Statistical Analysis	76
4.3 Results	77
4.4 Summary of Structural Analysis	99
<u>CHAPTER 5</u>	101
5.0 Conclusion	101
5.1 ASTER Analysis	101
5.2 GIS Database	104
5.3 Structural Analysis	104
5.4 Future Work	105
REFERENCES	107
APPENDIX I: CARTOGRAPHIC MODEL	114

I. TABLE OF FIGURES

Figure #	Title	Page #
1.1	Location map	2
1.2	Mount Chomolhari	4
1.3	ASTER instrument in space	6
1.4	Simplified geological map of the Himalayas	11
1.5	Generalized cross-section depicting channel flow hypothesis	15
1.6	Detailed map of the geology of the Himalayas (Nepal and Bhutan)	18
1.7	Geological map of Bhutan (Gansser, 1983)	20
1.8	Legend for the geological map of Bhutan	21
1.9	Simplified geological map of Bhutan	24
1.10	Cross-section of Bhutan	25
1.11	Geological map of the Lingshi Klippe	27
2.1	False colour composite image of the Lingshi Klippe	32
2.2	Histogram analysis for NW Bhutan	35
2.3	Cluster analysis for NW Bhutan	37
2.4	Chlorite (1) composite image for NW Bhutan	45
2.5	Chlorite (2) composite image for NW Bhutan	46
2.6	Muscovite composite image for NW Bhutan	47
2.7	Carbonates (1) composite image for NW Bhutan	48
2.8	Carbonates (2) composite image for NW Bhutan	49
2.9	Feldspar composite image for NW Bhutan	50
2.10	Example of NDVI analysis for NW Bhutan	51
2.11	Geological map of the refined lithological units	53
2.12	Gansser's original map for the Lingshi Klippe	54
2.13	False color composite for Sikkim	56
2.14	Carbonates (1) composite for Sikkim	57
2.15	Chlorite (1) composite for Sikkim	58
2.16	Feldspar composite for Sikkim	59
3.1	Unprojected version of the geological map of Bhutan (Gansser, 1983)	62
3.2	Geo-referenced version of the geological map of Bhutan (Gansser, 1983)	63
3.3	Map of station locations	65
3.4	Map of sample locations	66
3.5	Map of planar measurements	67
3.6	Map of linear measurements	68
3.7	Map of the traverses performed in the Lingshi Klippe	70
4.1	Map of the structural data used for analyses	73
4.2	Map of structurally homogeneous zones	75
4.3	Map of the statistical fold axes and trends of lineations	79
4.4	Legend for the stereonet	82
4.5	Group 2 / Area 1: Main Foliation	82
4.6	Group 2 / Area 1: Axial Planes	83
4.7	Group 2 / Area 1: Lineations	83

Figure #	Title	Page #
4.8	Group 2 / Area 2: Main Foliation	84
4.9	Group 2 / Area 2: Axial Planes	84
4.10	Group 2 / Area 2: Lineations	85
4.11	Group 2 / Area 3: Main Foliation	85
4.12	Group 2 / Area 3: Lineations	86
4.13	Group 2 / Area 4A: Main Foliation	86
4.14	Group 2 / Area 4A: Lineations	87
4.15	Group 2 / Area 4B: Main Foliation	87
4.16	Group 2 / Area 4B: Axial Planes	88
4.17	Group 2 / Area 4B: Lineations	88
4.18	Group 2 / Area 4C: Main Foliation	89
4.19	Group 2 / Area 4C: Lineations	89
4.20	Group 1: Sedimentary Bedding	90
4.21	Group 1 / Area 1: Axial Planes	90
4.22	Group 1 / Area 1: Crenulation Cleavage	91
4.23	Group 1 / Area 1: Lineations	91
4.24	Group 1 / Area 2: Main Foliation	92
4.25	Group 1 / Area 2: Axial Planes	92
4.26	Group 1 / Area 2: Crenulation Cleavage	93
4.27	Group 1 / Area 2: Lineations	93
4.28	Group 3: Main Foliation	94
4.29	Group 3: Sedimentary Bedding	94
4.30	Group 3: Lineations	95
4.31	Group 4: Main Foliation	95
4.32	Group 4: Axial Planes	96
4.33	Group 4: Lineations	96
4.34	Group 2 / Area 4B: 2 nd Foliation	97
4.35	Group 2 / Area 4B & C: Conjugate Shear Bands	97
4.36	Structural map of the Lingshi Klippe	98

II. TABLE OF TABLES

Table #	Title	Page #
I	Table of figures	iv
II	Table of tables	vi
III	Table of acronyms used	vii
1.1	ASTER Data specifications compared to Landsat TM and SPOT	8
2.1	List of ASTER images acquired + statistics	33
2.2	Band Ratio Codes for primary mineralogy of the study areas	41-42
2.3	Band-ratio composite images	43
3.1	Sample analyses	64
4.1	Types of structural measurements taken from the field	74
4.2	Division of lithological units into structurally homogeneous areas	76
4.3	Statistical fold axes trends found for main foliation and bedding analyses	78
IV	Table of software programs used	112

III. TABLE OF ACRONYMS USED

Acronym	Meaning
Ar/Ar	<i>Argon/Argon dating</i>
ASTER	<i>Advanced Spaceborne Thermal Emission and Reflection Radiometer</i>
DN	<i>Digital Number</i>
ERSDAC	<i>Earth Remote Sensing Data Analysis Centre</i>
GCS-WGS-1984	<i>Geographic coordinate system with a datum of the World Geodetic System of 1984</i>
GHS	<i>Greater Himalayan Sequence</i>
GIS	<i>Geographic Information System</i>
GPS	<i>Global Positioning System</i>
HST	<i>Himalayan Sole Thrust</i>
KT	<i>Kahktang Thrust</i>
Landsat TM	<i>Landsat Thematic Mapper</i>
Lap	<i>Fold Axis Lineation</i>
Lboudin	<i>Boudinage</i>
Lcr	<i>Crenulation Lineation</i>
LHS	<i>Lesser Himalayan Sequence</i>
Lis	<i>Intersection Lineation</i>
Lkb	<i>Kink Band Lineation</i>
Lmin	<i>Mineral Lineation</i>
LS	<i>Lingshi Syncline</i>
Lsl	<i>Slickenlines or slickenfibres</i>
Lstr	<i>Stretching Lineation</i>
MBT	<i>Main Boundary Thrust</i>
MCT	<i>Main Central Thrust</i>
MFT	<i>Main Frontal Thrust</i>
MHT	<i>Main Himalayan Thrust</i>
NASA	<i>National Aeronautics and Space Administration</i>
NDVI	<i>Normalized Difference Vegetation Index</i>
PCA	<i>Principle component analysis</i>
S0	<i>1st Foliation (without any apparent genetic associations)</i>
Sap	<i>Axial Planes</i>
Scr	<i>Crenulation Cleavage</i>
Sf	<i>Main Foliation</i>
Sf1 / Sf2 etc...	<i>Tectonic Foliation</i>
Sj / Sj1 / Sj2	<i>Fracture set or Joints</i>
Skb	<i>Kink Bands</i>
Sm/Nd	<i>Samarium/ Neodymium Provenance analysis</i>
Sp	<i>Shear Planes</i>
Ss	<i>Sedimentary Bedding</i>

Acronym	Meaning
Ssb	<i>Shear Bands</i>
STD	<i>South Tibetan Detachment System</i>
SWIR	<i>Short-Wave Infrared</i>
TIR	<i>Thermal Infrared</i>
TSS	<i>Tethyan Sedimentary Sequence</i>
U-Pb	<i>Uranium-Lead dating</i>
VNIR	<i>Visible and near infrared</i>

ACKNOWLEDGEMENTS

I would like to extend my deepest gratitude to my supervisors Djordje Grujic, Charles Walls, and Dawn Kellett for their extensive help, knowledge and guidance throughout this thesis. I would also like to thank all of the many geologists over the years whose field mapping in the Himalayas made this work possible. Finally, thank you to my family and friends who were unfailing in their support, patience and encouragement when I most needed it.

Thank you.

-Tara Muth

CHAPTER 1

1.0 INTRODUCTION

1.0.1 Problem

In this study, ASTER (Advanced Spaceborne Thermal Emission and Reflection Radiometer) remote sensing data are used to identify map-scale tectono-stratigraphic units and create a geological and structural map of Northwest Bhutan and Northern Sikkim. Field mapping in the Himalayas is hindered by factors such as access, terrain, expense, and climate. Lower-lying levels of the mountain range are densely vegetated or cultivated and the rocks are heavily weathered, meaning the best exposures lie at higher altitudes, which are largely inaccessible due to the extreme relief, as well as political border sensitivities. Snow in the winter and monsoon rains in the summer restricts geological expeditions to the months of May, September and October. The field work in the area is also expensive as the costs are up to US \$220 per day, per person in Bhutan. Thus, many areas of the Himalayas are poorly mapped and geological boundaries are unconstrained.

1.0.2 Location

The Kingdom of Bhutan is located in the Eastern Himalayas, bordering India to the east, south and west and Tibet to the north (Figure 1.1). It is situated entirely within the Himalayan range, from 26.5° N to 28° N and from 88° E to 92° E, bounded by the Tibetan Plateau to the north and the Precambrian Indian plate to the south (Gansser, 1983). Sikkim is located to the northwest of Bhutan and east of Nepal. It is a tiny state of India, located approximately from 27.1° N to 28.1° N and from 88.0° E to 88.9°E.

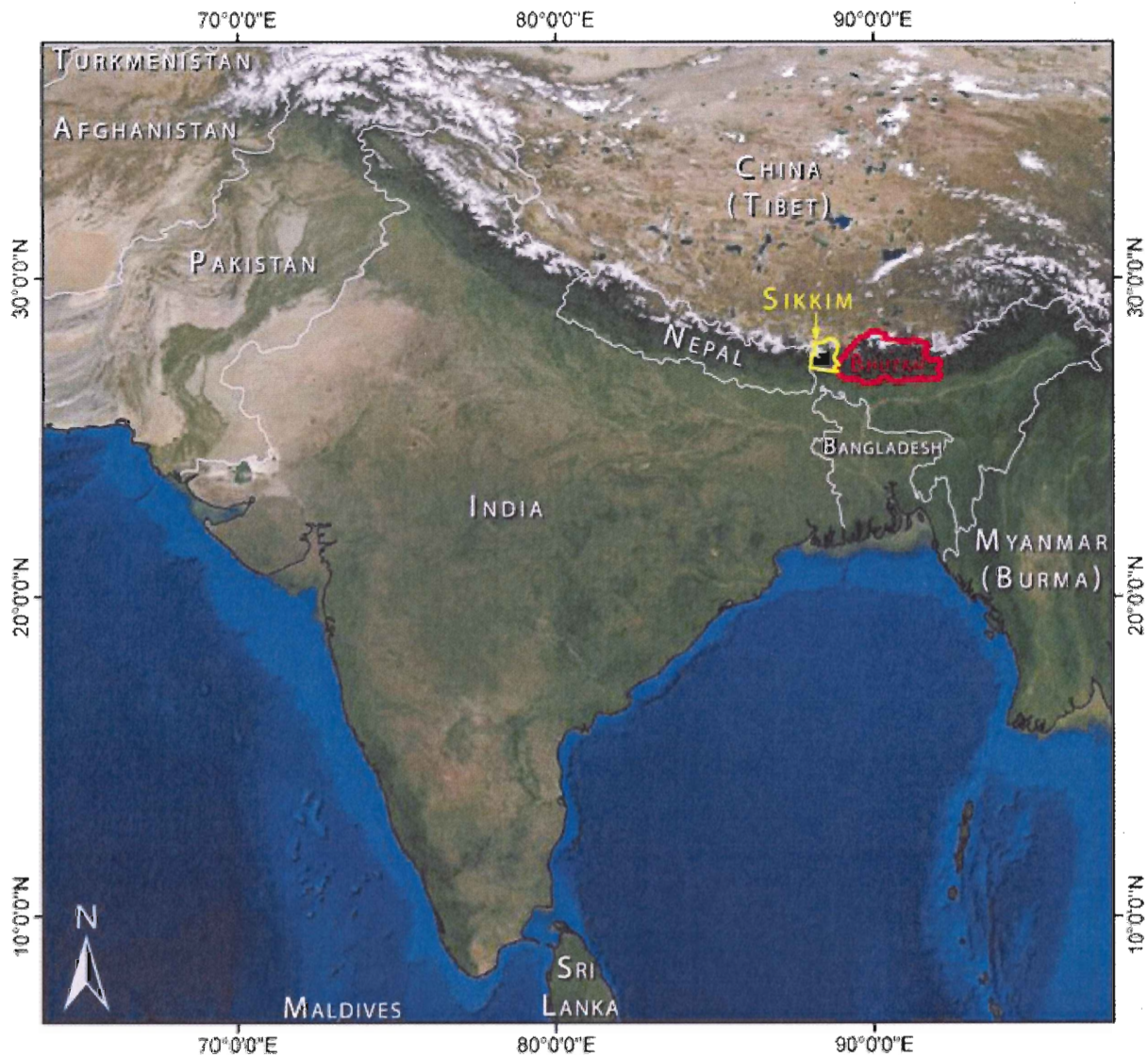


Figure 1.1: Map showing the location of Bhutan (in red) and Sikkim (in yellow). Projected in the Geographic Coordinate System with the World Geodetic system datum of 1984 (GCS-WGS-1984). (Exported from ArcMAP using ESRI data files + GeoMapApp)

1.0.3 Introduction to Methodology

The main aim of this study is to locate a first-order shear zone in the eastern Himalayas. South Tibetan Detachment system (STD), an orogen-wide normal fault-geometry shear zone

separating the upper crust of the Himalayas from the high-grade metamorphic rocks of the middle crust, is exposed in Northwest Bhutan. Due to logistic limitations, its precise location and relationship to the surrounding rocks is poorly constrained. The current geological map (Gansser, 1983), is based only upon field work in accessible areas and Landsat I (1977) data. The introduction of new remote sensing technologies enables us to look at the region from a new perspective and refine the old lithological boundaries. ASTER satellite images can be used to map the bedrock geology, due to the variations in reflectance of different types of bedrock, allowing us to more precisely define the lithological and structural boundaries. The area being mapped is at relatively high elevations with mountainous terrain; ranging from ca. 2300 m at the lowest up to over 7300 m at the highest peaks (Figure 1.2) near the border with Tibet. The relative lack of vegetation and excellent exposure make it an ideal location for mapping with remote sensing. In addition, the combination of remote sensing data with field mapping has not yet been extensively applied in this area. The information gathered from the images is correlated with the field data that has already been collected from Bhutan, allowing the same technique to be applied to an area of similar geology in neighbouring Sikkim. The area in Bhutan has been visited on several occasions by western geologists (including Dalhousie professors); however, no known mapping has been performed in northern Sikkim. However, this second field area lies approximately 40 km south of an area studied using a similar technique by Watts et al. (2005). This study will allow us to gain a new perspective of the geology of the area and construct a well-constrained geological map, as well as experiment with an innovative, modern mapping technique.



Figure 1.2: Mount Chomolhari, 7314 m, is the tallest mountain in the study area. The mountain is a horst with the Yadong-Gulu Graben to the west. To the SE the massif is bordered by major seismically active strike slip fault. (Photo Courtesy of Djordje Grujic)

1.1 REMOTE SENSING

1.1.1 History of Remote Sensing

Remote sensing is the collection of information from a distant or remote location (Campbell, 2007). More specifically, the type of remote sensing used for this study is the analysis of electromagnetic radiation that is reflected or emitted from the surface of the Earth.

The very first “remote sensing” images were photographs taken from balloons in 1858 (Campbell, 2007). Even in its earliest forms, scientists recognized the value of being able to view the Earth from a distance. Remote sensing has now grown into a major field of research, with an intricate network of techniques serving a wide range of disciplines. Today, satellites in space are used to capture not just visible data, but data that span the entire electromagnetic spectrum, making it an invaluable tool for a range of different applications such as, geomorphology, geology, hydrology, soil analysis, atmospheric sciences, urban planning, forestry, international politics, agriculture, environmental monitoring, etc. One of the more recent and exciting functions in geology for remote sensing data is the ability of remote sensing data to distinguish differences in bedrock geology from space. Such a function is extremely helpful for mapping areas that are unsuitable for traditional field mapping, or even as a method to map very large, exposed areas quickly and relatively inexpensively. Even so, the most sophisticated remote-sensing techniques still require ground-truthing, thus the best use for this type of data is in tandem with field work. Satellite imagery can also be very useful for generating an overview of the regional geology and structural variations present in an area, which may not be possible or visible on a smaller, localized scale.

1.1.2 ASTER Data

The ASTER instrument aboard the National Aeronautics and Space Administration’s (NASA) satellite Terra collects remote spectral data that are particularly well-suited for geological mapping applications. ASTER is an advanced multi-spectral instrument, gathering data encompassing 14 different bands from the visible and near infrared (VNIR) to the thermal infrared (TIR). The ASTER obtains several more bands than the Landsat Thematic Mapper (14

vs. 7), thus improving the spectral and radiometric resolution available for geological mapping (Table 1.1). The description following is derived from that provided by Abrams (2000). The ASTER device was launched in December, 1999 aboard the NASA spacecraft Terra, for an ongoing mission to obtain a global coverage map of the Earth's surface (Figure 1.3). ASTER data can be used to study many features, such as vegetation patterns, natural hazards such as volcanic eruptions, climate change, glaciers, sea-ice extent and albedo, degradation of coral reefs, etc .



Figure 1.3: Rendered image depicting the Terra spacecraft (with the ASTER instrument aboard) as it would look in space. (After Herring, <http://terra.nasa.gov/Brochure/brochure.pdf>)

The ASTER instrument gathers data from three spectral categories: from the VNIR (Visible and near-infrared) spectrum ($0.52\text{-}0.86\ \mu\text{m}$) with 15 m resolution, the SWIR (short-wave infrared) spectrum ($1.60\text{-}2.45\ \mu\text{m}$) with 30 m resolution and the TIR (Thermal infrared) spectrum

(8.125–11.65 μm) with 90 m resolution. A backward-looking radiometer within the VNIR band 3 provides along-track stereo capability. Swaths of data are collected approximately 60 km in width, with the additional ability to view any spot on the surface at least once every 16 days.

The ease of access and acquisition, and availability of several customized data options to meet the specific needs of the researcher, makes ASTER data an appealing choice for research purposes in Earth Sciences. The addition of several more bands in the SWIR (short-wave infrared) and TIR range increases spatial resolution, makes the ASTER instrument a logical advancement of the Landsat-TM device and especially useful for lithological mapping based on surface reflectance (Abrams, 2000).

Table 1.1: ASTER technical data specifications compared to Landsat TM and SPOT (preceding analogous remote sensing instruments) data formats.

(After ERSDAC, 2005; Abrams et al., ASTER User's Handbook; and Abrams et al., 1995)

ASTER				Landsat TM		SPOT	
Subsystem	Band #	Spectral Range (μm)	Spatial Resolution (m)	Band	Spectral Range (μm)	Band	Spectral Range (μm)
VNIR			15	1	0.45-0.52		
	1	0.52-0.60		2	0.52-0.60	1	0.50-0.59
	2	0.63-0.69		3	0.63-0.69	2	0.61-0.68
	3N	0.78-0.86		4	0.76-0.90	3	0.79-0.89
	3B	0.78-0.86					
SWIR	4	1.60-1.70	30	5	1.55-1.75		
	5	2.145-2.185					
	6	2.185-2.225					
	7	2.235-2.285		7	2.08-2.35		
	8	2.295-2.365					
	9	2.360-2.430					
TIR	10	8.125-8.475	90				
	11	8.475-8.825					
	12	8.925-9.275		6	10.4-12.5		
	13	10.25-10.95					
	14	10.95-11.65					

ASTER data have already been used with success to map some of the dominant lithologies of the Himalayan orogen in southern Tibet (Watts et al., 2005). A band ratio technique combined with field observations was used to distinguish between Tertiary granites and Cambrian gneisses based upon their muscovite compositions. The study successfully

mapped several gneiss domes that were previously unknown and greatly improved upon the mapping accuracy of the known domes in the region (Watts et al., 2005). The lithologies mapped by Watts et al. are thought to be similar to those of the Bhutan and Sikkim study areas (Figure 1.1), thus a similar technique is used for this study.

ASTER imagery has also been used effectively for several other geological mapping projects. Before the launch of the Terra spacecraft, simulated ASTER data were proven as a valuable tool for mapping lithologies in the Cuprite Area of Esmeralda County, Nevada to distinguish zones of alteration products in Tertiary volcanic rocks (Abrams & Hook, 1995). In another study (Gomez et al., 2005), ASTER data were used to map lithological contacts in a large syncline/anticline pair in Namibia by using only a geological map as support for the analysis. The purpose of the study was to assess the viability of several different methods of processing the data, and the lithological contacts were mapped to a precision and extent that was not possible using field methods (Gomez et al., 2005).

1.2 GEOLOGICAL BACKGROUND

1.2.1 The Himalayas

The Himalaya range is a truly spectacular mountain range, spanning six countries, with peaks that form the highest relief on Earth. The Himalayas cover an area of 2500 km in length and 250-300 km in width, stretching from the Nanga Parbat peak (8125 m) in the west to the Namche Barwa peak (7782 m) in the east, and from the Indus-Tsang Po suture in the north to the Ganges Plains in the south (Figure 1.4; Hodges, 2000; Brunel et al., 2005). The Himalayan orogen was formed by the collision of two continental plates, the Indian plate to the south and the Lhasa Block of the Asian plate to the north. One hundred million years ago, the vast Neo-

Tethys Ocean separated the Indian Plate from the Eurasian plate (Hodges, 2000). The oceanic crust of the Neo-Tethyan Ocean was subducted northwards beneath the Eurasian continent during the Mesozoic. Tibet formed during the process, through the successive accretion of several exotic terranes, squashed onto the Eurasian Plate (Yin & Harrison, 2000; Tapponnier et al., 2001). A continental volcanic arc formed during the Lower Cretaceous off the coast of the Eurasian plate, dominated by volcanic with plutonic rocks, metamorphosed Precambrian-Mesozoic country rock and Cretaceous-Tertiary forearc basin sediments. From the Mid-Cretaceous to the Lower Paleocene, the island arc, plutons and sedimentary sequences assembled together into what is known as the Transhimalayan Zone. After its accretion, the zone continued to evolve as a continental arc complex, with a complex series of calc-alkaline plutons and volcanics, dominated by the immense Gangdese batholith (Hodges, 2000).

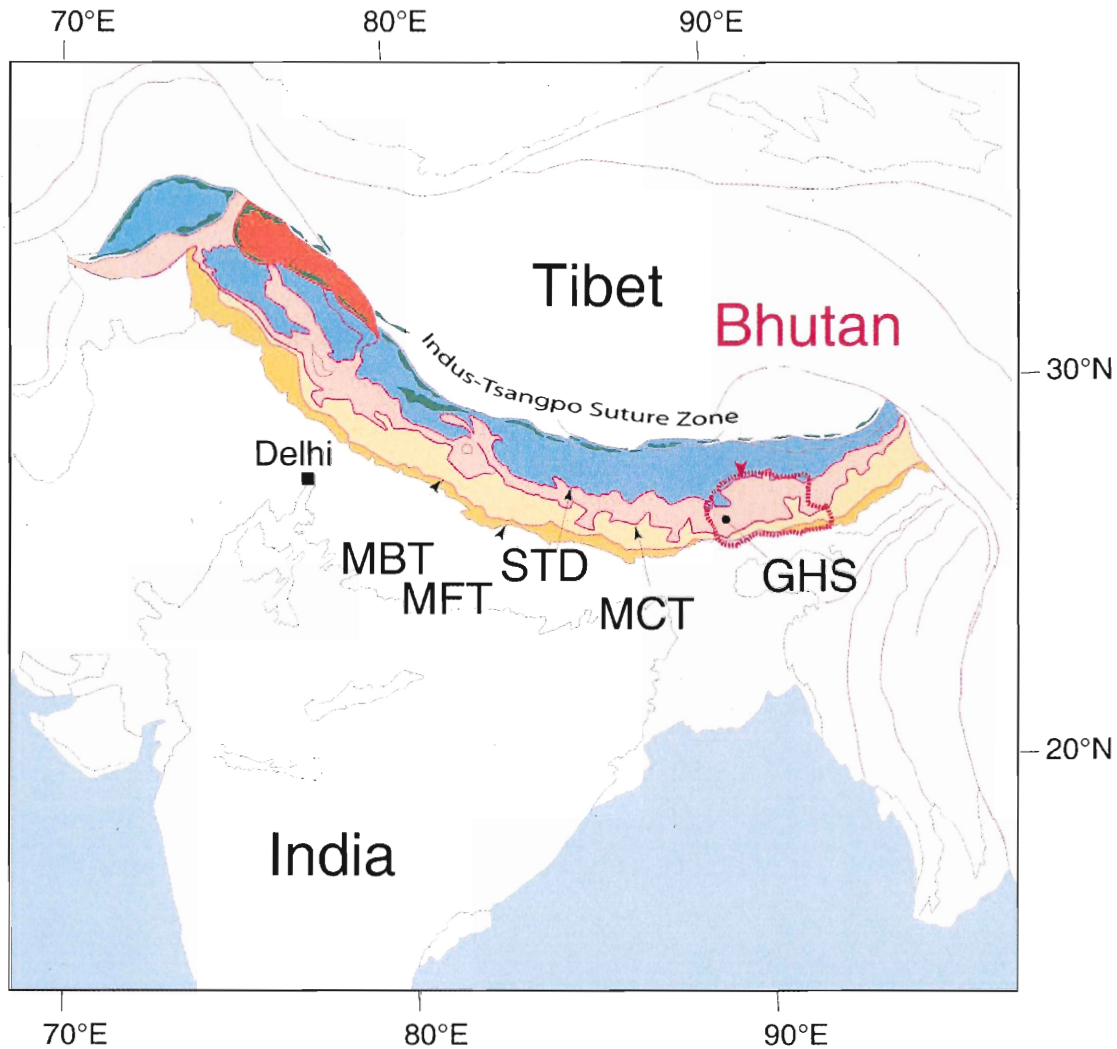


Figure 1.4: Simplified geological map of the Himalayas, showing some of the key geologic and tectonic features in context of the whole orogen. MBT= Main Boundary Thrust, MCT = Main Central Thrust, MFT = Main Frontal Thrust, STD = South Tibetan detachment, GHS (in red) = Greater Himalayan Sequence, Blue = Tethyan Sedimentary Sequence (TSS), Green = Ophiolites of the Indus-Tsang Po Suture zone, Tan = Lesser Himalayan Sequence (LHS), Light Orange = Siwaliks, Dark Orange = Batholiths (Hodges, 2000), Grey = Quaternary cover. (After Gansser, 1983).

The exact timing of the collision between the continental crust of India with Southern Tibet is a widely debated topic and there have been several varying methods to determine the precise age of the impact. Estimates from stratigraphic analysis suggest that the collision date

ranges from 52 to 55 Ma, at the transition from marine to non-marine sediments in the collision zone (Leech et al., 2005). Paleomagnetic data indicate that the collision occurred at ~ 55 Ma when the northward spreading rate of the Indian Ocean slowed dramatically from 180 ± 50 mm/year to 100 ± 20 mm/year (Klootwijk et al., 1992; Guillot et al., 2003). Another method cites the cessation of the continental arc magmatism as evidence for collision occurring before ~ 53 Ma (Hodges, 2000). More recently, researchers dated the peak of ultrahigh pressure metamorphism in exhumed eclogites from the subduction zone. Using the age of metamorphism of the Indian rocks, rates of collision and geometry of the subduction zone, it was possible to retro-deform the Indian plate to the point and time of collision. The results indicated that the edge of the Indian Plate reached the Tibetan trench (i.e. the onset of collision) at no later than $\sim 57 \pm 1$ Ma (Leech et al., 2005). It is suggested that the discrepancies can be resolved by interpreting later events as delayed reactions to the initial collision and commencement of the subduction of the Indian Crust (Leech et al., 2005).

Debate is ongoing as to whether the collision was diachronous or synchronous along the orogen (Aichison et al., 2007; Guillot et al., 2007). The earlier cessation of magmatism in the west than the east and analysis of the sedimentation ages from both sides of the orogen suggest that the collision occurred earlier in the west than the east (Rowley, 1996; Guillot et al. 2007). However, difficulties of constraining the ages of the collision related sediments and correlation have led to an uncertainty about the diachronity, if any that may have existed (Rowley, 1996). Following the collision, convergence and shortening continued, accommodated by thickening of the crust in South-Asia, as ophiolites and flysch of the Tibetan margin piled up, in addition to a southward-propagating fold-and-thrust belt built onto the Indian Plate (Brunel et al., 2005). The large thrust system propagated from north to south, stacking up upper-and mid-crustal rock of

the Indian plate to form the Himalayas, doubling or even tripling the original crustal thickness up to 70-80 km (Brunel et al., 2005; Godin et al., 2006).

The Indus-Tsangpo Suture marks the boundary between the Indian and Asian continents (Figure 1.4). In the immense, near-vertical shear zone, remnants of the Transhimalayan zone, Neo-Tethyan oceanic sequences and southern Indian continental margin rocks are juxtaposed, divided by Mesozoic and Cenozoic faults (Hodges, 2000). To the south of the suture zone is the Tethyan sedimentary sequence (TSS; Figure 1.4 & 1.6), an approximately 10 km-thick sequence of Cambrian to Eocene sedimentary rocks, which were originally deposited on the northern passive margin of the Indian continent (Hodges, 2000; Brunel et al., 2005). Some important features to note within the TSS are the previously mentioned North Himalayan Gneiss Domes. The domes consist of cores of muscovite-biotite Cambrian gneiss, Neoproterozoic-Paleozoic schists and migmatites, along with Tertiary granites and leucogranites, mantled by the rocks from the TSS (Hodges, 2000; Watts et al., 2005).

The Southern Tibetan detachment system (STD) denotes the boundary between the TSS and the Greater Himalayan sequence (GHS) (Figure 1.4 & 1.6). The STD forms a laterally-continuous system group of normal sense ductile shear zone and brittle faults sporadically active between 24 and 12 Ma (Hodges, 2000; Godin et al., 2006). In fact, the STD is a broad ductile shear zone that is postulated to be either the boundary of a channel which is extruding mid-crustal material as the GHS (Beaumont et al, 2001; 2004; 2006; Grujic et al., 1996; 2002) or the passive roof fault of a thrust duplex bounding the GHS (Yin, 2006; Godin et al., 2006; Webb et al., 2007). The STD indicates alternating instances of south and northwards shearing events with the deformation extending for a 3-4 km spread through the footwall and lower portions of the hanging wall (Grujic et al., 1996; Godin et al., 2006). Most instances indicate an older

southward shearing event overprinted by the younger top-to-north shearing (Grujic et al., 2002 and references therein).

The GHS is a sequence of high-grade metamorphic rocks of sedimentary and igneous origins, bounded to the north by the STD and to the south by the Main Central Thrust (MCT) (Figure 1.4 & 1.6). At the top of the GHS, leucogranite intrusions can be found, caused by anatexis melting of the surrounding GHS rocks during the Miocene. A distinctive characteristic of the GHS, which has contributed to the controversy surrounding its formation, is the inverted metamorphic gradient across the unit. The GHS has been variously interpreted as the limbs of large recumbent folds (Gansser, 1964), a thrust sheet which has been subjected to various processes to explain the inverted metamorphic gradient, a pre-existing metamorphic sequence which was then folded and faulted, or as hot rocks from the mid-lower crust conveyed to the surface by the MCT (Swapp & Hollister, 1991; Hodges, 1988). More recently, the GHS is proposed to be a 10-15 km orogenic channel of low viscosity material originating 200 km away from beneath the Tibetan plateau, which was extruded onto the foreland between the MCT and STD (Grujic et al., 1996; 2002; Beaumont et al., 2001; 2004; 2006; Jamieson et al., 2004; 2006; Godin et al., 2006). Thus, the GHS can actually be interpreted as a ductile, partially-melted section of the lower-middle crust, which is being extruded southwards from beneath the Tibetan Plateau (Figure 1.5). Some geologists however, strongly oppose this hypothesis (e.g. Harrison, 2006; Kohn, 2008).

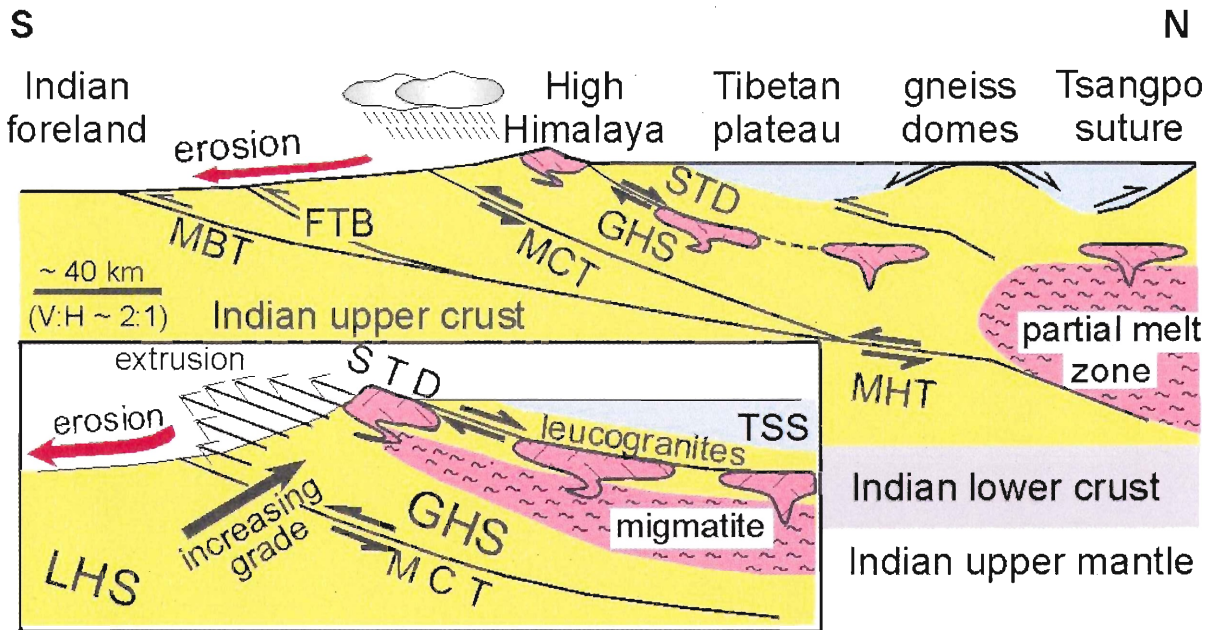


Figure 1.5: Generalized cross-section of the Himalayas showing the main features. Inset: Diagram depicting the extrusion of the GHS as an orogenic channel flow. Blue = weak, upper crust; Yellow = medium-strength middle crust; Grey = strong lower crust; Pink = melt-weakened middle crust (including migmatite and plutons). MBT = Main Boundary Thrust, FTB = Fold & Thrust belt (Siwaliks), MCT = Main Central Thrust, GHS = Greater Himalayan Sequence, STD = South Tibetan Detachment, MHT = Main Himalayan Thrust, TSS = Tethyan Sedimentary Sequence. (After Beaumont et al., 2001)

The base of the GHS is marked by the MCT, an intracontinental thrust shear zone, which can be traced for 2500 km along the mountain belt and up to 10 km thick (Daniel et al., 2003). Like the GHS, the most distinguishable trait about the MCT is the inverted metamorphic gradient across the zone, peak metamorphic temperatures increase upwards through the zone and there may be an rise in pressures as well (Daniel et al., 2003). The phenomenon is related to the contentious formation of the GHS. The shearing is directed southwards, and the thrust merges with the Main Boundary thrust (MBT) and Main Frontal Thrust (MFT) at depth to form a large north-dipping décollement, which is often referred to as the Main Himalayan Thrust (MHT) (Nelson et al., 1996), or alternatively as the Himalayan Sole Thrust (HST) (Hodges, 2000). The

MCT was active from about 25 to 14 Ma, roughly coeval with the STD for a long period, from ~24 to ~12 Ma (Godin et al., 2006). Ages as young as 11-10 Ma have been reported as well (Catlos et al., 2004).

Bounded above by the MCT and below by the MBT, lies the Lesser Himalayan sequence (LHS; Figure 1.4 & 1.6). The LHS is composed primarily of lower-grade meta-sedimentary rocks deformed into a series of fold-and-thrust sheets (Hodges, 2000). Quartzites, phyllites and schists dominate, with minor marbles, metamorphosed mafics, and augen orthogneisses. The sequence is likely a continuation of the TSS, deposited on the Indian Passive margin, but earlier and more proximal than the sediments of the TSS and with different source rock provenance. The deposition age has been interpreted as mid-Proterozoic, Neoproterozoic and Paleozoic-Cenozoic for various litho-tectonic packages (DeCelles et al., 2000). Similar to the GHS, the LHS rocks also display an inverted metamorphic gradient, increasing from lower greenschist to lower amphibolite facies upwards at the MCT (Swapp & Hollister, 1991; Hodges, 2000; Daniel et al., 2003).

The MBT displaces the Lesser Himalaya southwards on top of the Sub-Himalayan Zone, or the Siwaliks, a Neogene-Quaternary foreland basin, composed of molasse sediments from erosion of the Himalayas (Najman, 2006). The MFT, the actual “active” thrust front of the orogen, thrusts the Siwaliks out onto the Quaternary sediments of the Indo-Gangetic Basin (Figure 1.6) (Brunel, 2005; Hodges, 2000). The Himalayas still form one of the most active orogenies today, with surface uplift and active tectonics still occurring. River terraces in the Sub-Himalaya region reveal recent tectonic activities in the region (Gansser, 1964; Wesnousky et al., 1999). The Indian plate continues to move northwards at a rate of 36-40 mm/year, of

which 15-20 mm/year is partitioned into the Himalayas (Zhang et al., 2004) resulting in earthquakes and continued uplift in the region (Bilham et al., 1997; Meyer et al., 2006).

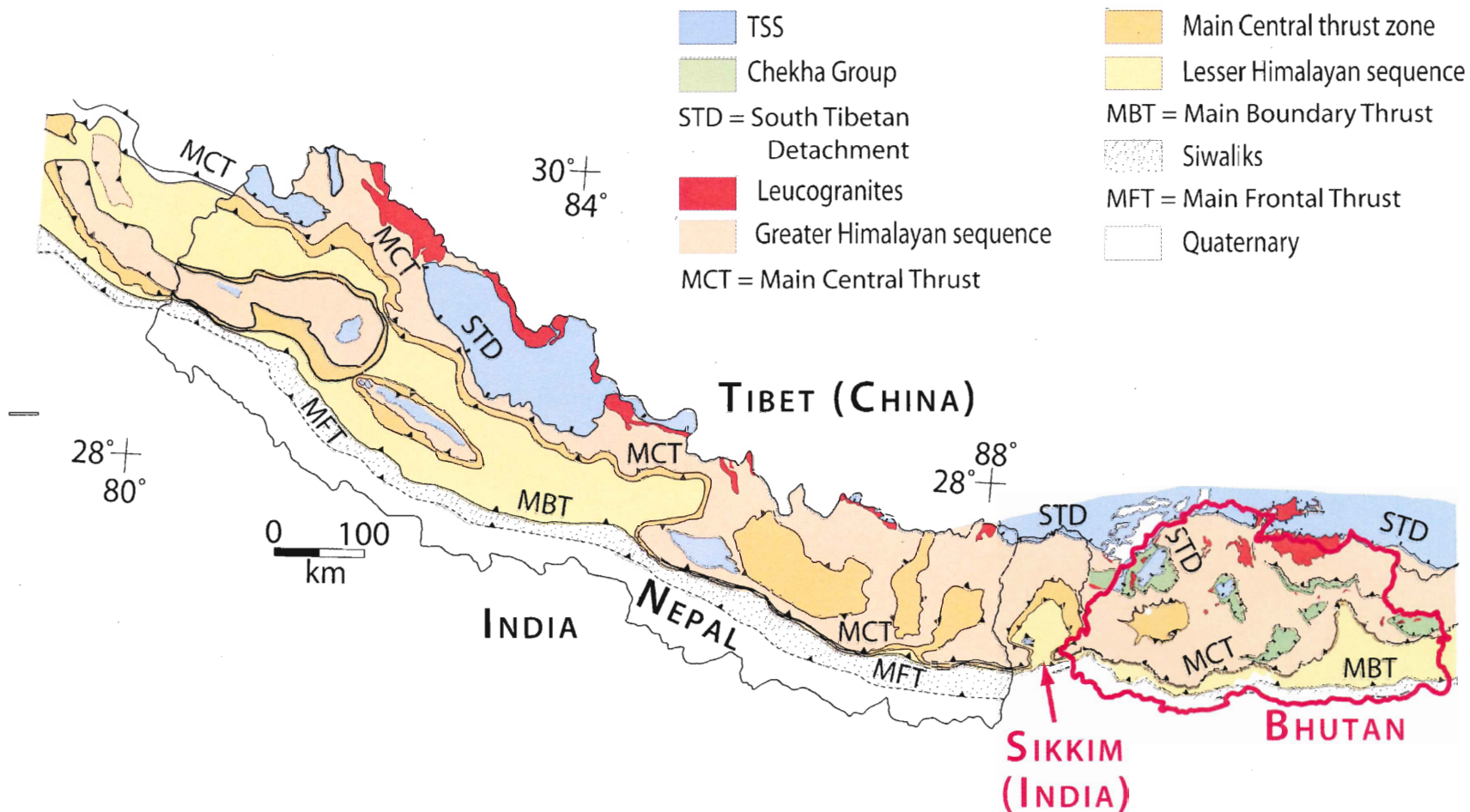
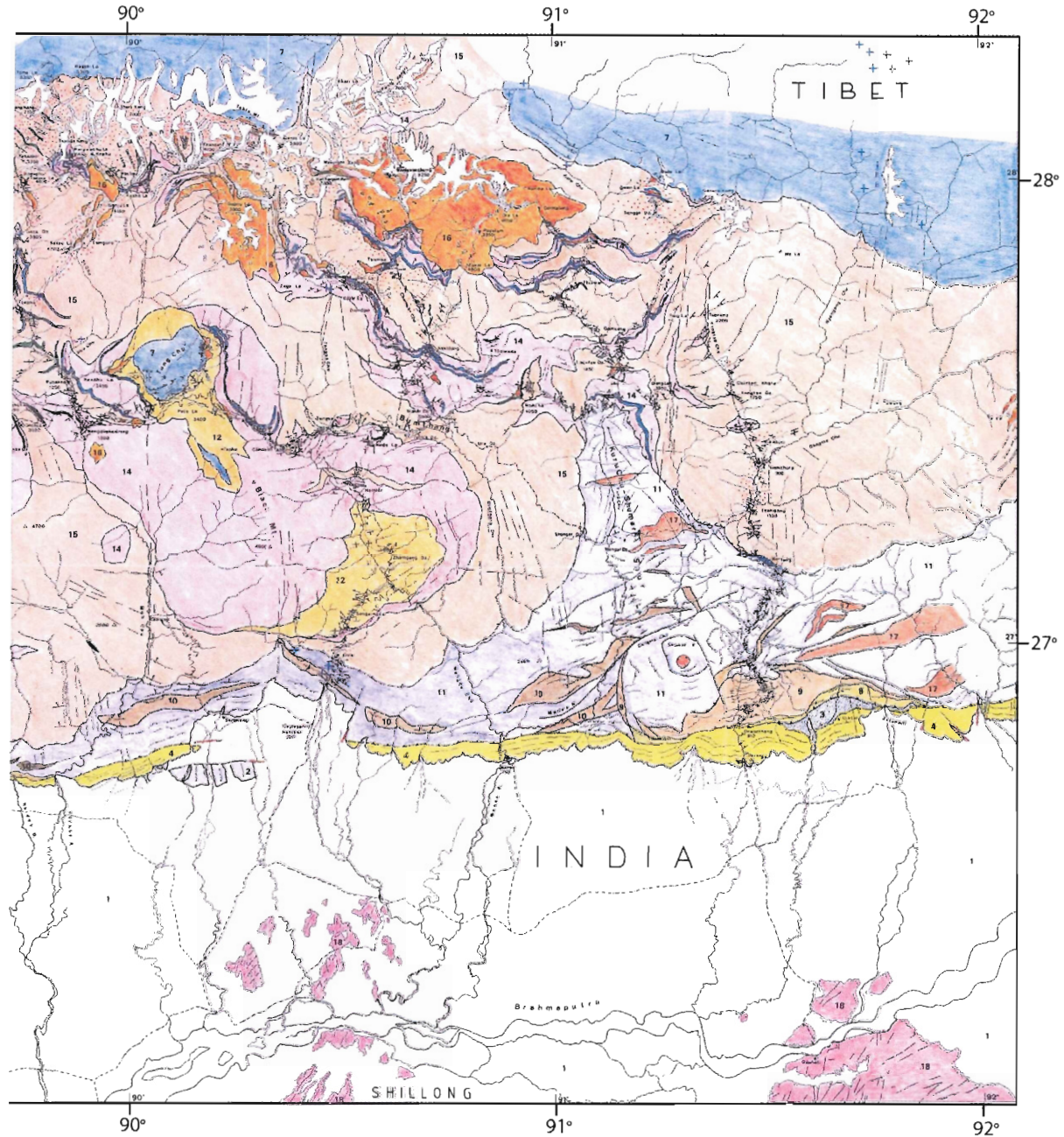


Figure 1.6: A more detailed map of central and eastern Himalayan geology showing the key features mentioned. (After McQuarrie et al., in prep)

1.2.2 Geology of the Study Areas

1.2.2.1 Bhutan

The first geological map of the Bhutan Himalaya was produced by Augusto Gansser, based on field work from 1963 to 1969, which was further revised in 1977 using Landsat photos and other available information (Figure 1.7 & 1.8; Gansser, 1983). Some mapping has also been performed by the Geological Survey of India (Bhargava, 1995). More recent additions to the understanding of the region have been made by analyses of metamorphic and structural trends by Swapp & Hollister (1991); Grujic et al (1996, 2002); Davidson et al. (1997); Edwards et al. (1996, 1999); Daniel et al. (2003); Ritchie (2004); Richards et al. (2006); Hollister & Grujic (2006); Carosi et al. (2006); and Chakungal (2006). The studies recognize the similarity of Bhutan to the Central Himalayas, however there are several notable exceptions. An extra thrust fault is present within the GHS between the MCT and the STD known as the Kahktang Thrust. Additionally, low-grade Tethyan sedimentary rocks occur as klippen atop the GHS (Grujic et al, 2002). In addition, the studies make a major contribution to the understanding of the formation of the GHS by interpreting it as a putative channel which has been exhumed from the mid-crustal levels underneath the Tibetan Plateau (Grujic et al 1996; 2002).



some additions in 1977, from Landsat photos and other available information. Scale = 1:500,000. Legend follows (Figure 1.8). (After Gansser, 1983)

LEGEND

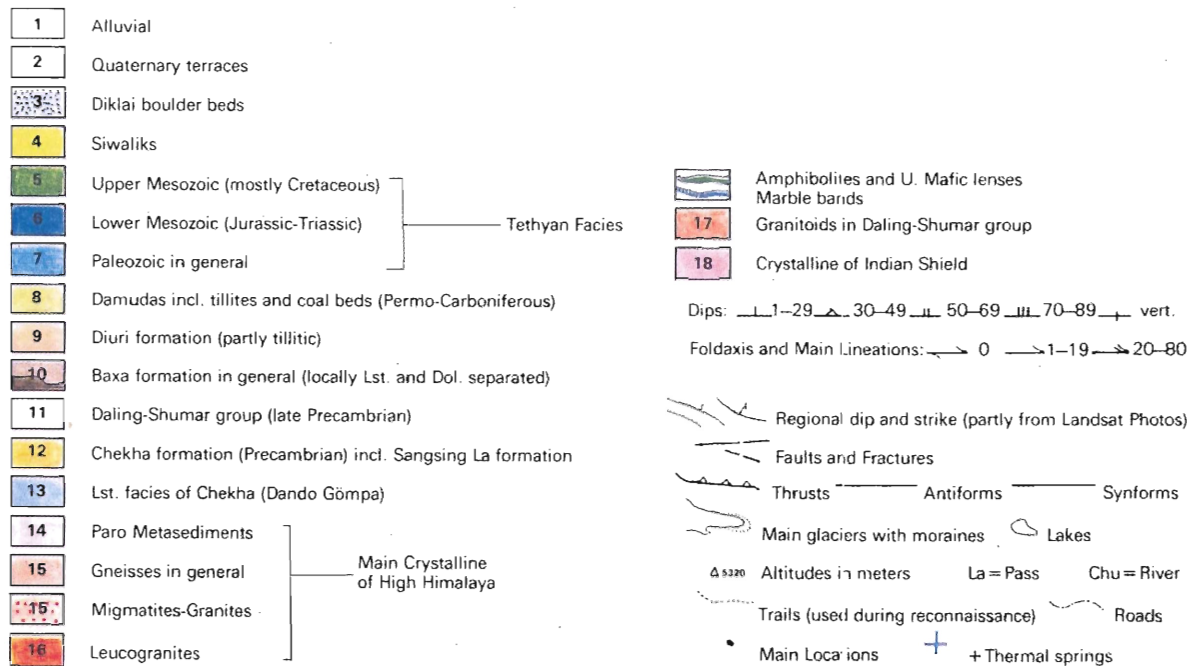


Figure 1.8: Legend for the Geological Map of Bhutan. (After Gansser, 1983)

In Bhutan, the Sub-Himalayan zone is dominated by the Siwaliks and younger deposits, composed of molasse sediments up to 3000 m in thickness (Bhargava, 1995). The Siwalik deposits can be traced intermittently across Bhutan, with erosional or depositional gaps in several locations. The MFT is intermittent, but present along the front of the Siwaliks, and the MBT can be traced easily along the top. Above the MBT lie the Lower Himalaya. Due to its lower elevation and thus higher mean annual precipitation (Bookhagen et al., 2005; Grujic et al., 2006), the LHS is strongly weathered and usually heavily vegetated, and therefore exposure is frequently poor. The MCT is not as fully exposed in Bhutan as in other areas of the Himalayas, however where it is visible the boundary is quite sharp and pronounced (Gansser, 1964; 1983; Daniel et al., 2003). Deformation within the MCT shear zone begins about 2 km below the

MCT, extending to the top of the GHS and retaining the same inverted metamorphic gradient as observed elsewhere in the Himalayas.

In Bhutan, the GHS can be divided into three main units: a granitic orthogneiss unit; the Paro Metasediments, composed of meta-carbonates, with interspersed schists, quartzites and amphibolite to granulite facies migmatite (derived from the other two units); and lastly, leucogranite intrusions (Gansser, 1983). These three main units are repeated several times along the section; either because of large-scale isoclinal folding and/or thrusting (e.g. Kahktang thrust). The leucogranite plutons, located at the top of the GHS exhibit intruding the STD shear zone exhibit evidence of northward shearing (Grujic, 2002). Crystallization ages range from between 26 and 11 Ma (Edwards & Harrison, 1997; Wu et al., 1998; Grujic et al., 2002; Daniel et al., 2003; Parrish et al., 2004; Carosi et al., 2006; Chakungal, 2006; Kellett et al., 2008). The intrusions occur as dykes and sills of leucogranites and leucotonalites, increasing in abundance upwards in the section, with the largest ones occurring just below the STD and above the Kahktang Thrust (KT) (Daniel et al, 2003).

The Kahktang thrust is an important structure which may be unique to Bhutan. The fault occurs as an out-of-sequence, younger thrust within the GHS, serving to nearly double its thickness (Figures 1.9 & 1.10) (Gansser, 1983; Grujic et al., 2002; Daniel et al, 2003). The thrust cuts the STD, as well as the leucogranite dykes, therefore it is interpreted to be younger than both structures. According to seismic surveys (Hauck et al., 1998), the thrust appears to merge with the STD at about ~ 25 km depth, rather than with the basal décollement as is conventionally the rule for out-of-sequence thrusts (Grujic et al., 2002). Since the STD was folded prior to the formation of the thrust, it could not easily be reactivated, thus the Kahktang thrust is likely a new fault formed as a consequence of continued shortening (Grujic et al, 2002).

The STD is a shear zone separating the GHS from the TSS with northward directed shearing, meaning that it is a normal-sense detachment. In Bhutan, the STD displays a complex deformational history, with top-to-south fabrics being overprinted by top-to-north fabrics. Throughout Bhutan, isolated remnants of low-grade metasedimentary rocks (most likely Neoproterozoic to early Paleozoic (Bhargava, 1995)), known as the Chekha formation, lie structurally on top of the GHS (Figures 1.8 & 1.9). The outcrops form the cores of large, open, upright synforms. The sole of the Chekha formation indicates the ductile top-to-north shearing and deformed leucogranite dykes generally associated with the STD. The formation is interpreted to have been formerly connected to the STD further north, but has been removed elsewhere in the Himalayas (Grujic et al, 2002). Thus, it is suggested that the sheared base of the Chekha formation may be a segment of the STD (Grujic et al, 2002). Thus, the Chekha klippen may represent the southern-most extent of the STD in the Himalayas (Grujic et al., 2002).

The Chekha formation is composed of phyllite, mica schists, hornblende schists, quartzites, limestones and quartz conglomerates (Bhargava, 1995; Gansser, 1983). Contrary to the GHS, the degree of metamorphism decreases upwards in the formation (Figure 1.9 & 1.10; Grujic et al. 2002; Ritchie, 2004; Kellett, PhD in progress).

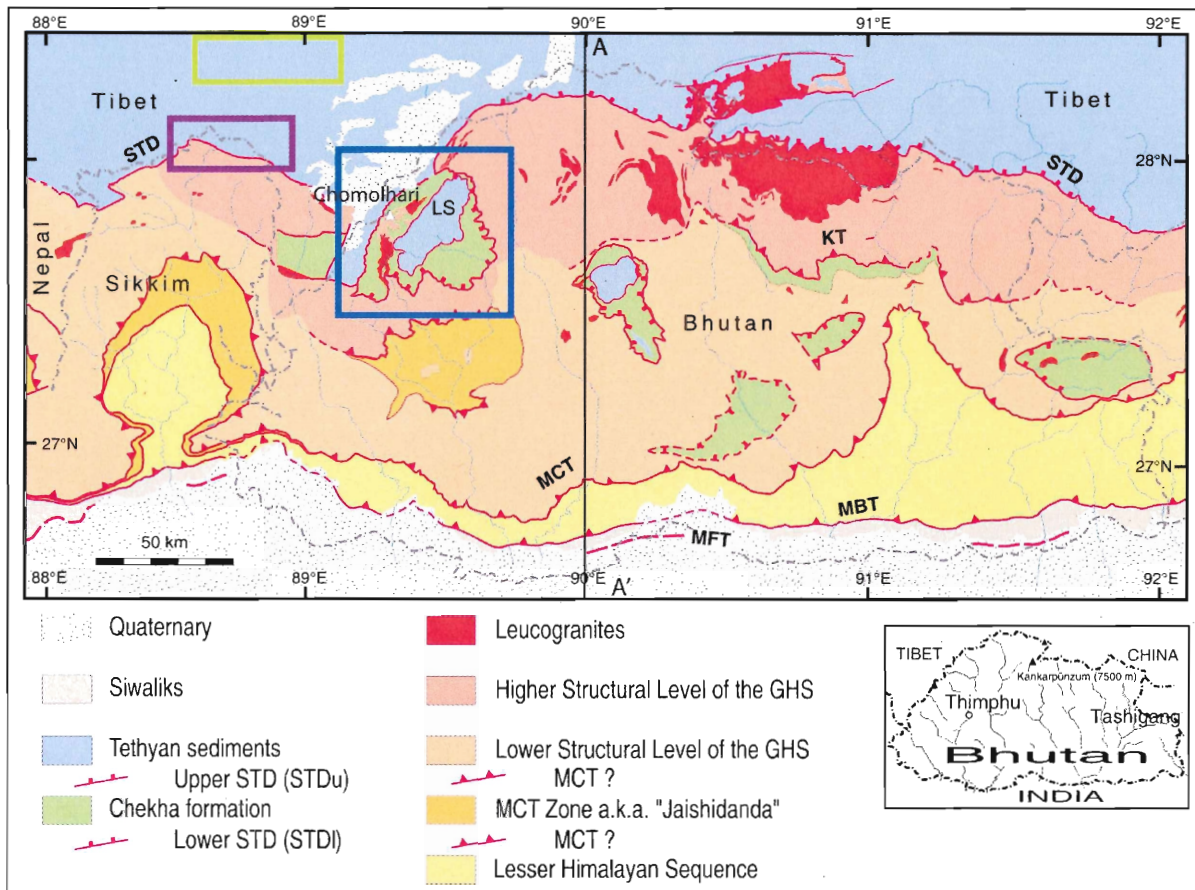


Figure 1.9: Simplified geological map of Bhutan indicating the study area in blue. Area in purple is the second study area in Sikkim. The area in green shows the approximate position of one of the North Himalayan Gneiss domes as mapped by Watts et al. (2005). STD = South Tibetan Detachment System, MCT = Main Central Thrust, MFT = Main Frontal Thrust, MBT = Main Boundary Thrust, KT = Kahktang Thrust, LS = Lingshi Syncline, A-A' = Location of cross section (Figure 1.10). (After Gansser, 1983; Grujic et al., 1996; 2002; and personal observations by D. Grujic)

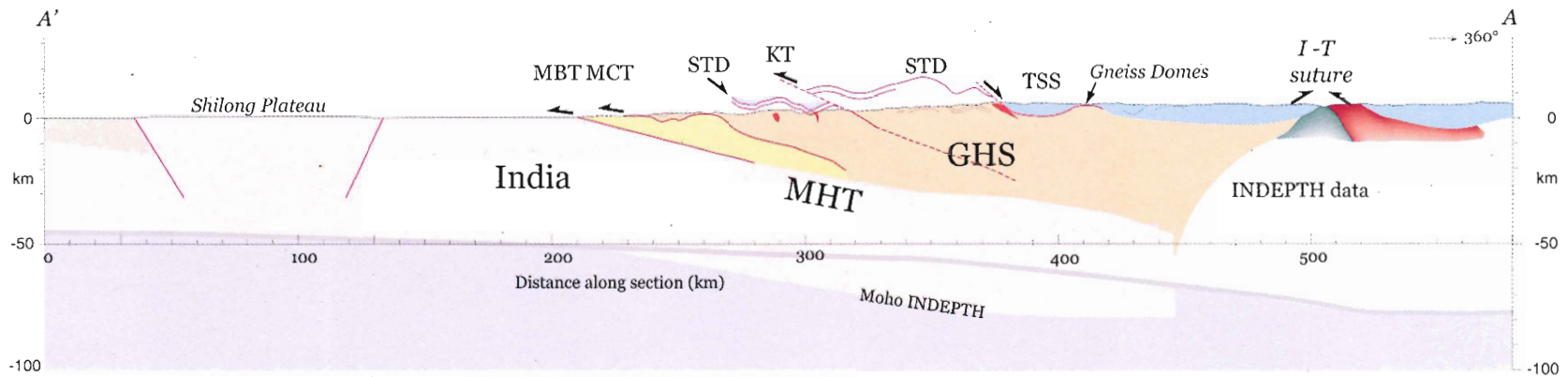


Figure 1.10: Cross-section of Bhutan at A-A' (Figure 1.9), indicating the structural relationships of the major units. The cross-section is extrapolated beyond the boundaries of the above map, in order to show the regional relationships to some of the other structures previously mentioned. MHT = Main Himalayan Thrust; I-T Suture = Indus-Tsang Po Suture line. (After Gansser, 1983; Grujic et al., 1996; 2002; and personal observations by D.Grujic)

1.2.2.2 The Lingshi Klippe

The primary location of this study is Northwestern Bhutan (Figure 1.9), at one of the meta-sedimentary klippen of Bhutan known as the Lingshi Klippe/Syncline (Figure 1.11). In this area, the Chekha formation is positioned beneath Paleozoic to Mesozoic Tethyan sediments, and above the gneisses and migmatites of the GHS. The upper and lower contact are both considered to be ductile normal-fault geometry shear zones (Grujic et al., 2002; Hollister & Grujic, 2006), as has also been suggested for the area of Mt. Everest in central Nepal (Searle et al., 2003). However, the Everest area is very difficult to access for detailed field study, therefore the timing and relationship of these two shear zones remains unknown. Since there exists a well-exposed fragment of the STD at the Lingshi klippe, a unique opportunity is presented to study these intriguing contacts. However, the area has only been mapped along two major valleys, the only areas of access to the region. The limited access has made it difficult to properly constrain the STD. Landsat data has also already been used to an extent for some mapping of the area, but increased resolution and accuracy can be achieved with the use of ASTER data, enabling us to make a more complete map of the region. In addition, the end results of the project will provide a fundamental contribution to the currently ongoing concomitant PhD project conducted by Dawn Kellett at Dalhousie University.

1.2.2.3 Sikkim

The ASTER technique for mapping was established and tested against the area in Bhutan, using the ground-truthing available. The same procedure could be applied to map similar lithologies throughout the region. To test this concept, a second area of study was chosen, located in Northern Sikkim (Figure 1.9). The area is also very inaccessible, and has never been mapped. The lithologies are similar to those studied in Northwest Bhutan and by Watts et al.

(2005). Thus, we applied the same technique used in Bhutan to map the geology of the Sikkim area as well. Future field excursions by D.Kellett and D. Grujic expect to visit the region, and the lithological map will provide the base to select the most relevant outcrops to visit to ground truth the geology determined using ASTER.

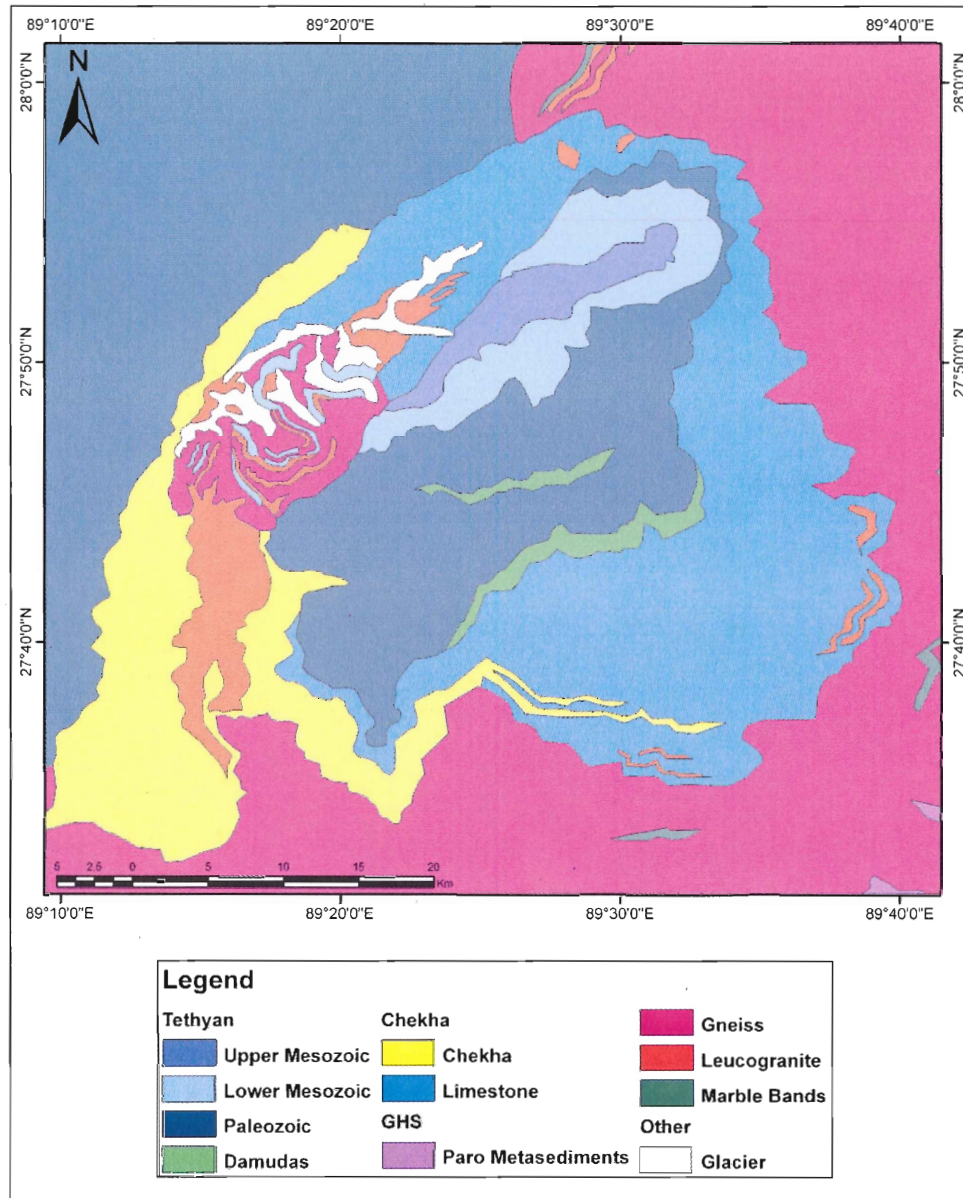


Figure 1.11: Formerly the most current geological map of the Lingshi Klippe (Study area # 1), which must be revised and updated. Traced from Gansser 1983.

1.3 OBJECTIVES

Objectives that we hope to accomplish during the course of this project include:

- 1) Determine the best technique to extract and identify lithological differences using ASTER satellite data;
- 2) Identify different rock types in NW Bhutan using satellite imagery;
- 3) Use the existing field database to match known tectono-stratigraphic units with information from the satellite images;
- 4) Use the collected information in conjunction with structural data analyses to map the boundaries between units on the ground and the major structures such as shear zones and axial traces of major folds.
- 5) Apply the techniques developed to a previously unexplored area in Northern Sikkim

CHAPTER 2

2.0 ASTER DATA ANALYSIS

2.0.1 Basic Principles

The sunlight that we take for granted every day on Earth actually forms a part of a complex phenomenon. Only a small portion of the light constitutes wavelengths that humans can actually see. In fact, sunlight is made up of a spectrum of electromagnetic radiation from the infrared to the ultraviolet. When sunlight is incident on the atmosphere, each of the wavelengths acts in a different manner. Some of the energy is reflected back into space or absorbed by the atmosphere. The amount which is partitioned into each depends on the wavelength in relation to the chemical components of the atmosphere. The reflected component is known as atmospheric scatter. The sunlight that penetrates the atmosphere is then transmitted to the ground, where it is also either reflected or absorbed. The amount of light which is reflected and the wavelengths which are reflected depend on the composition of the material which the light strikes. Remote sensors record the reflected radiation that is received from Earth. If the sensor is in space then the light once again encounters the atmosphere on its journey to the sensor. By analyzing the information picked up by the remote sensors from the reflected wavelengths, we can determine the nature of the surface from which the light was reflected. In essence, this is exactly what we are doing when we are looking at any object. Our brain analyses the wavelengths received from the object and assigns it an identity based on the spectral and other information, such as texture, colour, shape, etc.

2.0.2 Value of Multispectral Sensors

In the past, geological mapping has been accomplished using only the human eye for rock identification either in the field or with aerial or satellite images. This means that mineral detection could only be accomplished using the reflected sunlight in the visible wavelength region of the electromagnetic spectrum: the only bands that people can see. However, the astounding array of mineral compositions occurring in nature results in reflected light from many different wavelength regions that fall outside the range of human detection. Thus, multispectral sensors such as ASTER are especially valuable for geological mapping applications. They collect data from a wide range of wavelengths that humans cannot detect, allowing for more precise mineral identification. Taking the isolation of this study area into account, ASTER data are an ideal source of information.

2.0.3 Attainment of ASTER Data

ASTER Data can be obtained easily through an online distribution center provided by NASA, known as the Earth Observing System (EOS) data gateway (<http://edcimswww.cr.usgs.gov/pub/imswelcome/>), with several hierarchical formats available for order. Potential ASTER images for this project were evaluated, previewed and ordered online. Data were ordered in the Level 1B format (registered radiance at the sensor), a reconstructed, full resolution version which has been geometrically and radiometrically calibrated (ERSDAC, 2007). The digital number values of each pixel are converted to radiance at the sensor, or spectral radiance and are reported in units of radiance:

$$\frac{W}{m^2 \times sr \times \mu m} \quad (2.1)$$

where W is the power emitted in Watts, m^2 is the surface area measured, μm is the wavelength in micrometers, and sr is angle subtended by the aperture of the lens in steradians (the solid angular measurement) (ERSDAC, 2005).

2.1 METHODS

2.1.1 Image Selection

Several criteria were used to choose appropriate images for mapping lithology. Cloud, snow and vegetation cover limit the amount of lithological information available from the images. Thus only those images with minimal cloud and snow cover were considered. Clouds and vegetation cover are more abundant during the summer monsoon months (July-September); also snow tends to accumulate during these months (Watts et al, 2005). Hence, images were inspected from the drier winter months in order to minimize these effects as much as possible. Land coverage is also an issue, as each image must be purchased individually, and may not cover all of the desired study area. Due to the nature of the ASTER flight path it is not conventionally possible to acquire neighbouring images that were taken at the same time, as they may have been taken up to several years apart. The images left to choose from were quite restricted after cloud and snow cover were taken into account; fortunately we were able to find several good images which extended over the whole study area and had minimal cloud and snow coverage (Figure 2.1; Table 2.1).

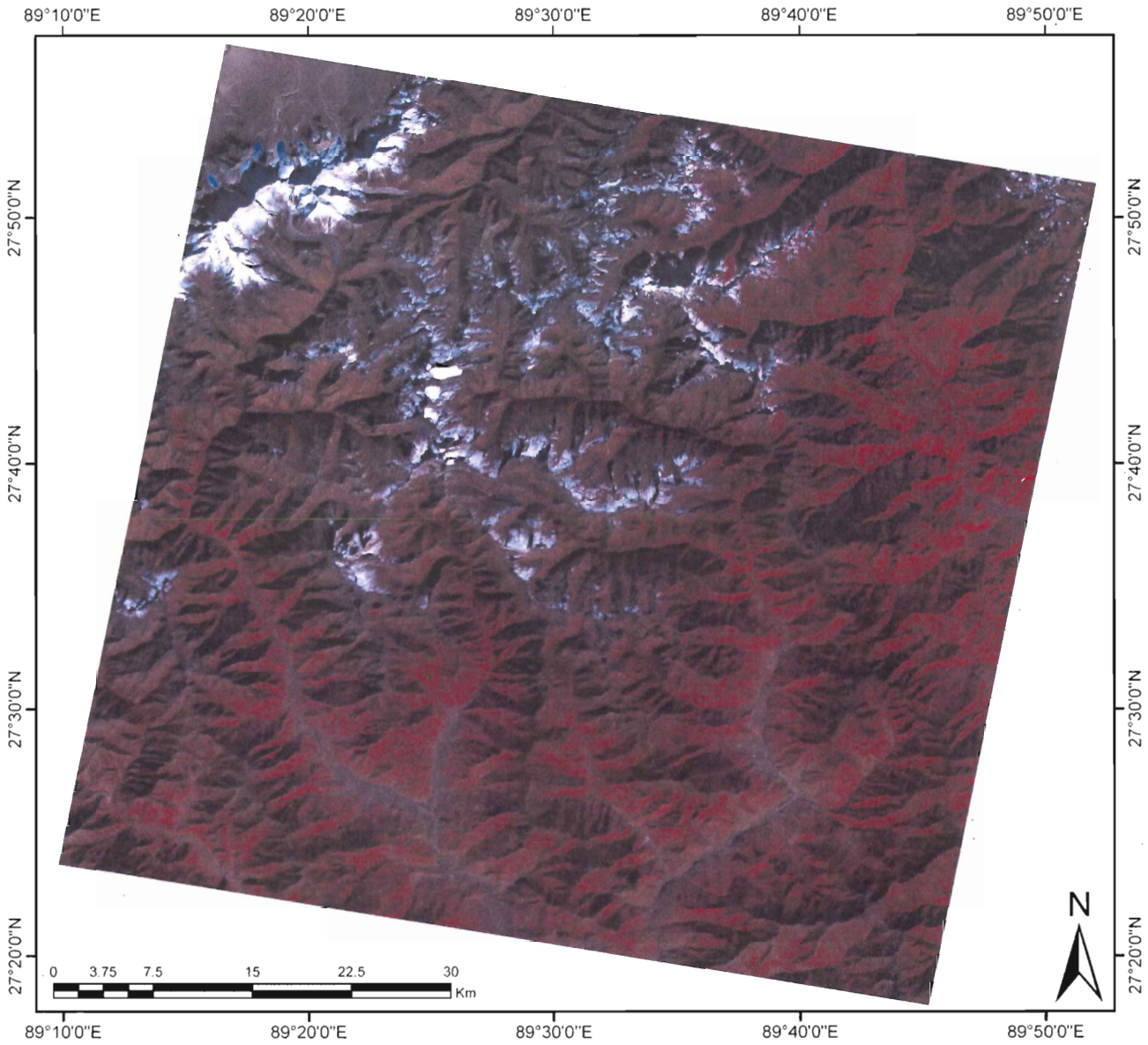


*Figure 2.1: False colour composite image formed using ASTER bands 1 through 3 depicting the study area in NW Bhutan (Data have been expanded, windowed and atmosphere corrected) and demonstrating the appearance of the data (see text for detailed explanations).
Projected in: GCS_WGS_1984. (Exported from ArcMAP)*

Table 2.1: List of all the ASTER images purchased for the NW Bhutan and Sikkim study areas and their coverage statistics.

Image Location	Date acquired by ASTER	Time image was acquired	Extent (approximate)		Centre Point	Coverage ($l \times w$ in km)	Area (km^2)	Purchase Date
			Latitude	Longitude				
NW Bhutan	Jan-06-2005	4:52 PM	27.29° N -27.96° N	89.09° E -89.94° E	27.62° N, 89.52° E	73 × 83	6050.3	Sept-13-2007
E Sikkim	Nov-01-2000	5:00 PM	27.60° N -28.26° N	88.53° E -89.38° E	27.93° N, 88.95° E	72.1 × 82.8	5973.6	Jan-24-2008
NW Sikkim	Dec-13-2001	4:56 PM	27.99° N -28.66° N	88.13° E -88.98° E	28.32° N, 88.55° E	73.4 × 82.7	6071.1	Jan-24-2008
SW Sikkim	Nov-27-2001	4:57 PM	27.46° N -28.13° N	87.93° E -88.79° E	27.80° N, 88.36° E	73.5 × 84.2	6189.8	Jan-24-2008

The processing methods were determined using the NW Bhutan image, since field data are also available (i.e. Gansser, 1983; field observations by D. Kellett, D. Grujic and co-workers). The processing procedure determined on this scene was then applied for the area in N Sikkim where no field observations are available. Several techniques were tested to determine the best method for extracting surface reflectance, and therefore lithological information, from the images (Section 2.1.3).

2.1.2 Pre-processing

The ASTER data for NW Bhutan were imported into the GIS program *Idrisi Kilimanjaro* for processing. The data arrive in a format where each band from 1 to 14 comprises a different image. Since the various spectral ranges come in three different resolutions, the SWIR and TIR images (at 30 m and 90 m resolution, respectively) were expanded to 15 m resolution, so that the images will contain the same number of pixels. The expansion divides the pixels of the lower resolution images to resemble the resolution of the VNIR images (15 m resolution). It is important to note that this step does not actually increase the resolution of the data; it merely

matches the numbers of pixels to that of the highest resolution so that further processing can be accomplished. All of the images are then windowed to the same extent, to eliminate background pixels of zero value, which may interfere with later analyses. The images of NW Bhutan were windowed to cover an area from 27.40° to 27.95° N and 89.16° to 89.87° E, so that the image now has dimensions of approximately 72 km × 78 km, and covers an area of 5664.4 km². Since the Sikkim images are not geo-referenced, their dimensions currently remain unknown.

Atmospheric scatter is taken into account by applying an atmospheric correction to each image using the dark object subtraction method. To accomplish this, a histogram is plotted of all the digital number (DN) values in each image, and the lowest value is recorded (Figure 2.2). The DN is an integer value from 0 to 255 that is assigned to each pixel to represent a unique radiance range. Since the radiance collected is essentially a continuous number it must be broken into intervals, or digitized (or assigned a digital number) in order to be recorded (Vincent, 1997). It is assumed that dark objects in the image will reflect no radiation of their own, resulting in a DN of zero. Any radiation recorded from a dark object would be due to the atmospheric scatter component. The process assumes the presence of dark objects in the image, such as water or cloud shade where the reflectance value is theoretically zero. Thus, the lowest value of the histogram represents the amount of reflectance attributable to the atmosphere received from any dark objects. If this value is brought back to zero, the atmospheric scatter would have been essentially removed. The lowest value of the histogram is therefore taken to be the amount of scatter due to the atmosphere. This value is subtracted from each pixel of the relevant image, restoring the DN to zero. Thus, any effects of atmospheric scattering are isolated and removed.

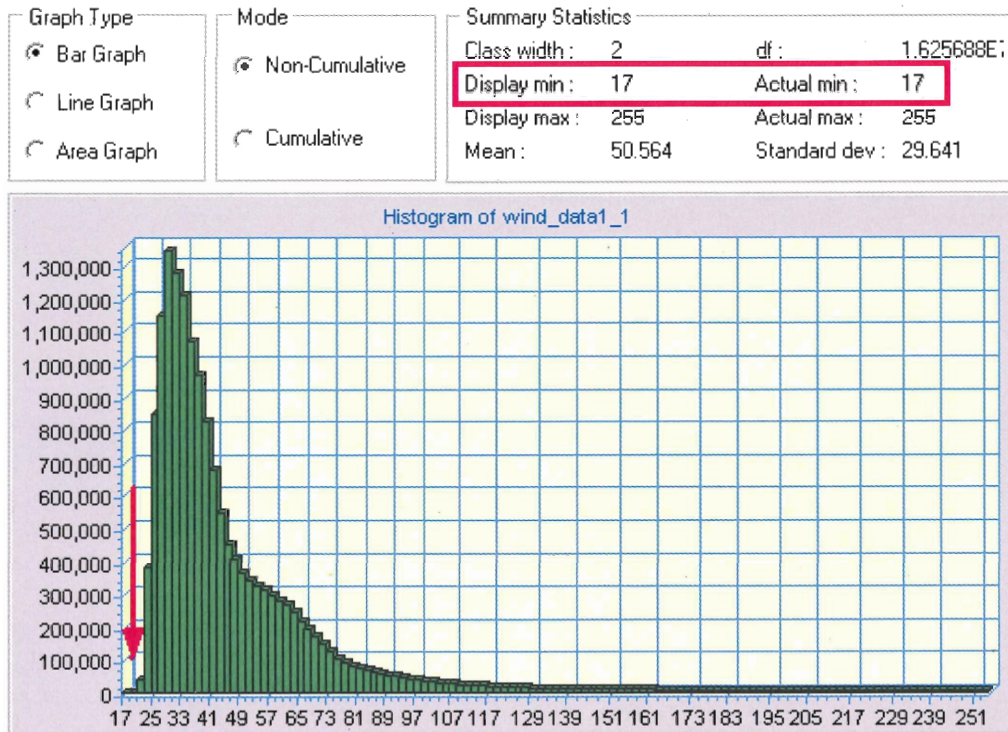


Figure 2.2: An example of a Histogram analysis, performed on band 1 (VNIR) of the NW Bhutan area. X-Axis: Digital Number (DN) assigned to each pixel based on its reflectance values, Y-Axis: the frequency that each DN occurs in the image. The summary statistics are displayed at the top of the graph. The red box in the summary statistics and red arrow on the graph indicate the minimum value. Thus, in this case the scattered component is 17, since this is the minimum DN. (Exported from Idrisi)

2.1.3 Analytical Techniques

Several different techniques were tested to determine the best method for extracting surface reflectance from the images.

A principal component analysis (PCA) was applied to the first 9 bands (VNIR to SWIR) to extract features with comparable surface reflectance (thus containing similar mineral content) from the data. Since the thermal emittance data are not relevant to the present study, the TIR bands are ignored and only the VNIR and SWIR bands were analyzed. PCA identifies the optimum coefficients that account for the maximum variation present in the original dataset

(Campbell, 2007). The result is an image that contains a single band of data which is an optimum representation of all the channels present in the original data. This process also reduces the size of the dataset by eliminating redundancy (Campbell, 2007). To put it simply, the PCA finds patterns in the data, and then displays them to emphasize the similarities and differences between the bands of data. This is especially useful in large data sets such as these, because it reduces the size of the data to more manageable proportions, but still keeps the most important information. Thus, using the coefficients found by PCA from the first nine bands, most of the information can be condensed into a single band. The end result is one image that contains the best depiction of the information present within the original data, making it easy to choose the most useful variables and discard those which may not contribute to the display of information (Campbell, 2007).

The second type of analysis performed was a cluster analysis. Due to intensive computing requirements, only the first seven bands of VNIR and SWIR data were used. Cluster uses a histogram technique to find peaks with greater frequency than the surrounding non-diagonal pixels. Each pixel in the image is then assigned to the nearest peak with divisions of classes placed at the mid points between the histogram classes. Thus, areas of similar attributes are “clustered” together to ideally form an image with groups of comparable reflectance values (thus, lithology) identified and classified together (Figure 2.3). The result of the cluster analysis could then be used for supervised classification methods. Using areas of known lithology as training sites, the software can be told to look for other areas with similar characteristics in terms of radiation reflectance. However, this process tends to be extremely time consuming and requires already detailed knowledge of the field area.

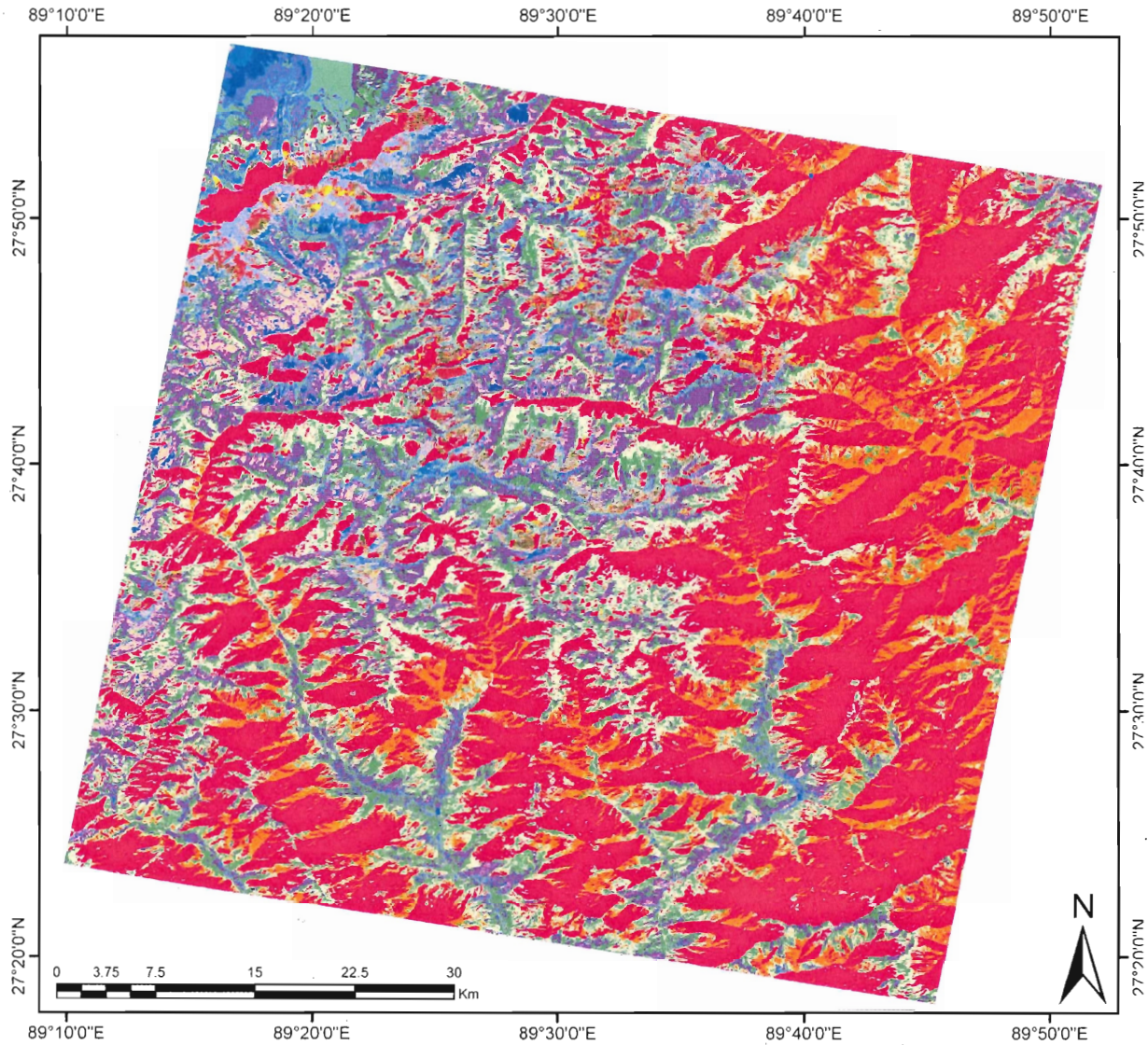


Figure 2.3: Image of cluster analysis, performed on bands 1 – 7 (VNIR-SWIR). Each colour represents an area of similar reflectance values. However, because the analysis does not take topography into account, much of the colour categories are likely from variations in slope deflecting the reflection angle, not actual differences in lithology. For example: the pink colour is likely far-side slope (the slope facing away from the viewer) vegetation, and the orange colour is near-side slope vegetation. The other colours likely represent similar far and near side slope surfaces. Projected in: GCS-WGS-1984. (Exported from ArcMAP)

The third type of analysis performed is the band ratio technique used by Watts et al. (2005) to map the North Himalayan gneiss domes in Southern Tibet. The technique was extended by J.L. Perry & R.K. Vincent (personal communication, 2008), who introduced the brightness and ratio codes for ASTER. Similar codes were developed previously by Vincent (1997) for Landsat data. The ASTER bands are converted to various band ratios using the OVERLAY function, by which the data from two images are combined using an operation (+, -, ×, /, etc.) chosen by the user; resulting in a single new image. For this study, the images are produced by simply dividing the required bands to get the desired ratio, which is especially useful because the ratios enhance chemical composition differences, while suppressing discrepancies in slope, atmospheric haze and illumination angle (R.K. Vincent; personal communication, 2008). It is easiest to interpret a colour composite image of three ratios (where each ratio is assigned blue, red or green).

It is crucial to decide which three ratios should be combined to map the desired lithologies. The concept of ratio codes was developed to solve this problem. Each potential ratio combination is assigned an arbitrary number from 0 to 9, to denote the extent to which that ratio displays the unique spectral characteristics of any particular mineral. A high ratio code (8-9) for a particular mineral indicates that it is among the brightest of the minerals tested for that spectral band, whereas low ratio codes (0-1) indicate the darkest minerals. In essence, a high ratio code will display the selected mineral distinctly, and low ratio codes will be dark for that mineral. The numbers 0-9 are chosen to provide ease of use in evaluating the tables and choosing which ratios will differentiate desired minerals. In addition, taking the reciprocal of any particular ratio will give the opposite code value. For example, if a particular ratio has been assigned a code of 9, taking the reciprocal of that same ratio will give a code of 1. Thus the highest and lowest ratio

codes can be chosen for the relevant minerals to be loaded into a composite image. In practice, the highest ratio codes for the target mineral are displayed as red, and then two ratios with lower codes are displayed as blue and green respectively. Thus, on the composite image the target mineral shows up as red (or a combination of colours including red, if there is interference from other minerals), enabling one to isolate areas where the relevant mineral is abundant. Different colour combinations can be chosen, for example ratios with high codes can be loaded into red and green and a low code for blue, so that the target mineral will display as yellow (R.K. Vincent; personal communication, 2008). This process is repeated for each likely mineral in the study area. Each combination may potentially discover several different minerals, so the codes must be chosen carefully to avoid repetition, as well as eliminate the possibilities of “false alarms” (minerals with similar codes).

It was found that the principle component analysis did not result in a spectrally discriminative result, and therefore the technique was not investigated further. The cluster analysis proved to be too excessively influenced by topographic and solar angle variations. Thus the band ratio method was chosen as it tends to be the most efficient and practical system and followed the same trend as previous studies, allowing us to utilize and expand upon their techniques.

2.1.4 Processing Procedure

The specific minerals and proportions present in each outcrop desired to be differentiated were identified based on field observations by Gansser (1983), D. Kellett and D. Grujic. Ratio codes have been assigned for many popular rock-forming minerals through experimental lab

procedures by Vincent (Table 2.2). Several combinations of ratios were chosen to image the different minerals seen in each lithology of the Bhutan field area (Table 2.3). In this scheme, albite and the K-spars are most commonly associated with migmatites and leucogranites (GHS). Biotite is common in the gneisses and schists of the GHS and also within the basal Chekha formation. Muscovite may be found in the leucogranites and smaller amounts within the GHS gneisses. The carbonates are present in some Tethyan sediments and in the limestone facies of the Chekha formation. Graphite is common in the Mesozoic sediments of the TSS, especially in the Cretaceous (Upper Mesozoic) slates. The goethite and hematite occur as alteration products on the surface of the black shale (Upper Mesozoic Tethyan). Since the ASTER instrument records data reflected from the surface, it is constructive to look for these weathering products in addition to the primary minerals of the unit. Quartz is common in the Chekha formation, but also in the GHS (See Figure 1.11 for the detailed geological map of the units we wish to identify). The band ratio codes for each mineral are analyzed and ratios are chosen which represent the highest and lowest codes for each mineral (Table 2.2). These ratios are then assembled into composite images according to the procedure outlined previously (Section 2.1.3). The combinations of ratio used for this study and their classification as the red, green, or blue band of the colour composite image created are outlined in Table 2.3.

Table 2.2: Band ratio codes for common minerals visible in outcrop for the study area. (After R.K. Vincent; personal communication, 2008)

Ratios	Albite	Biotite	Calcite	Chlorite	Dolomite	Graphite
2/1	3	5	4	0	6	1
3/1	3	7	4	0	6	6
4/1	3	9	3	8	4	6
5/1	4	9	3	9	3	7
6/1	4	9	3	9	3	7
7/1	4	9	2	8	1	7
8/1	4	9	2	8	2	8
9/1	4	9	3	8	3	8
3/2	4	8	4	2	6	7
4/2	3	9	3	9	4	7
5/2	4	9	3	9	3	7
6/2	4	9	3	9	2	7
7/2	4	9	2	9	1	7
8/2	4	9	2	9	2	8
9/2	4	9	3	9	3	8
4/3	2	9	3	9	3	7
5/3	4	9	3	9	3	7
6/3	4	9	3	9	2	7
7/3	5	9	2	9	2	7
8/3	5	9	2	9	2	8
9/3	4	9	3	9	3	8
5/4	6	9	4	9	3	8
6/4	5	9	5	9	3	8
7/4	7	9	3	9	2	9
8/4	6	9	2	8	2	9
9/4	6	9	4	9	3	8
6/5	2	8	5	2	1	7
7/5	6	8	1	0	0	7
8/5	4	7	0	0	1	8
9/5	5	8	3	2	3	8
7/6	8	6	1	0	0	7
8/6	7	6	0	1	1	8
9/6	6	8	3	2	4	8
8/7	4	6	0	2	5	8
9/7	4	7	9	8	9	8
9/8	3	7	9	9	9	7

Table 2.2 (Continued): Band ratio codes for common minerals visible in outcrop for the study area. (After R.K. Vincent; personal communication, 2008)

Ratios	Hematite	Microcline	Muscovite	Orthoclase	Quartz	Goethite
2/1	9	8	7	4	6	9
3/1	9	7	6	3	7	9
4/1	9	6	6	4	7	9
5/1	9	6	4	5	7	9
6/1	9	6	2	5	7	9
7/1	9	6	5	5	8	9
8/1	9	6	3	5	8	9
9/1	9	6	3	6	8	9
3/2	8	6	6	4	8	9
4/2	7	6	6	4	7	8
5/2	7	5	3	5	7	8
6/2	7	5	2	5	7	8
7/2	7	6	4	5	7	8
8/2	7	5	3	6	7	8
9/2	7	5	2	5	7	8
4/3	6	6	6	4	7	8
5/3	6	5	3	6	7	8
6/3	6	4	2	6	7	8
7/3	7	5	4	6	7	8
8/3	7	5	3	6	7	8
9/3	7	5	2	6	7	8
5/4	8	4	2	7	7	8
6/4	8	3	1	7	8	7
7/4	8	5	3	7	8	7
8/4	8	5	2	8	8	7
9/4	8	5	2	8	8	6
6/5	7	1	0	5	6	3
7/5	7	7	8	5	5	4
8/5	8	4	3	6	7	4
9/5	8	5	2	7	7	5
7/6	7	8	9	5	5	5
8/6	8	7	9	6	7	4
9/6	8	6	6	7	8	5
8/7	8	3	1	7	7	5
9/7	8	3	1	7	7	4
9/8	7	3	2	5	6	3

Table 2.3: The band ratio combinations chosen to image the lithologies in the study area. The band ratios are loaded into a colour composite image in which each is chosen to represent the red, green or blue parts. The ratios displayed for red in each composite image have high codes; the ratios for blue and green have low codes. The exception is chlorite (2), which has ratios with high codes for red and green, and a low-code ratio for blue. For pictures of the composite images used see Figures 2.4 – 2.9.

Mineralogy	Red	Green	Blue
Chlorite (1) (Figure 2.4)	6/2	3/1	2/1
Chlorite (2) (Figure 2.5)	4/3	5/3	2/1
Muscovite (Figure 2.6)	7/6	6/5	6/4
Carbonates (1) (Figure 2.7)	9/7	7/1	7/2
Carbonates (2) (Figure 2.8)	7/6	4/3	6/5
Feldspar (Figure 2.9)	2/1	4/3	7/4

The created ASTER composite images were projected on top of the Geological Map of Bhutan (Gansser, 1983) in order to compare the band ratios to the current lithological boundaries (Figures 2.4 - 2.9). In addition, a false colour composite image was created in order to view zones with the most extensive outcrop and eliminate glaciers and areas of snow (Figure 2.1). An additional snow overlay was created by choosing the representative DN for snowy areas, and reclassifying the image to only display the snow (details are given in Appendix I). A vegetation index analysis was performed to find areas of coarse vegetation, to be overlain visually onto the composite images (Figure 2.10). The vegetation index indicates green vegetation through a combination of the visible red and near-infrared bands of the ASTER data. The module used is a simple numerical index known as NDVI (Normalized Difference Vegetation Index). The model exploits the concept that live, green plants use solar radiation for photosynthesis. The leaf cells have evolved to scatter light in the near-infrared region (NIR) and are most efficient at absorbing red light. Thus, the bands corresponding to the red and NIR ranges are combined in the following fashion:

$$NDVI = \frac{NIR-RED}{NIR+RED} \quad (2.2)$$

where NIR represents band 3 and RED represents band 2 for ASTER data (Campbell, 2007).

The result is an image that shows the location of green vegetation (Figure 2.10).

The ASTER images were geo-referenced, using prominent topographic features (e.g. mountain peaks, confluences, etc) identifiable accurately on both images as control points. Once overlain, the ASTER images can be compared to areas of known lithology on the Gansser map and field observations by D. Kellett, D. Grujic, and C. Warren, to distinguish the spectral signature of the various lithologies. Thus, the band ratios can be correlated with the established boundaries to ensure that they accurately represent reality. The areas of similar lithology are digitized as polygons in ArcMAP, essentially mapping colour variations in the composite images. Areas of similar classification correlating to field-identified litho-tectonic packages have then been mapped to produce a more accurate geological map of the study area.

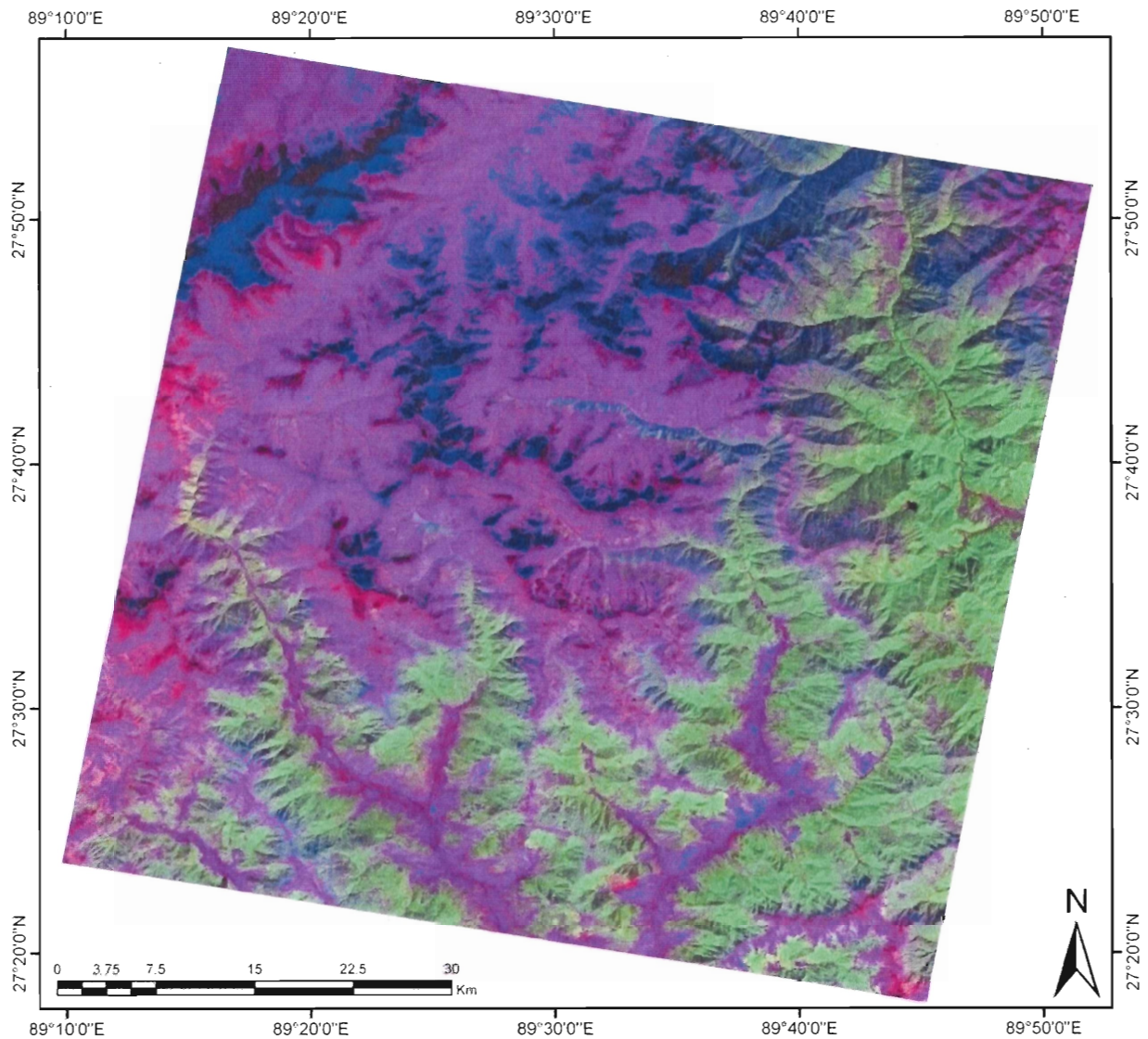


Figure 2.4: The Chlorite (1) image (Table 2.3), one of the composite images created to map lithologies. The image is a composite where: $R = 6/2$, $G = 3/1$, $B = 2/1$, which will differentiate areas based on chlorite content. In this case, green / greenish-blue = vegetation, bright blue = snow, purple = alluvium, pink = Chekha, dark-blue = TSS. Projected in: GCS-WGS-1984. (Exported from ArcMAP)

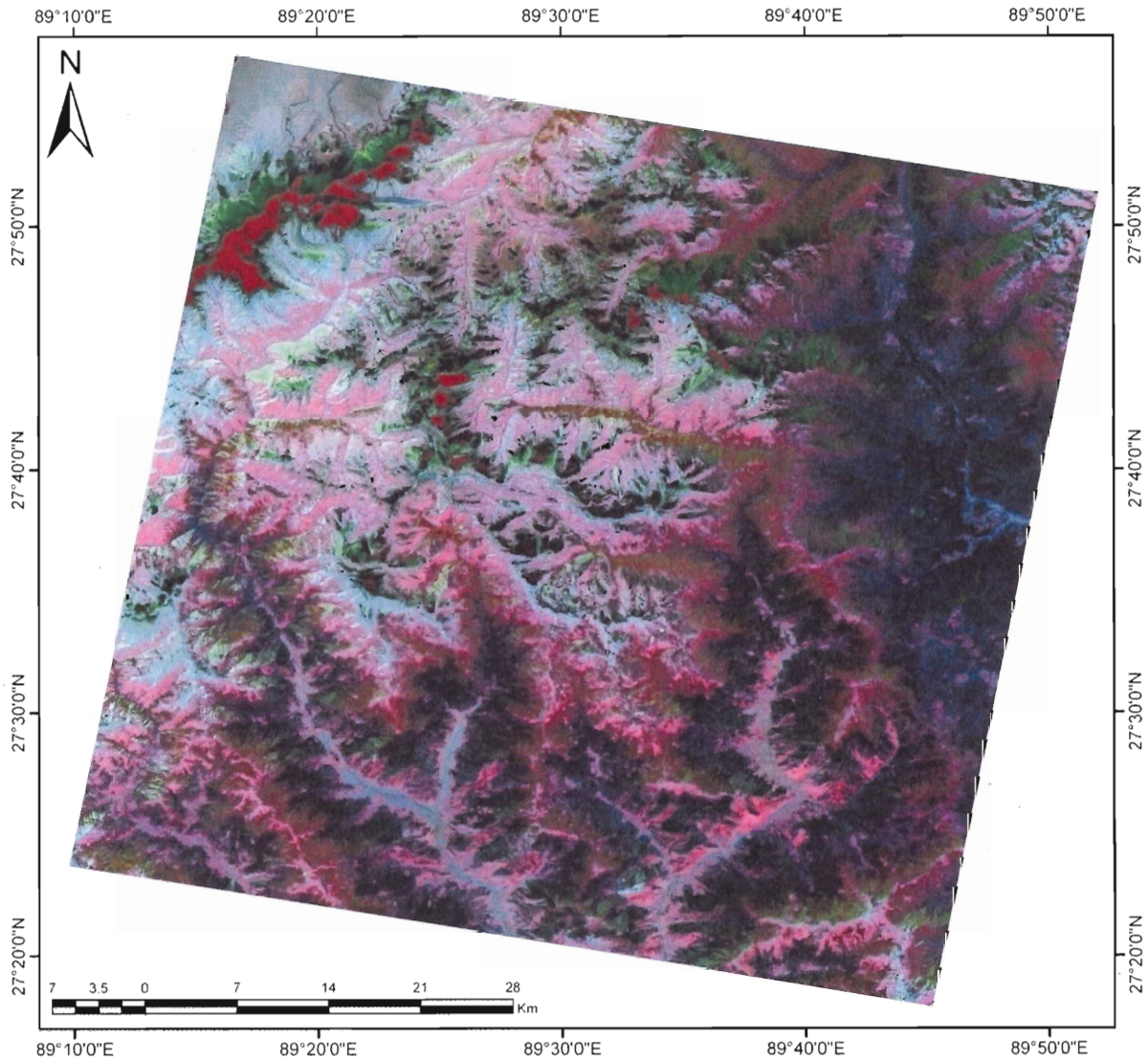


Figure 2.5: The Chlorite (2) image (Table 2.3). In this case, pink = soil, black and dark red = vegetation, bright red = snow, brownish-red = L.Mesozoic TSS, cyan + red = Paleozoic TSS. Cyan = other lithologies, undifferentiated. Projected in: GCS-WGS-1984. (Exported from ArcMAP)

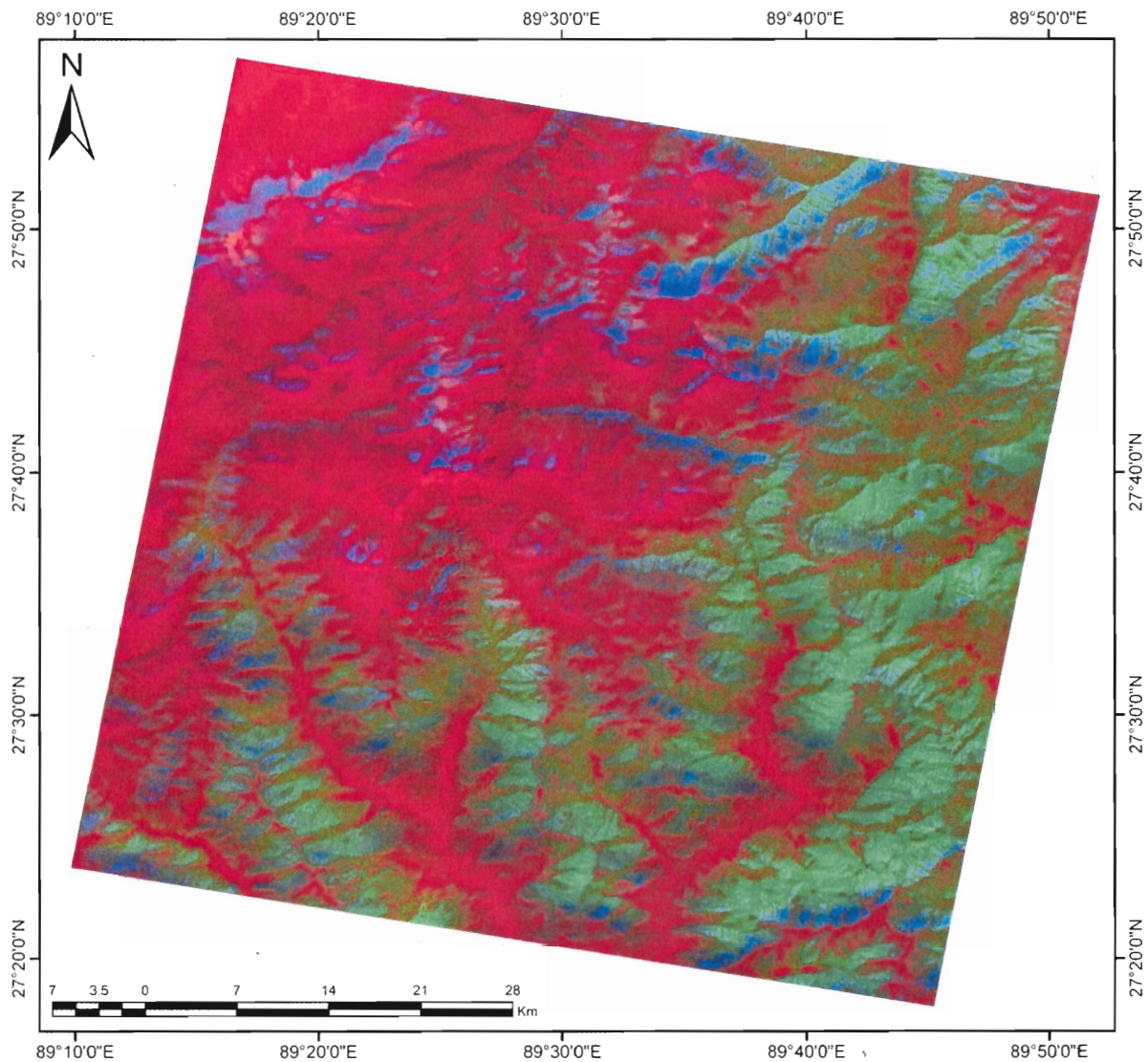


Figure 2.6: The Muscovite composite image (Table 2.3). This image did not prove to be as useful as the others, but was tried based on the study by Watts et al. (2005). The colours are not very separable, everything has shown up as a fairly uniform red, except for vegetation which shows as green in this case, and snow which is blue. Projected in: GCS-WGS-1984. (Exported from ArcMAP)

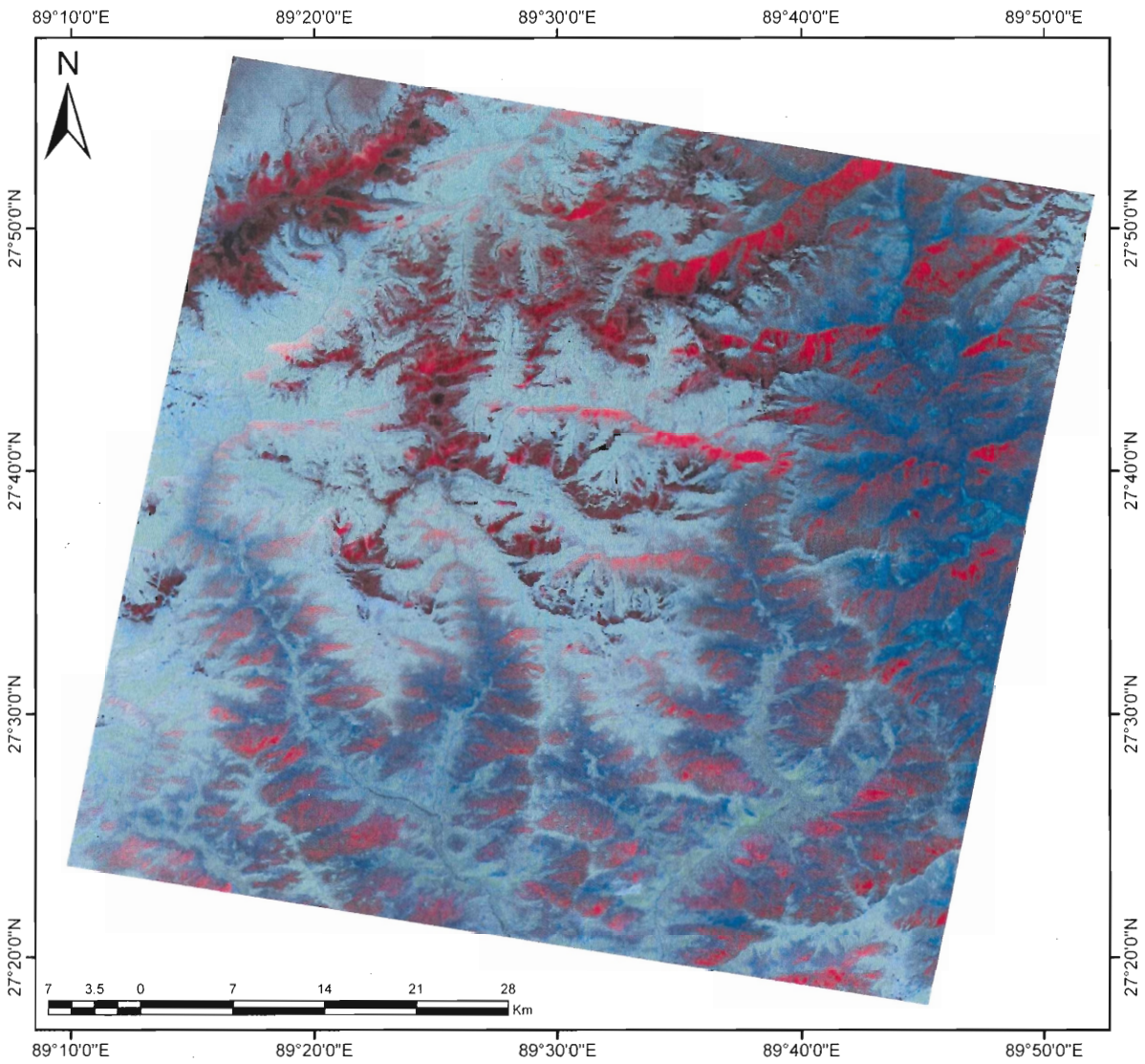


Figure 2.7: The Carbonates (1) composite image (Table 2.3) In this case, bright red = vegetation, medium blue = soil/alluvium, reddish brown = carbonates, dark red = snow. Projected in: GCS-WGS-1984. (Exported from ArcMAP)

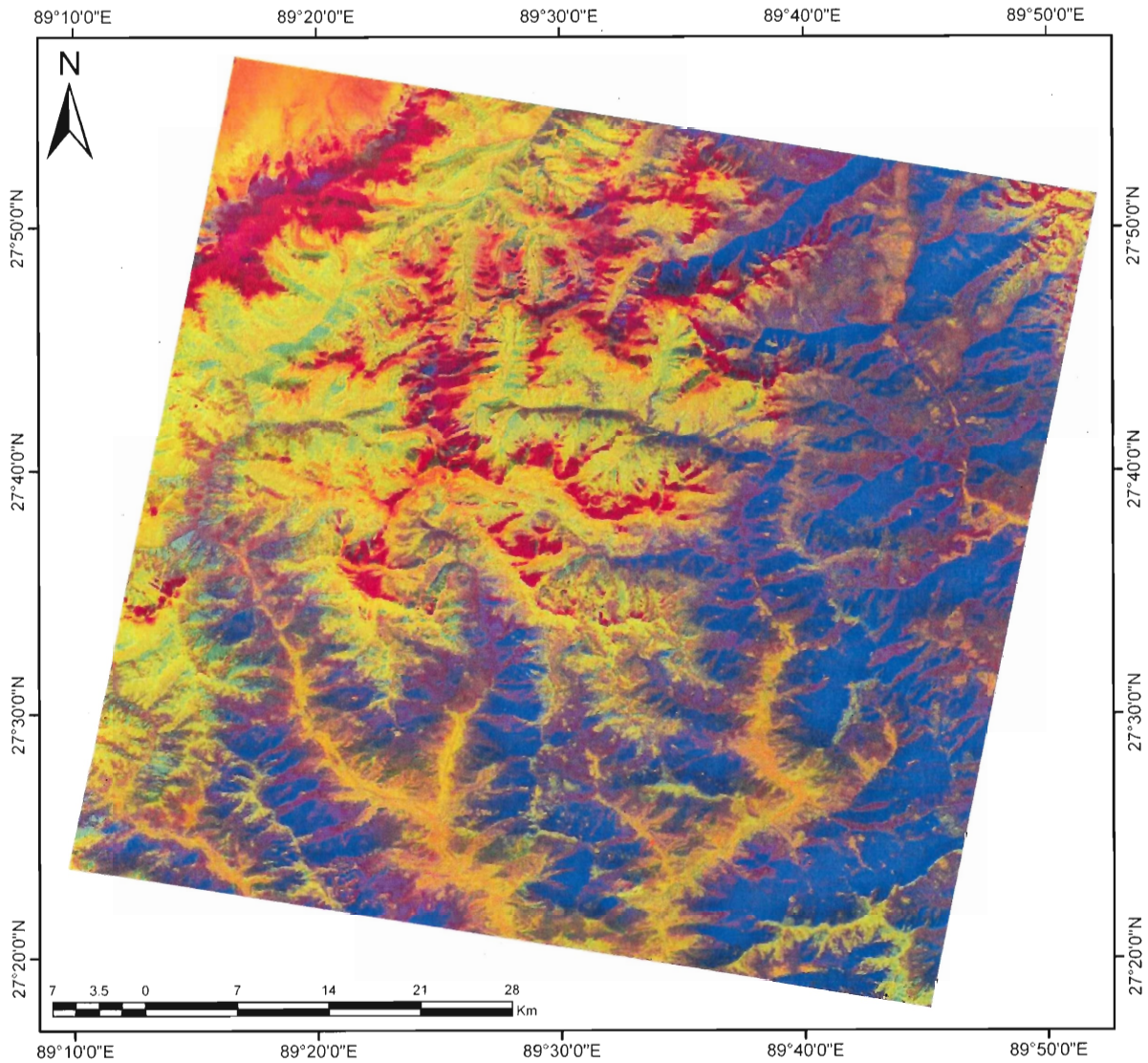


Figure 2.8: The Carbonates (2) image (Table 2.3). In this case, pink = snow, blue + purple = vegetation, yellow = soil. Green = shadow, Bright orange = carbonates, Bright yellow = Leucogranite, Chekha + GHS. Projected in: GCS-WGS-1984. (Exported from ArcMAP)

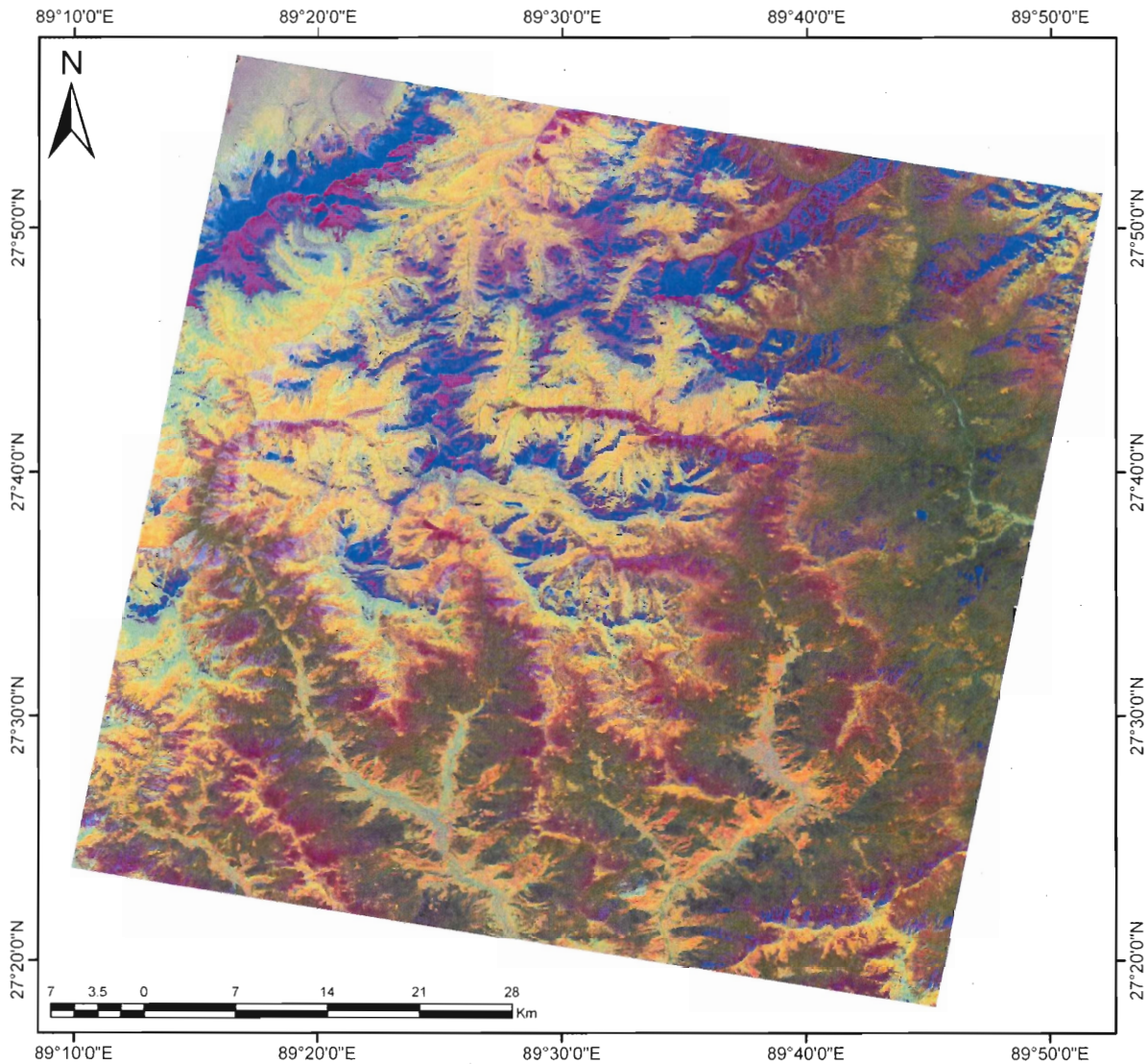


Figure 2.9: The Feldspar composite image (Table 2.3). For this image, purple + dark green = vegetation, pinkish orange = soil, purple + bright blue = snow, Bright green = leucogranite, dark purple = L. Mesozoic TSS, bluish-purple = Paleozoic TSS, cyan + purple = Chekha carbonates, bright greenish-blue = GHS gneisses. Projected in: GCS-WGS-1984. (Exported from ArcMAP)

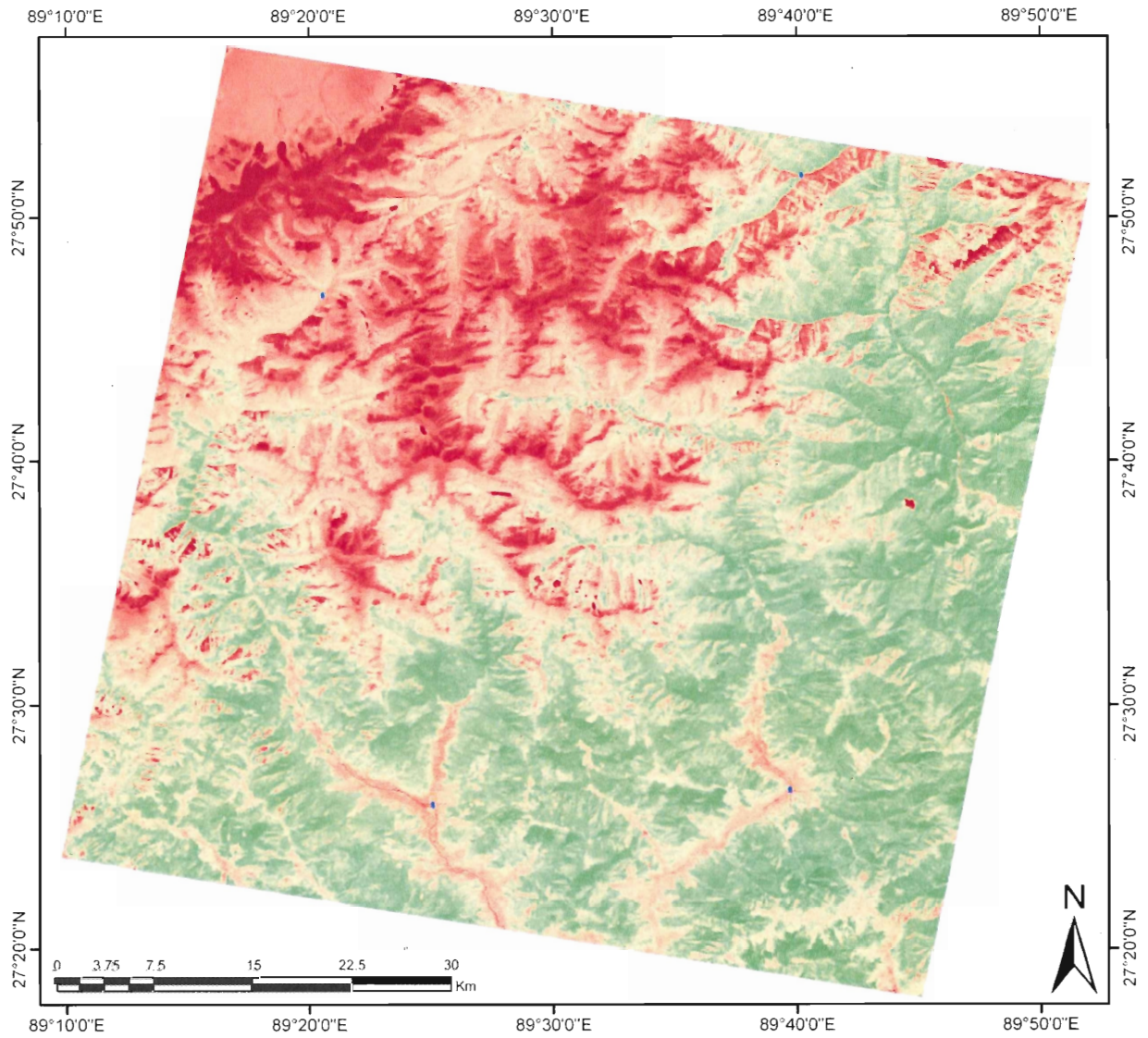


Figure 2.10: An example of the NDVI (Normalized Difference Vegetation Index) performed using bands 2 and 3 (VNIR) to detect vegetation. Areas of coarse vegetation (forest) are shown as dark green. Projected in: GCS-WGS-1984. (Exported from ArcMAP)

2.2 RESULTS

2.2.1 *Lingshi Syncline*

Using the band ratio technique, we were able to differentiate some of the lithologies present in the Lingshi syncline. The images given in Figures 2.4 - 2.9, using the ratios outlined in Table 2.3, were used to make the following distinctions. The limestone facies of the Chekha group was separable from the GHS gneisses and the Paleozoic TSS carbonates. Using the Carbonates (1) composite image the Chekha carbonates display as reddish-brown compared to cyan for the GHS (Figure 2.7). In the Chlorite (1) image, the Chekha carbonates are pinkish-purple and the TSS carbonates are dark-blue (Figure 2.4). The Carbonates (2) image displays the carbonates as orange and the GHS as green/yellow (Figure 2.8). The Lower Mesozoic TSS is distinguishable from the Paleozoic TSS using the Chlorite (2) image (Figure 2.5). The Paleozoic displays as greenish-brown whereas the L. Mesozoic displays as reddish-brown.

The leucogranites were differentiated based upon the feldspar composite image (Figure 2.9). In this image, feldspar is distinguished by a bright green/yellow colour, and carbonates are purple.

The Upper Mesozoic black shale of the TSS were also differentiated, but mainly based upon the absence of feldspar or carbonates. Images to pick up the primary minerals in this unit (i.e. graphite or typical Fe-oxides on weathered surfaces) did not give an unambiguous result, probably due to a lack of extensive outcrop in the area.

The image used by Watts et al. (2005) to find muscovite was also tested (Figure 2.6), however did not give a satisfactory result for this region. This could be due to the presence of other minerals that have similar band-ratio codes interfering with the muscovite signature.

However, since we were able to distinguish the units based on the presence of other minerals, the muscovite image was not needed.

Digitizing the boundaries of some of the units proved to be difficult due to the topography and presence of vegetation in the area. However, it was still possible to refine and alter the lithological boundaries from the current geological map (Gansser; 1983). The lithological polygons drawn from the selected composite images (shown in Table 2.3) are shown below compared to the original map (Figure 2.11 & 2.12).

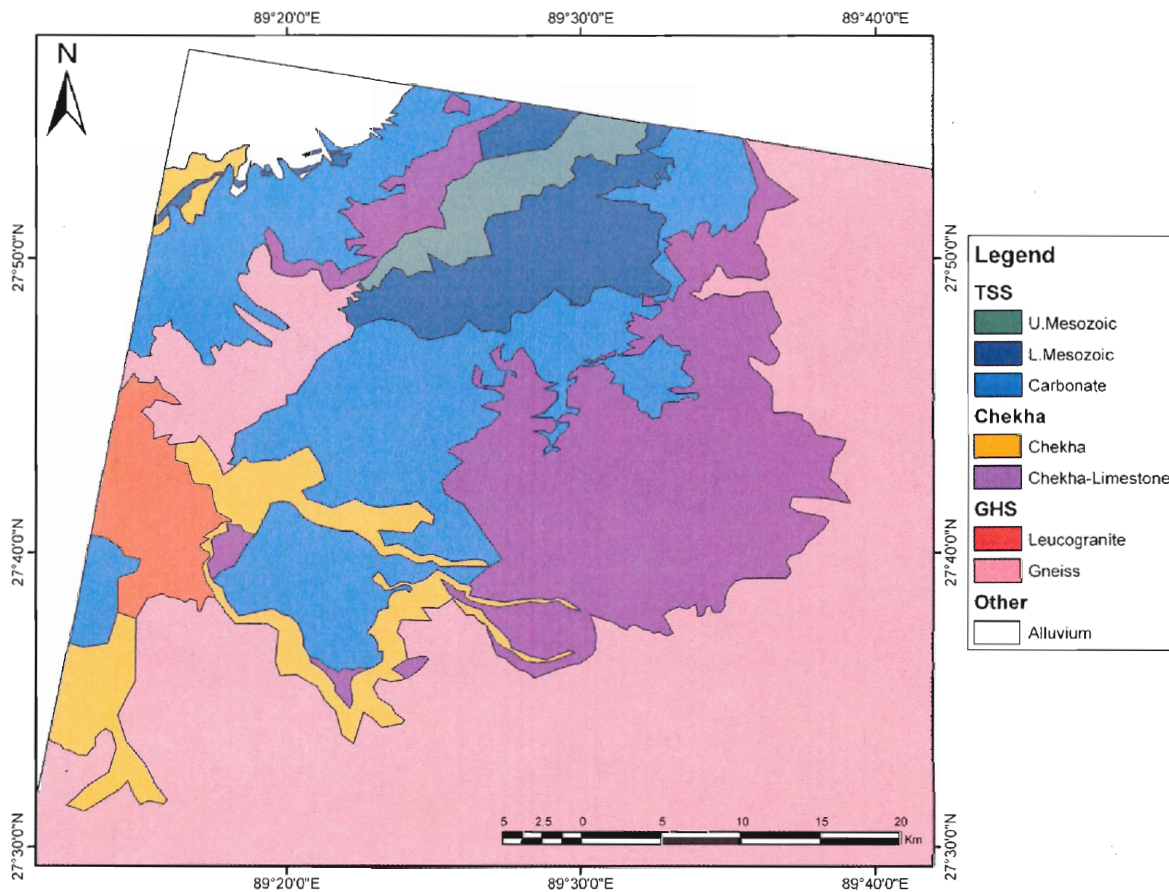


Figure 2.11: The lithological units as drawn from the composite images for the Lingshi Syncline. (Figures 2.4 – 2.9). Projected in: GCS-WGS-1984. (Exported from ArcMAP)

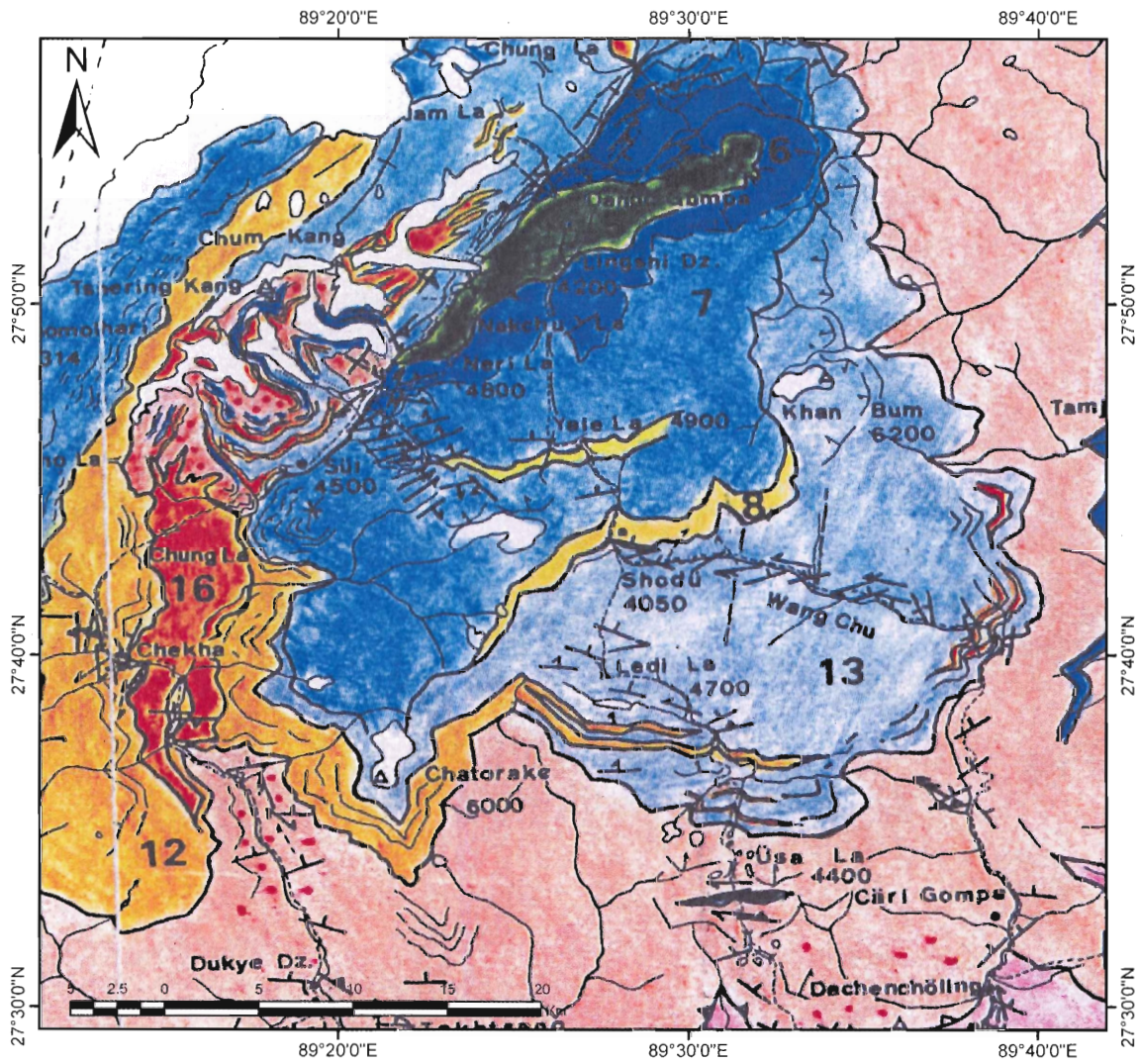


Figure 2.12: Gansser's original map (1983) for the Lingshi Syncline. For legend, refer back to Figure 1.8. Projected in: GCS-WGS-1984. (After Gansser; 1983; Exported from ArcMAP)

The cartographic model of the steps used to make the images from raw ASTER data is given in Appendix I. This gives a standardized set of steps which can be applied to map other regions in the Himalayas with similar lithologies that also remain incompletely mapped.

2.2.2 *Sikkim*

The same band ratios used for the Bhutan area were subsequently applied to the region in northern Sikkim (Study Area #2; Figure 1.9) in order to test the technique. Since the Sikkim area has no field mapping control whatsoever, the Bhutan image serves as the colour code for the mineralogy (as both have similar lithology). Unfortunately, it was not possible to geo-reference the maps from Sikkim because no topographic maps were obtained during this project.

However, to give an idea of the results, some examples of the unprojected composite images are shown in Figures 2.13 – 2.16. The images were referenced to each other and the effects of the band ratio analyses evaluated. Each image is composed of three different ASTER images stitched together, giving it an uneven appearance. The differences in colour arise from acquisition of each ASTER image in differing light conditions. The Sikkim area images gave considerably better results compared to the Bhutan area. The issues of topography and vegetation were not as significant here; hence the images were much easier to interpret. Some of the boundaries can very clearly be seen and differentiated based on colour (Figures 2.13 – 2.16). Once the images have been geo-referenced, polygons can be digitized to represent each lithological unit, with the colour codes taken from the field referenced Bhutan images.

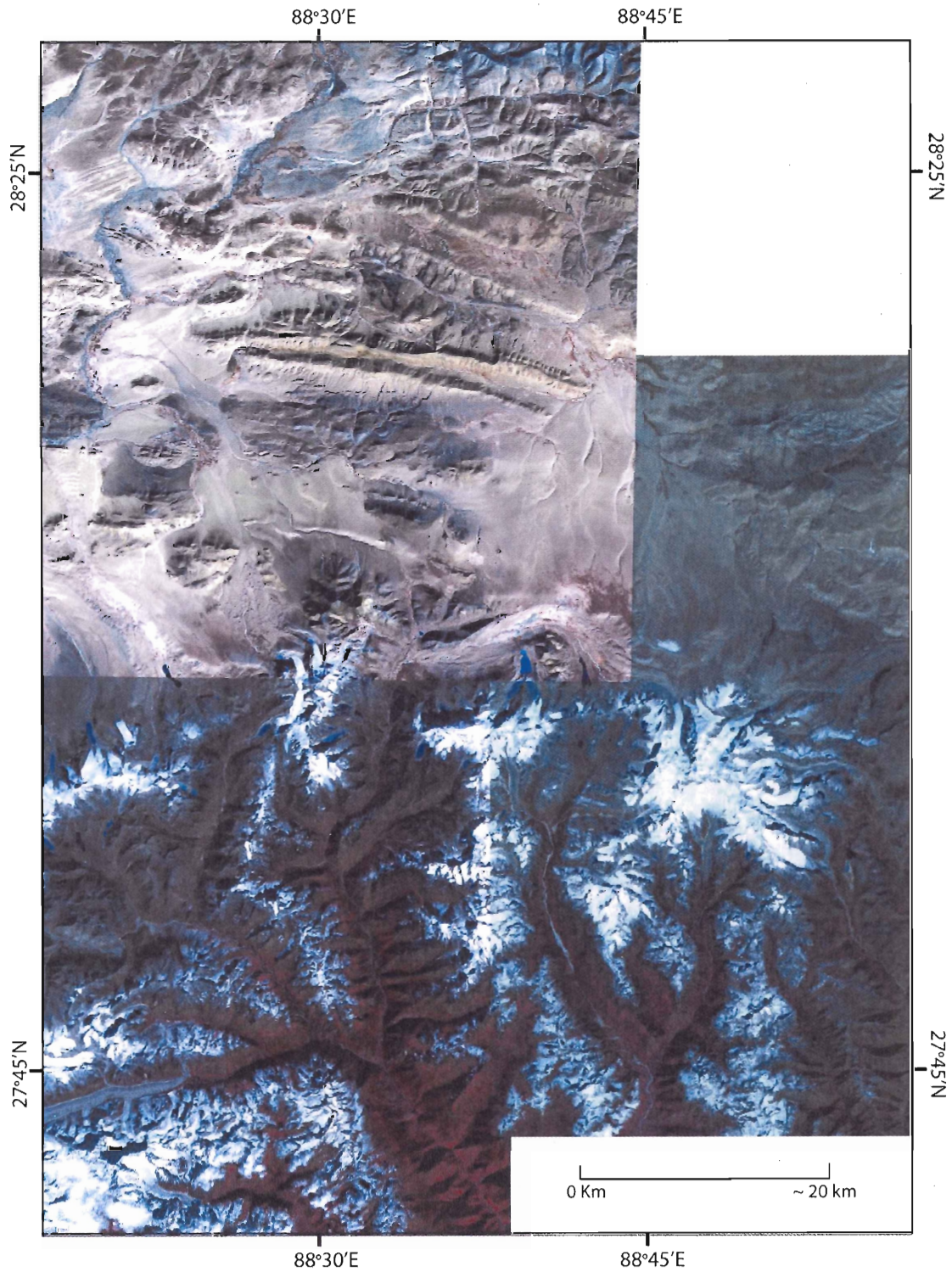


Figure 2.13: False colour composite of the Sikkim area constructed from bands 1, 2 and 3 loaded as blue, green and red respectively. As of March-11-2008, no topographic maps have been purchased for this region, so it is not possible to geo-reference the images. Therefore, the scale bar and coordinates are only approximate.

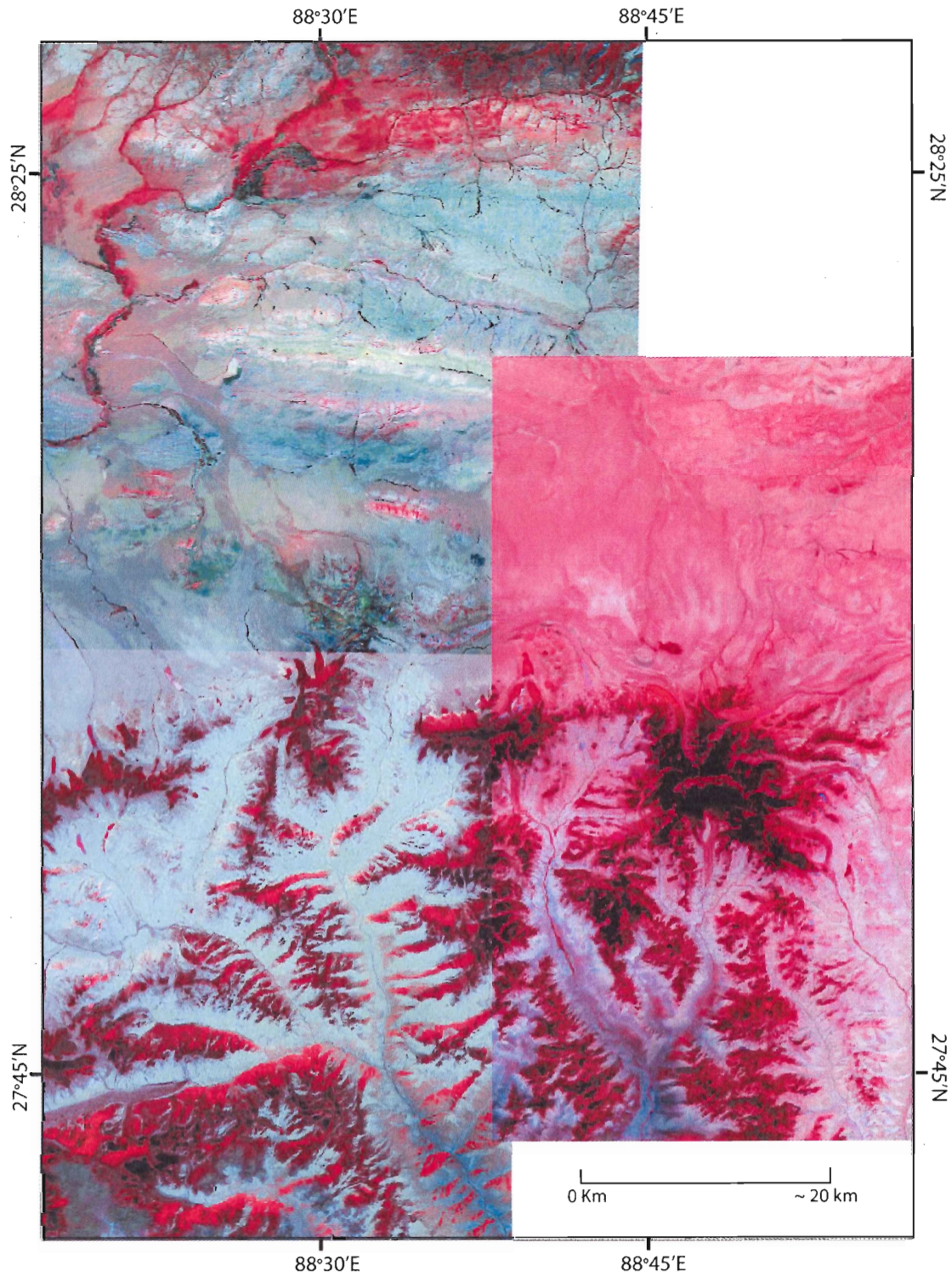


Figure 2.14: Carbonates (1) composite image for Sikkim (Table 2.3). The colours are similar to the Bhutan carbonates (1) image (Figure 2.7), taking into account discrepancies due to time of day the image was acquired. The scale bar and coordinates are only approximate.

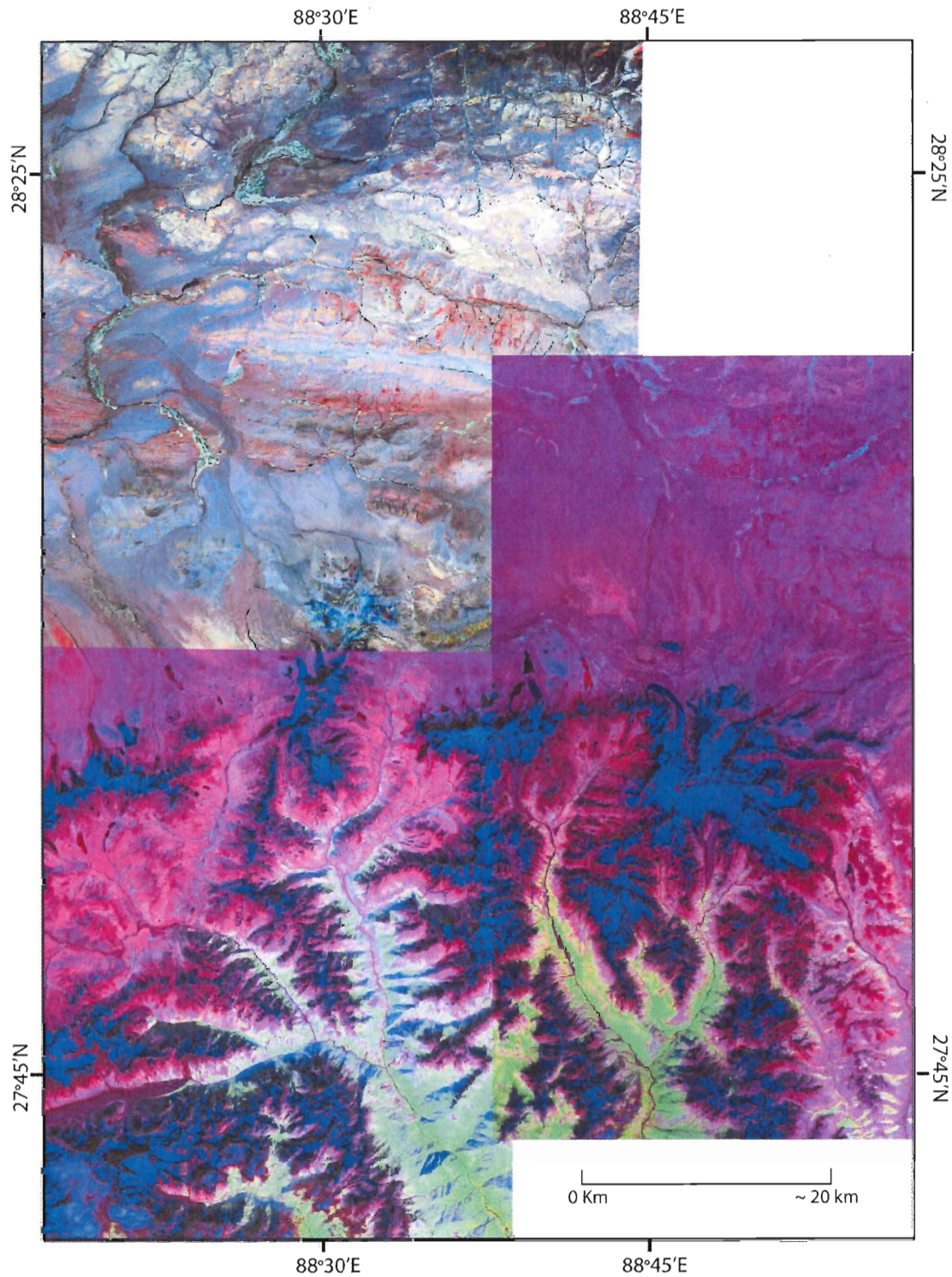


Figure 2.15: Chlorite (1) composite image for the Sikkim area (Table 2.3). The colours are similar to the Bhutan chlorite (1) image (Figure 2.4), taking into account discrepancies due to time of day the image was acquired. The scale bar and coordinates are only approximate.

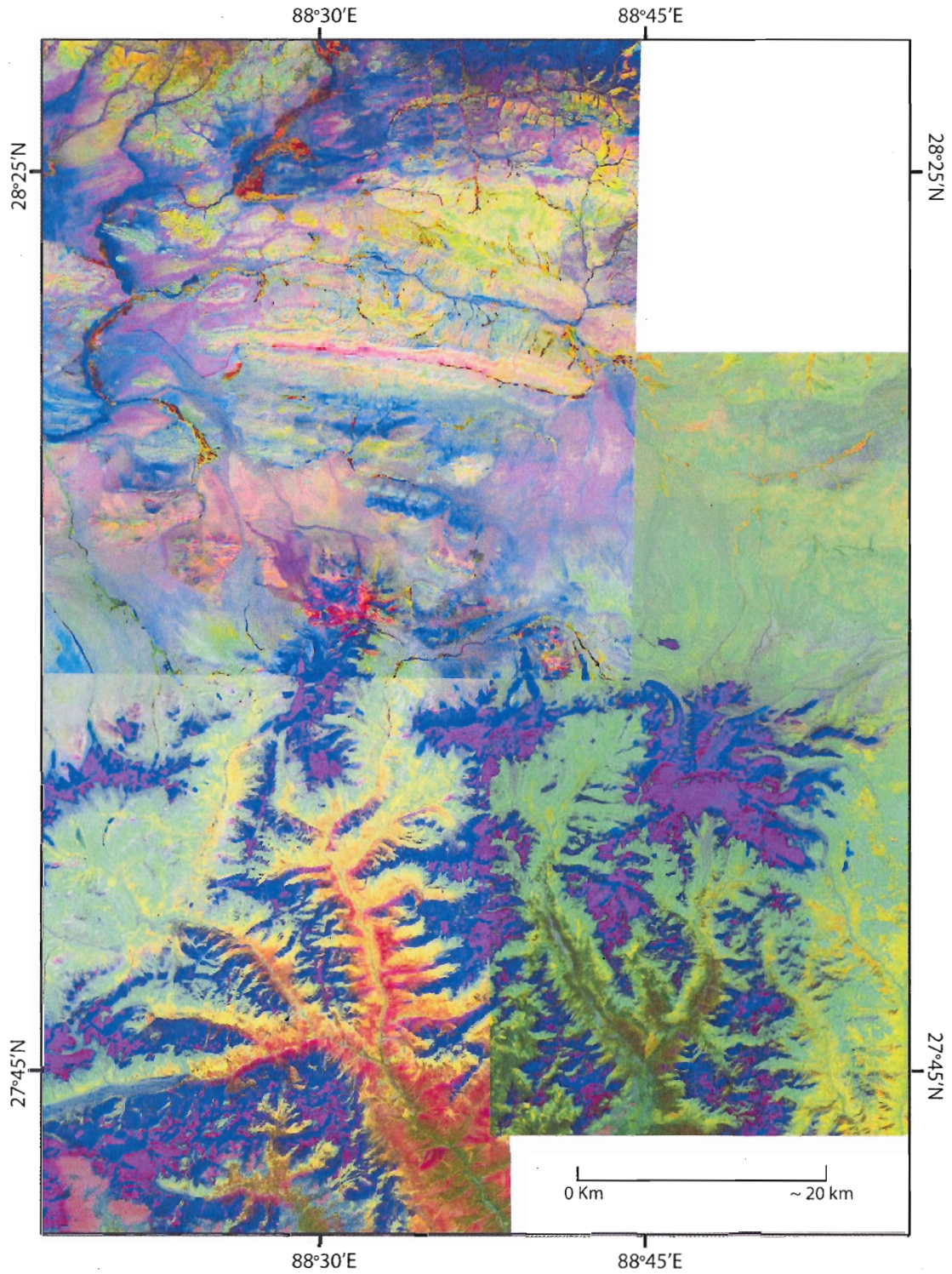


Figure 2.16: Feldspar composite image for the Sikkim area (Table 2.3). The colours are similar to the Bhutan feldspar image (Figure 2.9), taking into account discrepancies due to time of day the image was acquired. The scale bar and coordinates are only approximate.

CHAPTER 3

3.0 GIS DATABASE

3.0.1 Introduction to GIS Database

Before mapping of the region could commence, the initial steps towards complete knowledge of the region involved creating a comprehensive database of all prior field work conducted throughout the area. In addition to the Lingshi Klippe area, data has been gathered from several other key zones of Bhutan. These data have never been published nor projected collectively onto a map. Areas from which data were gathered include most of the country, with quite extensive areas in the east and west, and some areas in the centre.

3.1 FIELD WORK

Field work has been conducted in Bhutan from 1996 to Jan 2007, by Djordje Grujic, his co-workers and graduate students (J. Chakungal, D. Kellett, I Coutand, K. Klepeis and C. Warren). Some of these data have already been discussed in published papers including: Grujic et al., 1996; Davidson et al., 1997; Grujic et al., 2002; Daniel et al., 2003 & Grujic et al., 2006. Wide ranges of data were acquired for many of the access routes in Bhutan; however the points have never been compiled together or projected onto a unique geo-referenced map. The information was separated into several different formats; the station locations, lithological observations, samples gathered from each traverses, as well as structural measurements for foliation and lineation visible in outcrop.

3.2 PROJECTION OF DATA

3.2.1 *Basemap*

Before the data could be projected to actual geographic coordinates, a basemap had to be prepared on which to view the different station locations. As the most current geological map for the region with approximate coordinates, Gansser's map was used as a temporary basemap. However, this map is hand-drawn with the aid of field sketches and some Landsat I images, and does not have an accurate coordinate system or geographic reference. Thus, the map was scanned and imported into ArcMAP, along with a mosaic of topographic maps (1:50,000) available for the region. Prominent topographic features such as confluences, mountain peaks and glaciers were used to register and geo-reference Gansser's Map. The original map is compared to the registered version in Figures 3.1 & 3.2. The slightly skewed nature of the geo-referenced image (Figure 3.2) is a result of stretching the original image (Figure 3.1) by matching major features to geo-referenced, high resolution topographic maps of the region.

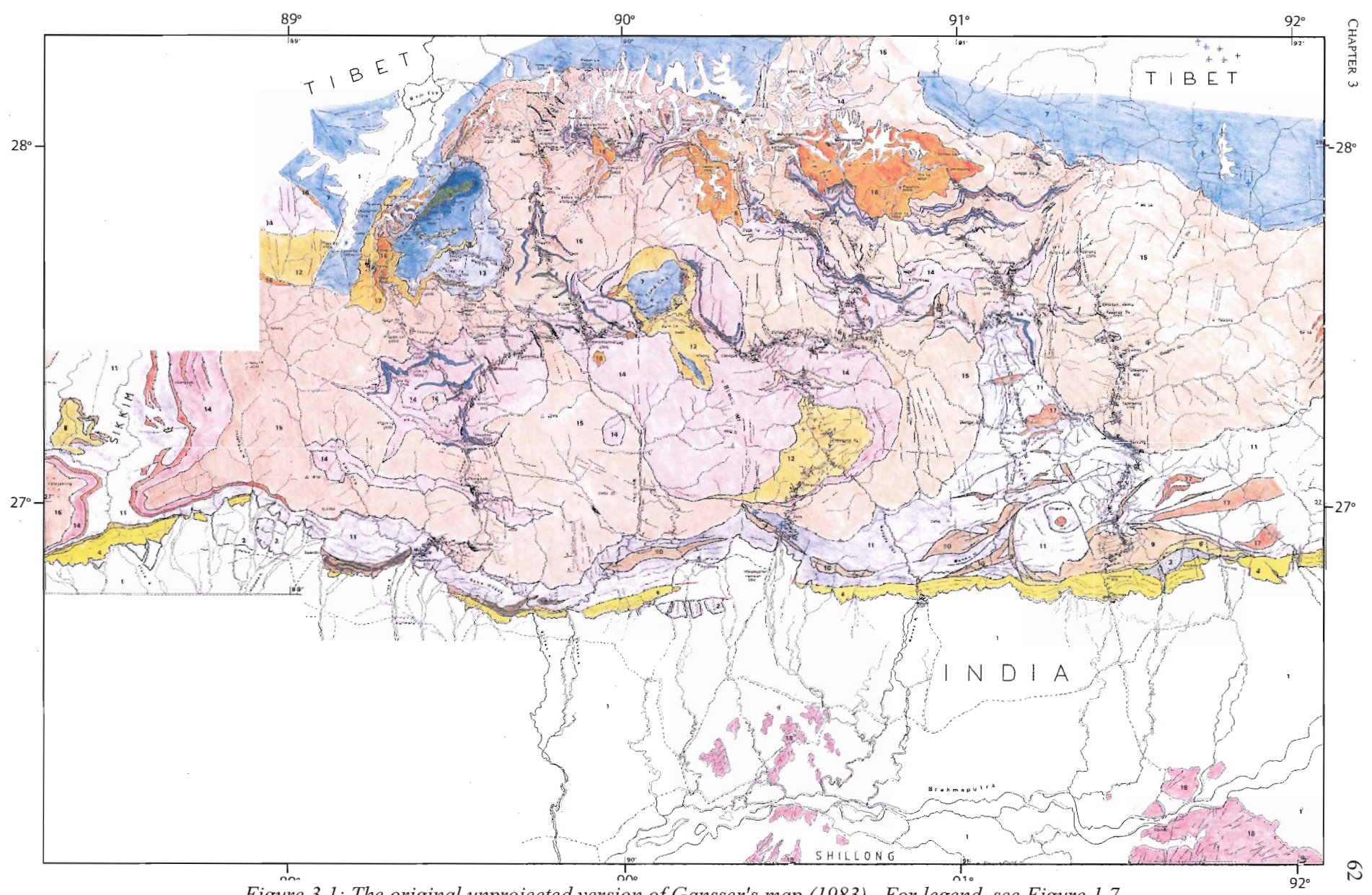


Figure 3.1: The original unprojected version of Gansser's map (1983). For legend, see Figure 1.7.

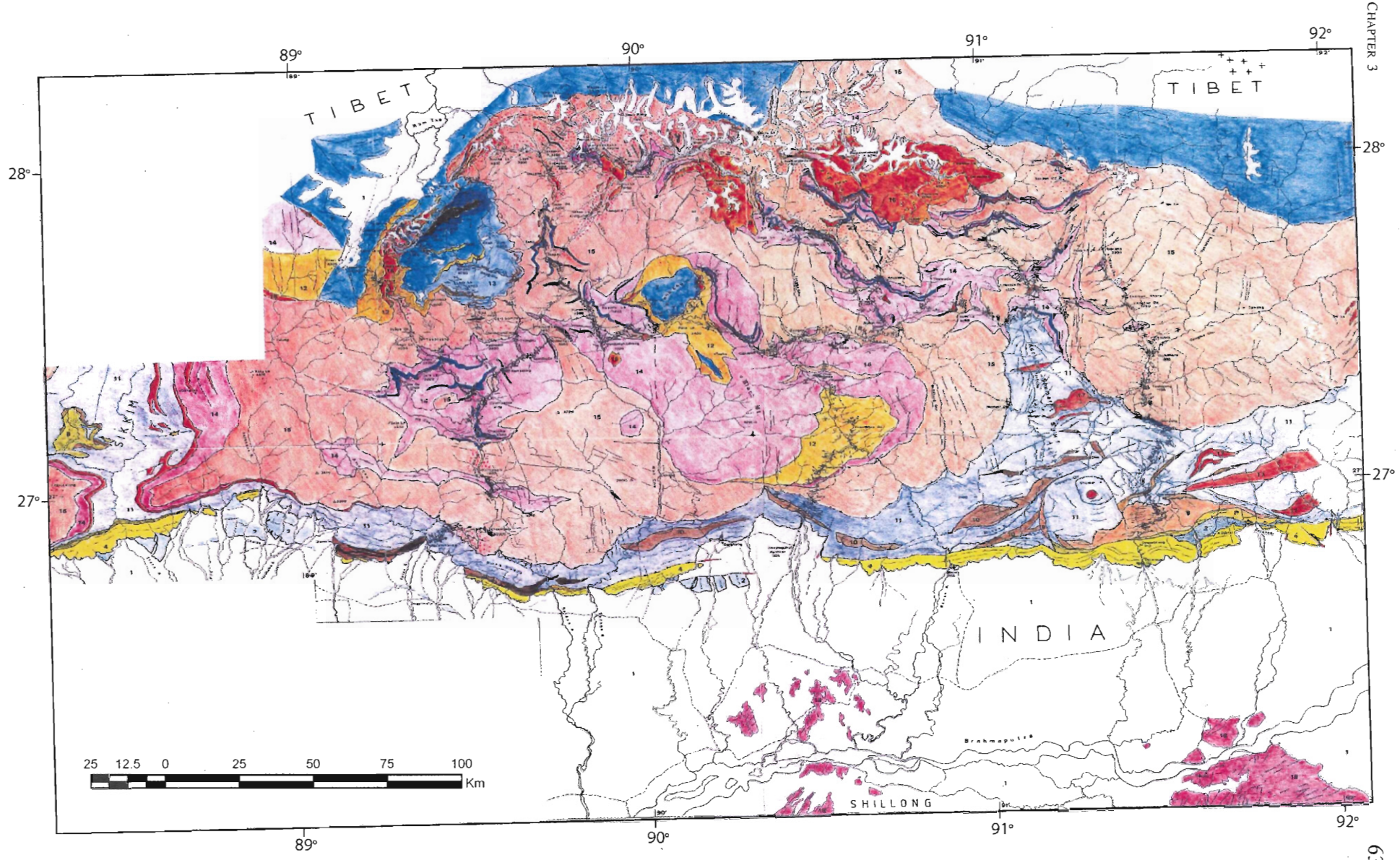


Figure 3.2: The geo-referenced version of Gansser's Map (1983). Projected in the geographic coordinate system with the datum as the World Geodetic System of 1984 (GCS-WGS-1984). For legend, see Figure 1.7.

3.2.2 Organisation of Data

All of the observations were divided into the respective components (structural, sample, and station data), given geographic locations, and then compiled into four separate databases within Microsoft Access. From this format, the data were then imported into ArcGIS, and projected onto Gansser's basemap using Lat/Long coordinates (Figures 3.3-3.6). Coordinates were determined either from GPS measurements at the station, or deduced from map data (also *GoogleEarthTM*) where GPS measurements were not available. The structural data were further subdivided into linear and planar data, and plotted according to trend /plunge or dip direction / dip respectively. Each type of structure was given a different symbol, which can be plotted together or separately in order to distinguish any patterns that may be present. A detailed structural analysis was performed for the Lingshi Syncline using the data, the details of which will be discussed in Chapter 4. The data collected for the whole of Bhutan span 1657 stations and include 2109 structural measurements (Figures 3.3, 3.5, & 3.6; Grujic et al., 1996 - 2007). Data from 833 rock samples were gathered and various analyses were performed on some of the samples according to the statistics presented in Table 3.1 (Figure 3.4). For the Lingshi syncline, the data include 499 stations, 332 samples, and 1083 structural measurements.

Table 3.1: Numbers of rock samples analysed by each of the various methods.

Type of Analysis	# of Samples Analysed
1) Lithology	89
2) Kinematics / Structural	60
3) Thin Section	210
4) Large Thin Section	7
5) Thermobarometry / Electron Microprobe	68
6) U-Pb dating	17
7) Ar/Ar dating (Muscovite)	13
8) Fission Track	95
9) Sm/Nd (provenance)	16
10) Detrital Zircon U-Pb (Provenance)	7
11) Raman Spectroscopy	43

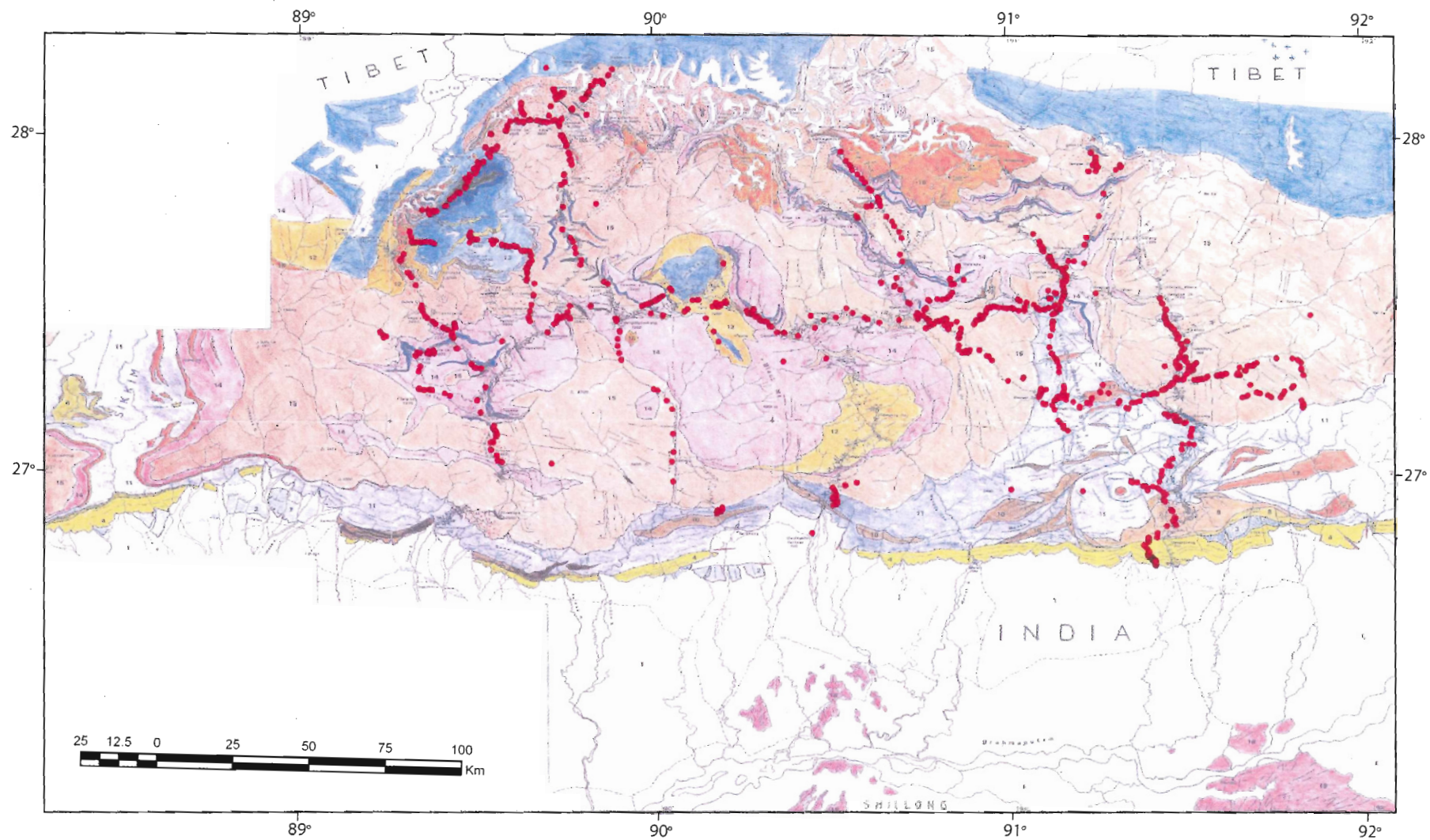


Figure 3.3: Geological map of Bhutan indicating the locations of stations in blue, from which data were collected.

Projected in: GCS-WGS-1984. (After Gansser, 1983)

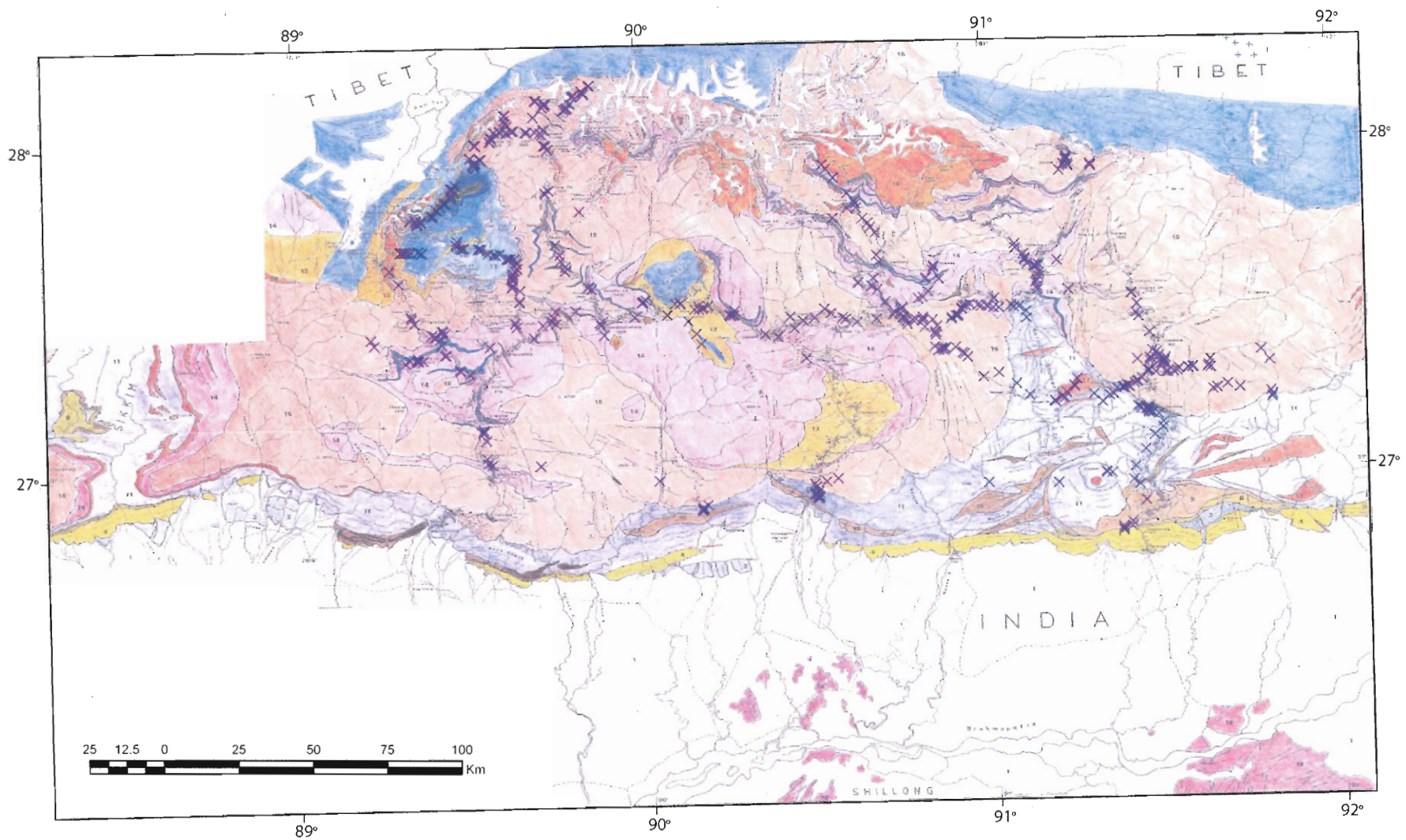


Figure 3.4: Locations of the samples collected from various outcrops.
Projected in: GCS-WGS-1984. (After Gannser, 1983)

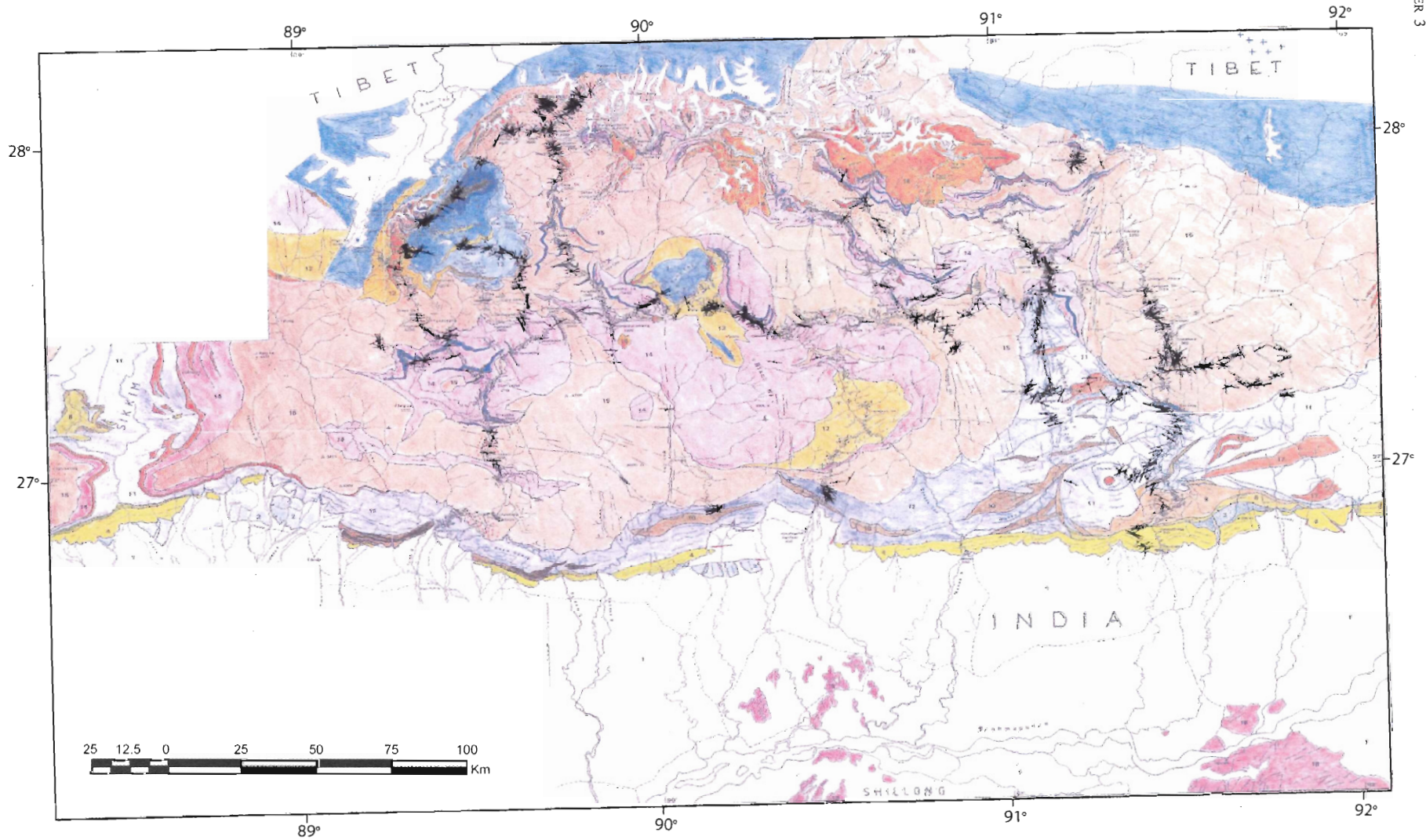


Figure 3.5: Locations of planar measurements taken from outcrops in Bhutan.
Projected in: GCS-WGS-1984. (After Gansser, 1983)

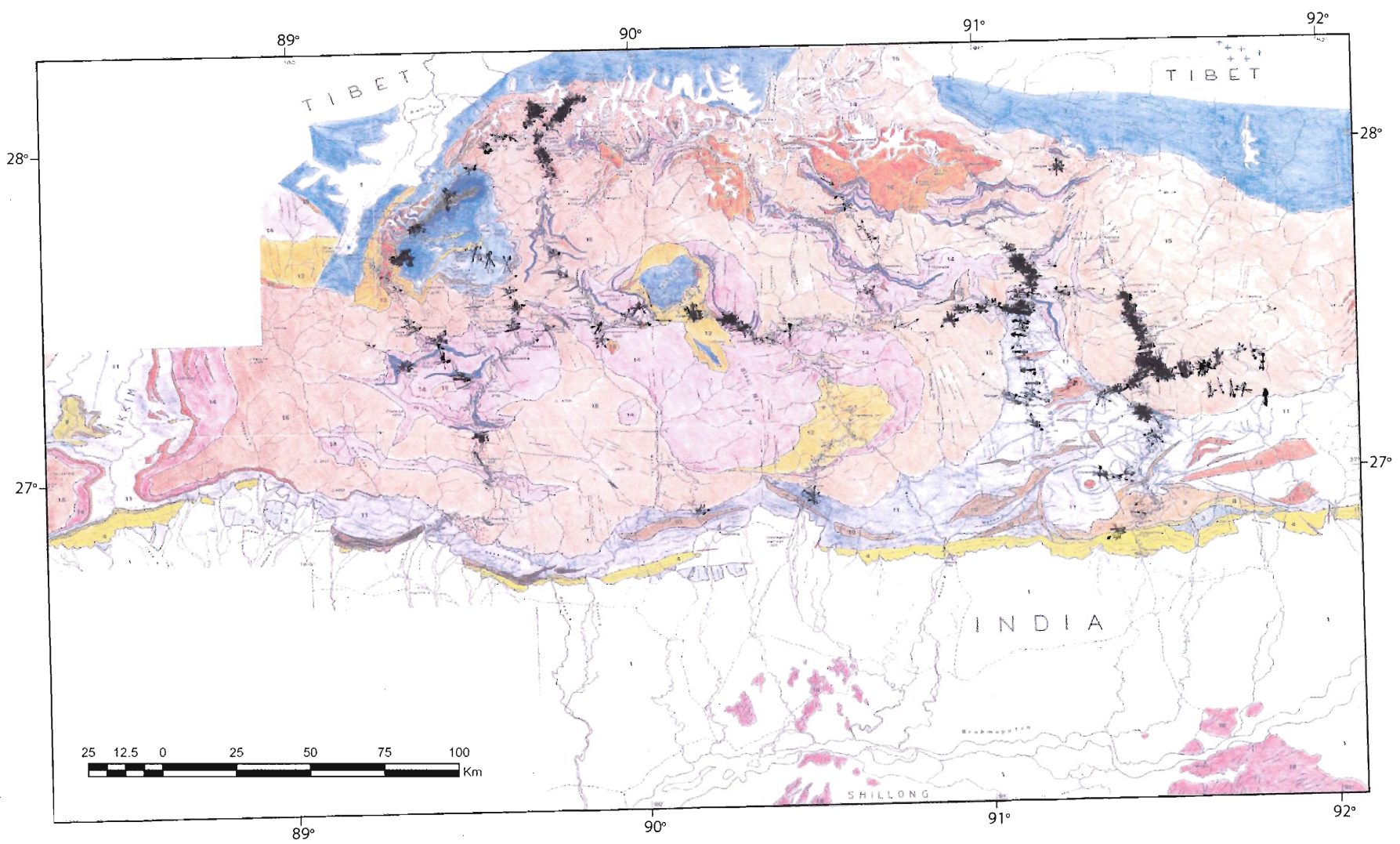


Figure 3.6: Locations of linear measurements taken from outcrops in Bhutan. Projected in: GCS-WGS-1984. (After Gansser, 1983)

The data gathered for the Lingshi Klippe and surroundings were gathered along traverses performed in Sept-Oct 1999, Oct 1996, May-June 2002, Sept-Oct 2002, Oct-Nov 2004, and Oct 2006, through four different valleys (Figure 3.7). The lithological information collected is connected to the ASTER images to determine the colour combinations which match each lithology. Using ArcMAP, polygons for each of the units are drawn to refine the important contacts of the region.

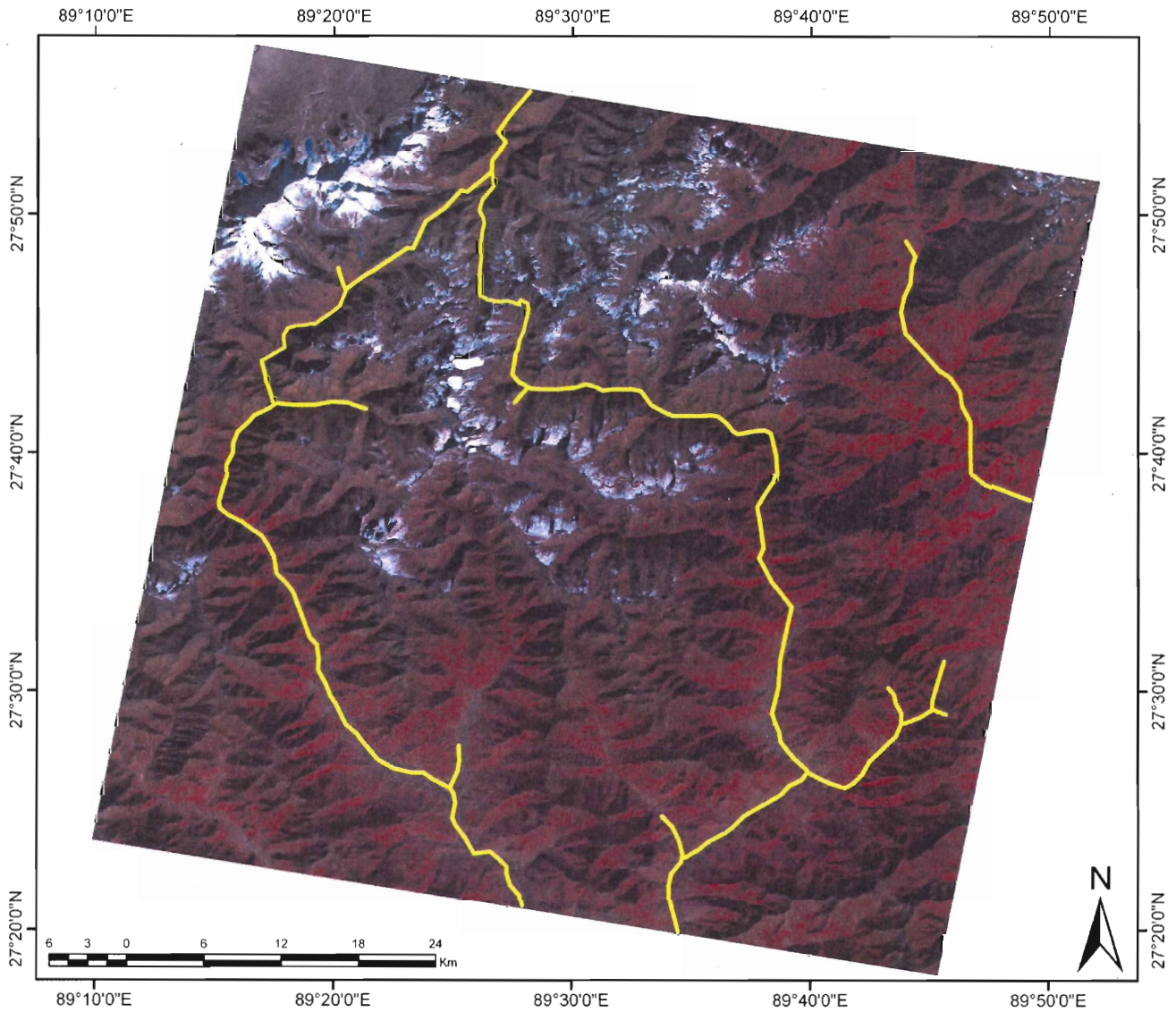


Figure 3.7: Image of a false colour composite created from ASTER Bands 1-3, showing the traverses that were performed throughout the syncline in yellow. Projected in: GCS-WGS-1984. (Exported from ArcMAP)

CHAPTER 4

4.0 STRUCTURAL ANALYSIS OF LINGSHI KLIPPE

The TSS and Chekha formation crop out in a series of erosional remnants (klippen) throughout the Bhutan Himalaya. The largest of these is the Lingshi Klippe. This is also one of only two such klippen that contain both sequences. The klippe is also known as the Lingshi Syncline, because the sedimentary units lie within the core of a large, irregular, synform (Gansser, 1983; Grujic et al., 2002). However, the exact fold geometry of this synform has not yet been investigated. Gansser (1983) was able to map the large Lingshi syncline and the matching anticline to the north and west, but did not perform any detailed structural analyses. One of the aims of this study is therefore to construct the orientation of the statistical fold axes and axial planes, using a large set of field measurements. In this thesis, the area was subdivided into structurally homogenous areas within individual tectono-stratigraphic units using a trial-and-error method (e.g. Ramsay & Huber, 1987). The main foliation (Sf) and sedimentary bedding (Ss) (where present) is analysed first. Second, the fold axes obtained from these analyses are compared to the field measurements of the related linear and planar structures (various lineations, axial planar cleavage, shear bands, etc). Finally, the regional trend of axial planes was constructed based on the trends of axial planes, fold axes, and lithological distribution.

The main foliation is the pervasive planar fabric in the study area. It is most likely the result of a complex, intensive folding and shearing history which has deformed all of the litho-tectonic units (Gansser, 1983; Grujic et al., 1996; Hodges, 2000) However, at the upper structural levels, primarily the TSS, the deformation intensity has decreased to an extent where original sedimentary bedding can still be observed. In the intermediate level, the Chekha, the Ss and Sf (primarily axial planar cleavage) are often difficult to distinguish in the field. Although

the orientations coincide in some areas, the two surfaces are not parallel (D. Grujic & D. Kellett, personal communications, 2007-2008). Several zones are also present where younger deformation can be observed, in the form of a second tectonic foliation (Sf2) and shear bands (Ssb).

4.1 CATEGORIZATION OF DATA

In order to perform the study, data were extracted from the created GIS database (Chapter 3) for the region of $89^{\circ} 7' E - 89^{\circ} 49' E$ and $27^{\circ} 24' N - 28^{\circ} 19' N$ (Figure 4.1). The data include a variety of planar and linear measurements acquired from field work (Table 4.1).

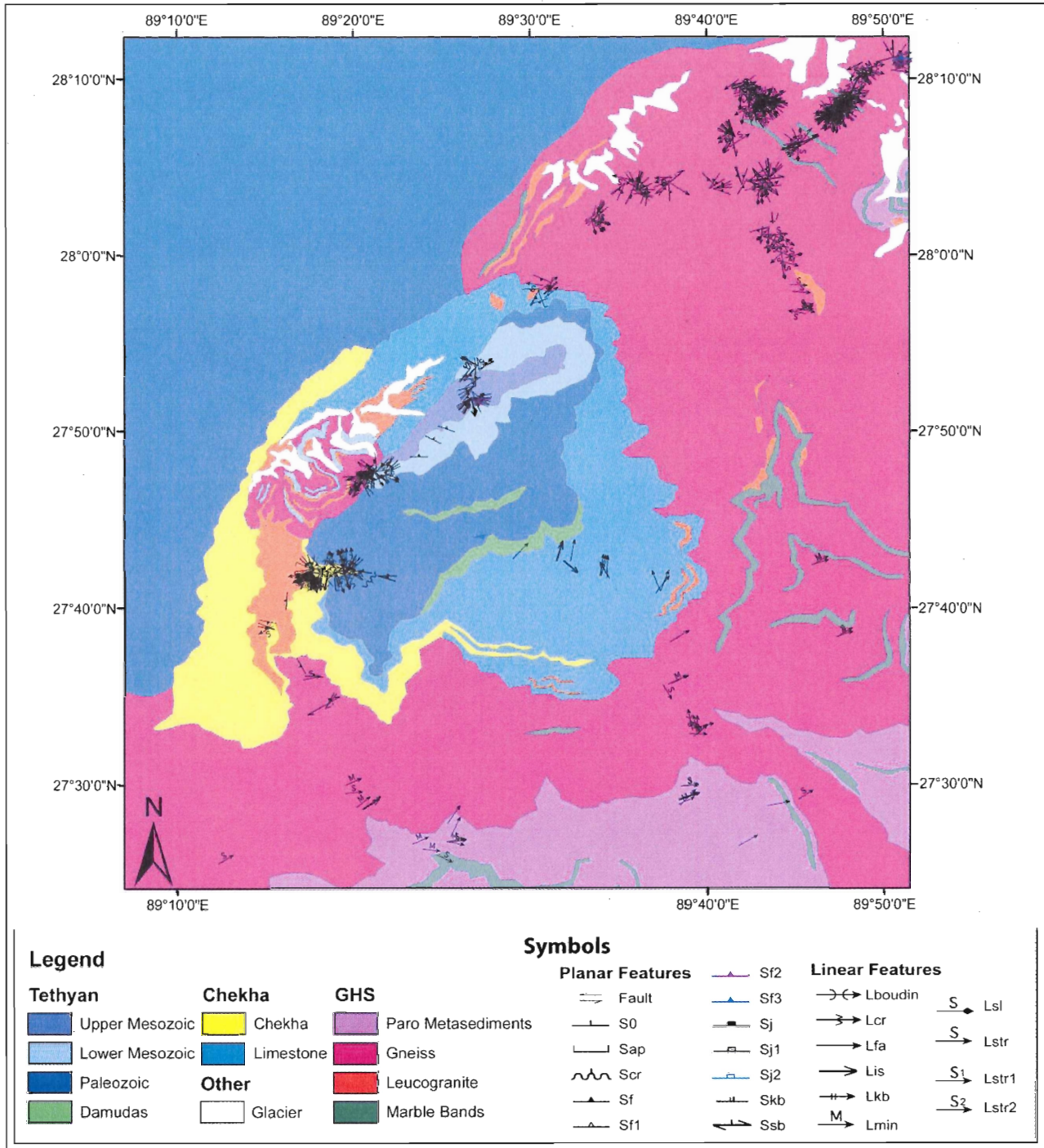



Figure 4.1: Map of the locations, extent and types of structural data extracted for analysis. The abundance and variation of data obviously make such a map difficult to interpret at this level, thus the data were divided into zones (Figure 4.2) and plotted on stereonet to find the trends (Figure 4.3).

Table 4.1: Table of the various types of structural measurements taken during field work (Performed by D. Grujic & coworkers from 1996 – 2006)

Lineations	Planes
Fold Axis = Lap	Main Foliation = Sf
Crenulation Lineation = Lcr	Sedimentary Bedding = Ss
Kind Band Lineation = Lkb	Tectonic Foliation = Sf1 / Sf2 etc...
Intersections = Lis	1 st Foliation (without any apparent genetic associations) = S0
Mineral Lineation = Lmin	Axial Planes = Sap
Slickenlines or Slickenfibres = Lsl	Crenulation Cleavage = Scr
Stretching Lineation = Lstr	Shear Bands = Ssb
Boudinage = Lboudin	Kink Bands = Skb
	Fracture Set or Joints = Sj / Sj1 / Sj2
	Faults
	Shear Planes = Sp

The measurements were differentiated by type and divided into groups based on lithological units. The groups were then broken up into locally homogeneous areas (smaller zones with a consistent deformational pattern), in order to differentiate the changes in structural trends throughout the region (Figure 4.2 & Table 4.2). To accomplish this, the measurements must necessarily be averaged over each area. The measurements from each area are analysed using the program SpheriStat to find the average trends for that region. Each area was analysed separately according to type of measurement and lithology.

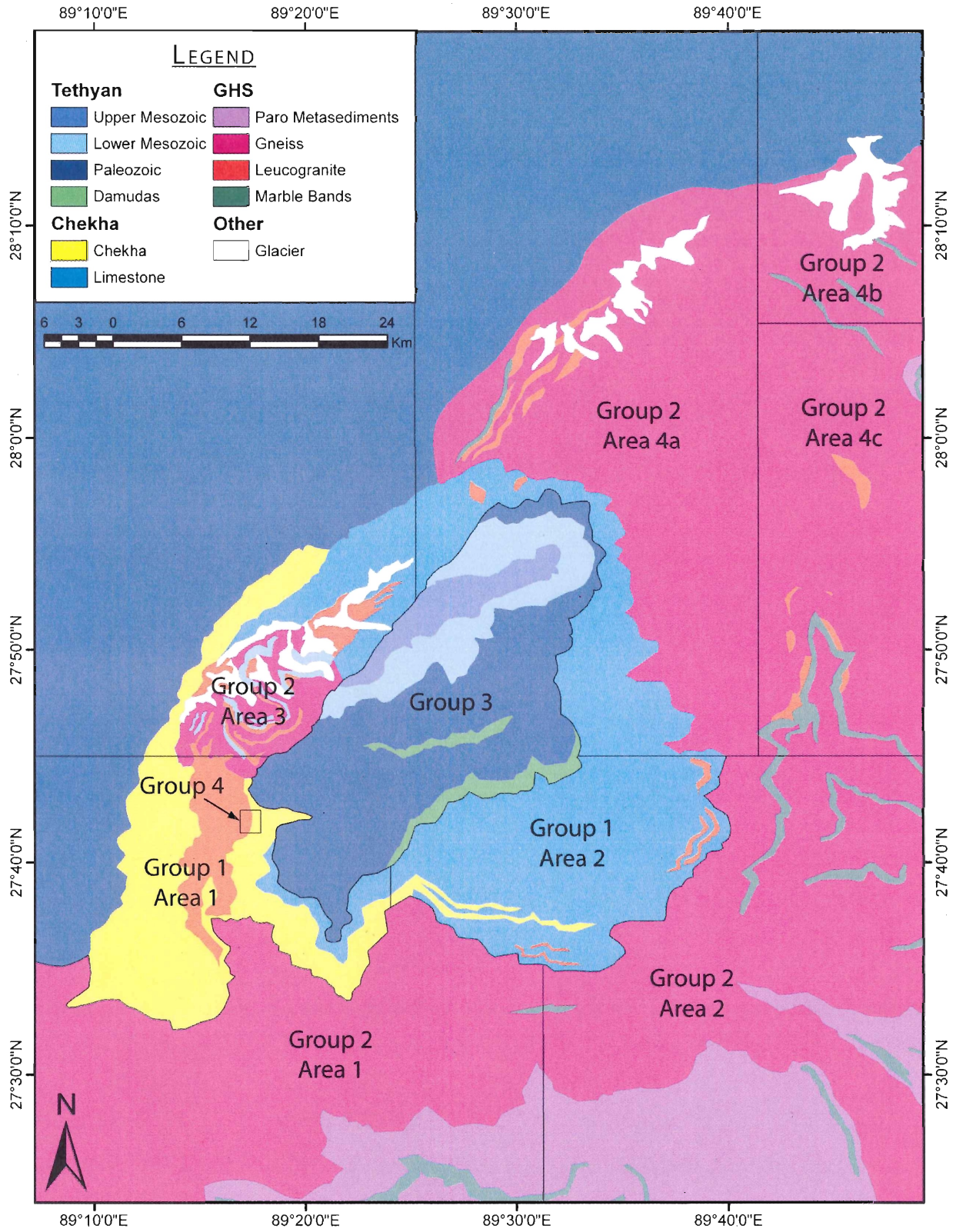


Figure 4.2: Map showing the structurally homogeneous zones into which the study area was separated

Table 4.2: Division of the lithological units into structurally homogeneous groups and any further subdivisions of those groups into areas indicated in brackets (See Figure 4.2 for the location of each of the areas).

Group #	Lithological Units Included (Including Gansser Unit #'s)
<i>Group 1</i> (Areas 1 & 2)	Limestone-Chekha; Chekha (Units 12 & 13)
<i>Group 2</i> (Areas 1 – 4)	Gneiss/Migmatites; Leucogranites; Paro Metasediments; Marble Bands (Units 14,15 & 16)
<i>Group 3</i>	Tethyan-Upper Mesozoic; Tethyan-Lower Mesozoic; Tethyan-Paleozoic, Damudas (Units 5, 6, 7 & 8)
<i>Group 4</i>	Boundary between the leucogranite intrusion & the Chekha Formation in the western area

4.2 DENSITY CONTOURING AND STATISTICAL ANALYSIS

The data were then imported into SpheriStat™ 2 (Pangaea Scientific Software), and plotted on stereonet as great circles or poles. SpheriStat can be used for entering large numbers of structural field measurements in a tabular form, to be utilised in a variety of ways, including plotting on a stereonet (Schmidt equal area or Wulff equal angle), map, or a circular (rose diagram). Information on the data can be extracted in several ways using the analytical tools available with each plotting method. For this analysis, the Sf data are contoured using the Gaussian E-sigma technique with a fine grid density. In the Gaussian counting technique, all the data points are counted using a function of their distance from the counting station. Points that are farther away are not weighted as heavily. Thus, this method gives a smoother contour line than other methods (Stesky, 1996). The contour diagram is assembled so that there are seven density contours, the optimal number of contours for a stereonet plot, arranged at equal interval between 1 and the maximum value of the net. From the contours, the spread and density of data can be determined. The three-dimensional treatment of data is based on eigenvector analysis (i.e. Bingham statistics) to determine the average trend and plunge of the statistical fold axis as

defined by the distribution of Sf and/or Ss orientations (Cheeny, 1983). Bingham statistics determines three mutually perpendicular eigenvectors t_1 , t_2 , and t_3 along with the corresponding eigenvalues τ_1 , τ_2 , and τ_3 . The three eigenvectors estimate the directions of principal axes of symmetry for the parent population. The associated eigenvalues (τ) are proportional to the point density in that direction (Cheeny, 1983). In the case of folded planar structures, two eigenvalues are located along the best-fitting great circle through the data (plotted as poles to the plane) and the third, corresponding to the statistical fold axis, is the pole to the great circle.

4.3 RESULTS

The structural analyses illustrate a complex folding pattern for the Lingshi Syncline. The Sf and Ss display a regional antiform / synform pair with changes in the trend of the fold axis (Table 4.3). The stereonet analyses used to find these trends follow (Figures 4.5-4.35), as well as a summary discussion of the main features observed. All of the stereonets shown (Figures 4.5 – 4.35) are produced in SpheriStat using the Schmidt, equal area, lower hemisphere projection, from data acquired by D. Grujic & co-workers between 1996 and 2006.

Table 4.3: Results from Eigenvector and Gaussian counting analysis for Sf and Ss measurements for each structurally homogenous area. The resulting trend/plunge is the statistical fold axis for each area analysed. n = number of field data points, Max value = the maximum value in the density distribution, greyed-out areas = no measurements available for that region.

MAIN FOLIATION										
Units	Group 2: GHS						Group 1: Chekha			Group 3: Tethyan
	Area 1	Area 2	Area 3	Area 4			Area 1	Area 2	Grp 4	
				A	B	C				
n	42	58	18	48	73	39		48	41	67
Max Value	25.19	17.33	12.18	14.47	10.78	8.46		14.43	14.57	10.20
Trend/Plunge of Fold Axis	326/19	334/15	095/13	224/00	080/07	080/01		272/13	150.0 9	066/11
BEDDING										
n							29		9	
Max Value							15.11		8.41	
Trend/Plunge of Fold Axis							270/17		078/00	

The Lingshi syncline is somewhat bowl-shaped (i.e.: it is a structural basin), as is evidenced by the distribution of the foliation and bedding orientations (Figure 4.1), lithological outlines (Figure 4.1), and variation in the trend and plunge of fold axis for each area (Figure 4.3). In the south, the syncline appears to be plunging to the northeast. To the north, the anticline pair to the syncline is obscured somewhat in the high mountains, however in the NE region of the GHS, the fold can be mapped in the field (e.g. Chakungal, 2006). Here, the anticline curves around into an east-west trend (Figures 4.3, 4.15, 4.18, 4.36). The planar features (Sf, crenulation cleavage (Scr) and axial planes (Sap)) appear to have been formed in the same tectonic event as these major folds, as they follow the same trend (Figures 4.5 4.6, 4.8, 4.9, 4.11, 4.13, 4.15, 4.16, 4.18, 4.20, 4.21, 4.44, 4.24, 4.25, 4.26, 4.28, & 4.20). Field measurements of axial planes of outcrop-scale open folds are consistent with the orientation of the first-order folds (Figures 4.6, 4.9, 4.16, 4.21, & 4.25). Similarly, the crenulation cleavage measured in the field may be related to this late folding event (Figures 4.22 & 4.26). Conversely, the lineations

present regionally are not parallel to the mean fold axis (Figures 4.7, 4.10, 4.12, 4.14, 4.17, 4.19, 4.23, 4.27 & 4.30).

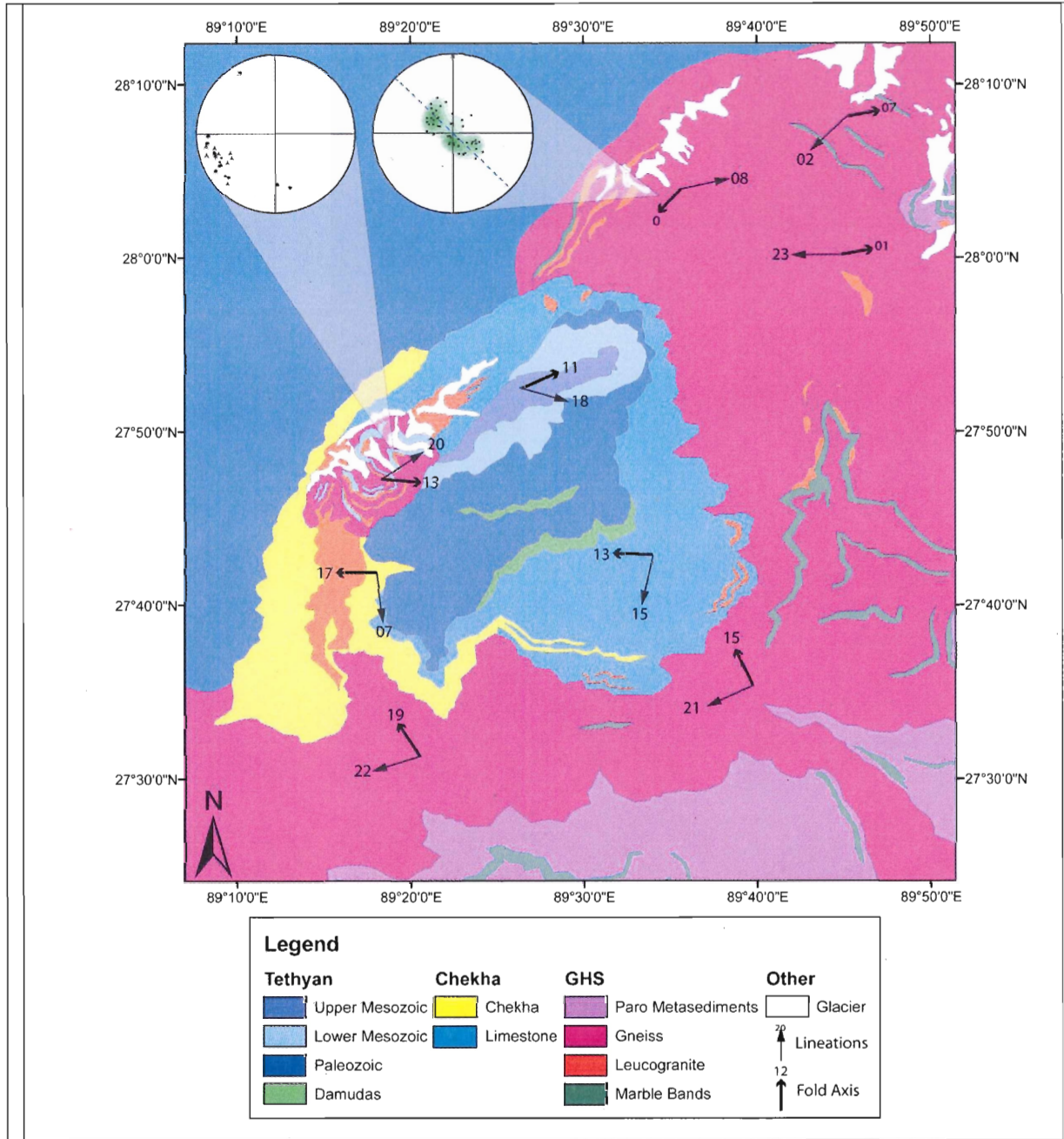


Figure 4.3: Map of the statistical fold axes and trends of measured lineations plotted for each area analysed and an example of each stereonet plot used to find these trends. The stereonets are shown in Figures 4.4 – 4.35.

However, their trends also vary along with the regional fold. Thus, it was interpreted that the formation of these lineations is likely related to a deformation stage preceding the formations of these folds. Most likely, the mineral and stretching lineations are related to the formation of the Sf in the area. Since there is no observed axial planar cleavage related to the large, open folds, it is probable that the most of the intersection lineations are also connected to the formation of the Sf. In the TSS, however, it is difficult to determine the temporal and thus kinematic relationship between the cleavage in the sediments and the foliation in the GHS rocks. The lineations were subsequently folded during the event that produced the Lingshi synform (the deformation stage analysed by this study).

The Lingshi Syncline is a very gentle, open, upright and highly non-cylindrical structure. Thus, it can actually be quite difficult to map the fold hinge regionally; it is only possible to map local variations in the structure. Since the fold is so irregular, the trends in fold axes vary quite substantially over the study area. This may be due to the presence of a major fault, the Lingshi fault, along the northern boundary of the TSS (Figure 4.36). The fault is a very steeply dipping fault with a vertical component (E block down), in addition to a strike-slip, sinistral shear sense (Drupka et al., 2006). Due to the shearing motion along the fault, the syncline may have been deformed locally, resulting in a non-cylindrical fold. In addition to the regional variations in the trend of the fold axes, there is also some discordance between the different structural levels. In the GHS, the southern areas display a consistent trend to the NW. However, in the northern areas, the fold axes trend to the east. In one area, where the axis is bending, the trend is to the southwest; however this may be an artefact of scatter in the data. In the Chekha Formation, both the eastern and western areas agree well, with a statistical fold axis trend to the west.

Conversely, the TSS exhibits a trend of both the Sf and Ss to the northeast/east. Thus, a different

folding style is observed at the various structural levels, in addition to the observed regional distinctions.

There are two places within the study area which deviate from the main observed regional trend. The first disparity is located in the NE-GHS (Group 2/Area 4b & c), where observations in the field combined with the statistical analysis, indicate the presence of a set of conjugate S_{sb} and a secondary tectonic foliation (Sf_2) (Chakungal, 2006). The first set of shear bands dips to the NW, with top-to-the-NW shear sense, and the second set dips to the south, with top-to-the-SE shear sense (field observations by J. Chakungal and D. Grujic). The NW-dipping S_{sb} are parallel to the Sf_2 , which also dip to the NW (Figure 4.34). The orientations are quite consistent and do not appear to be affected by the regional folding, thus they are likely younger or occurred at a later stage of the folding. The second zone is at the location of the contact between the leucogranites of the GHS and the Chekha formation (Group 4). Here, the structures are quite complex. The Sf orientations give a statistical fold axis to the SE, with S_{ap} trending to the SW (Figures 4.31 & 4.32). The lineations trend to the NE, and may be related to the S_{ap} orientations (Figures 4.32 & 4.33). However, the data have a large amount of scatter, probably influenced by the intrusion of leucogranite into the existing foliation, and/or by deformation along the Lingshi fault (Figure 4.36). The first zone is located near the upper STD, and the second zone is located at the lower STD. Since both zones are associated with the leucogranite intrusions at the top of the GHS, it is thought their formation is probably related to movement along the STD.

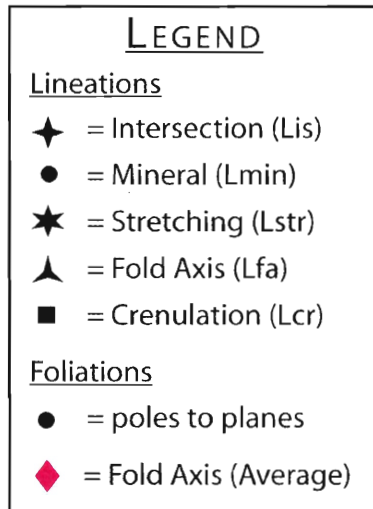


Figure 4.4: Legend for the following stereonet.

Group 2 / Area 1: Main Foliation

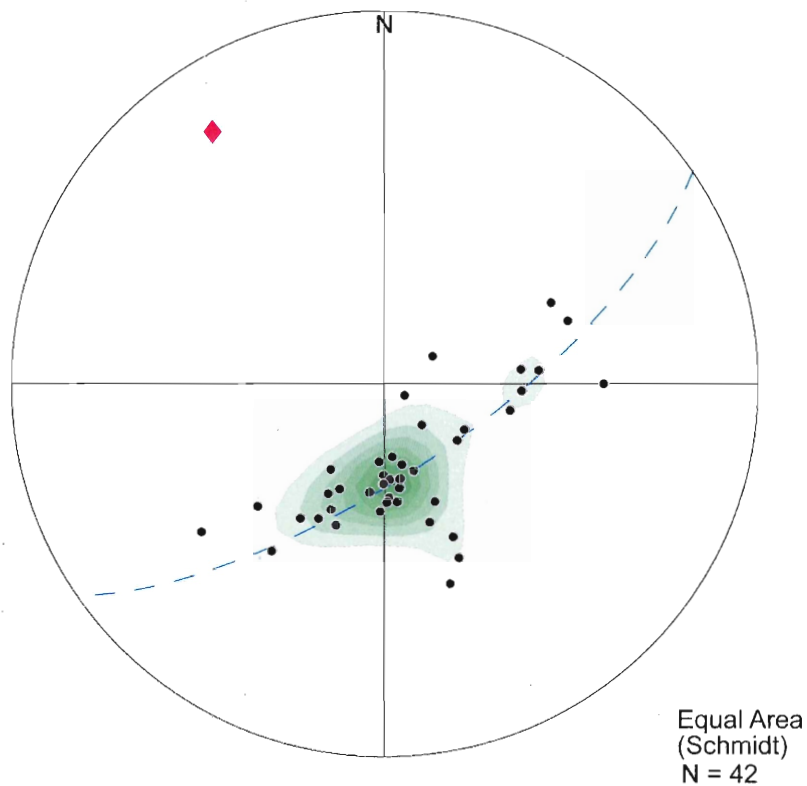


Figure 4.5: Sf measurements for the SW-GHS (Group 2/Area 1). Here, the fold trends NW. This is likely due to the fold being somewhat “bowl-shaped”; this unit is located on the SW rim of the syncline.

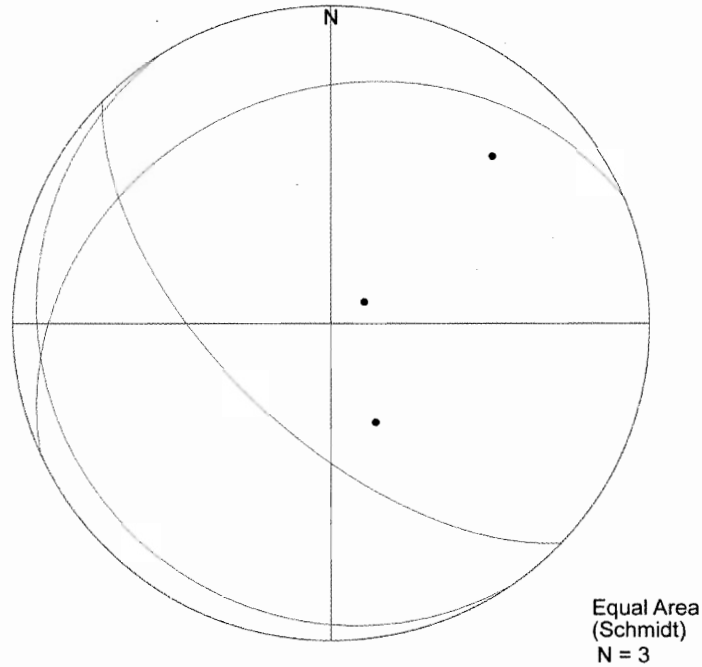
Group 2 / Area 1: Axial Planes

Figure 4.6: Sap for the SW-GHS (Group 2/Area 1). Orientations follow a similar trend to those described in Figure 4.5.

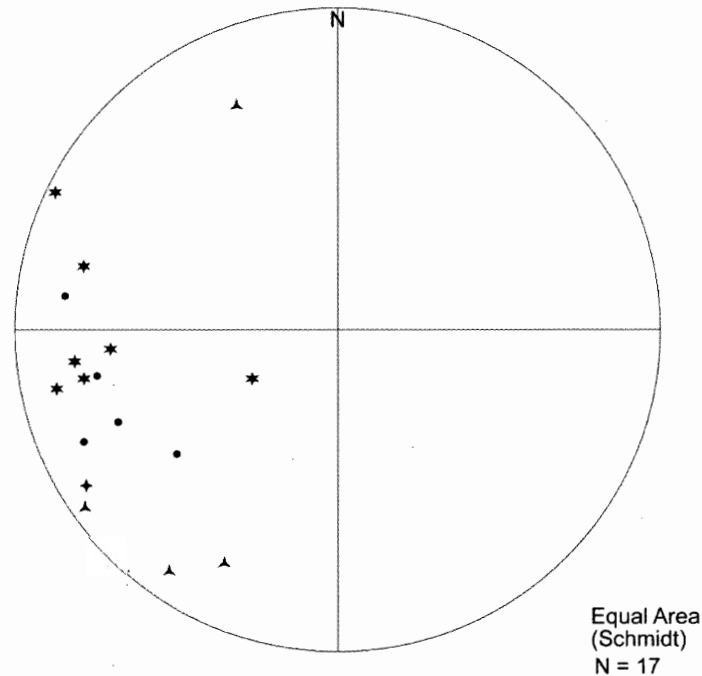
Group 2 / Area 1: Lineations

Figure 4.7: Lineations for the SW-GHS (Group 2/Area 1). Only a few follow the fold trend, the rest lie in the different orientation. Note that the trend of the lineations changes regionally. This is likely the result of the variations in the shape of the fold and the folding of this lineation.

Group 2 / Area 2: Main Foliation

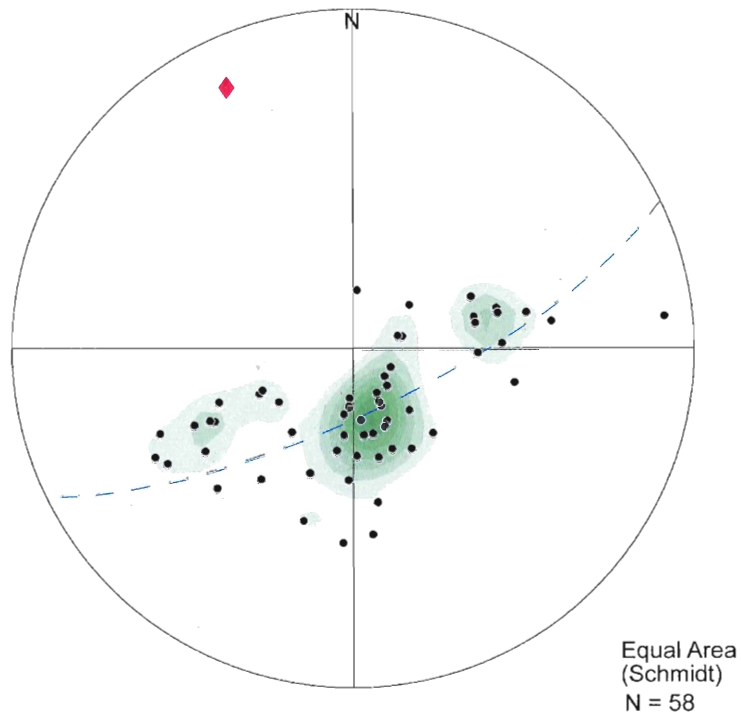


Figure 4.8: *S_f* for the SE-GHS (Group 2/Area 2). The trend is similar to that in the SW, shown in Figure 4.5.

Group 2 / Area 2: Axial Planes

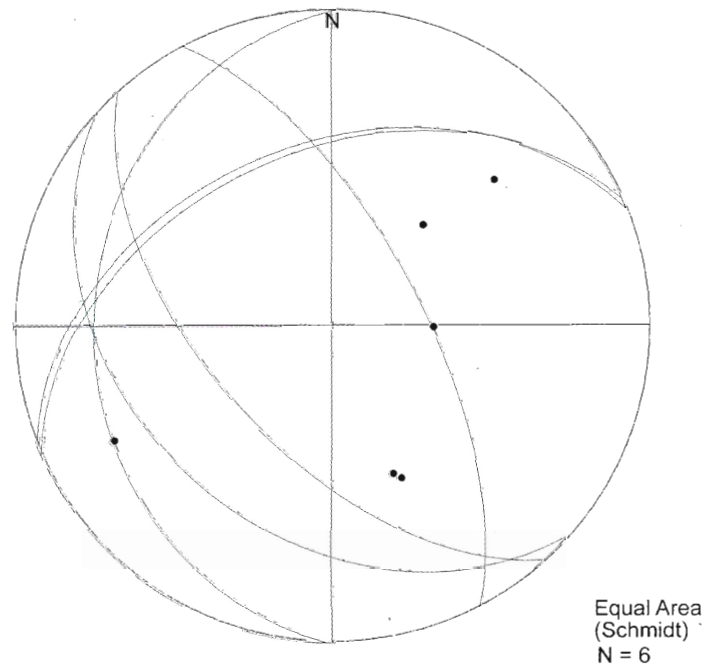


Figure 4.9: *S_{ap}* for the SE-GHS (Group 2/Area 2). There is a high scatter, and a specific trend cannot be noticed.

Group 2 / Area 2: Lineations

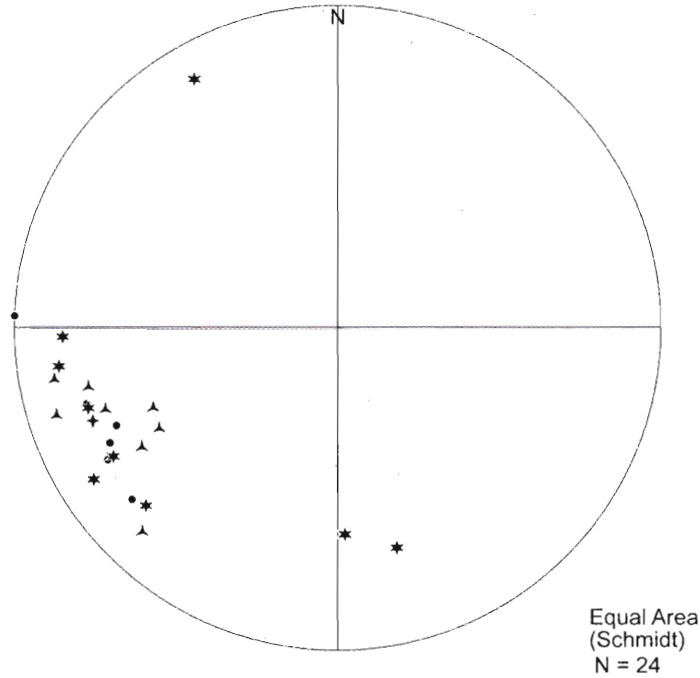


Figure 4.10: Lineations for the SE-GHS (Group 2/Area 2). These are similar to the lineations in the SW (Figure 4.7), following the same trend.

Group 2 / Area 3: Main Foliation

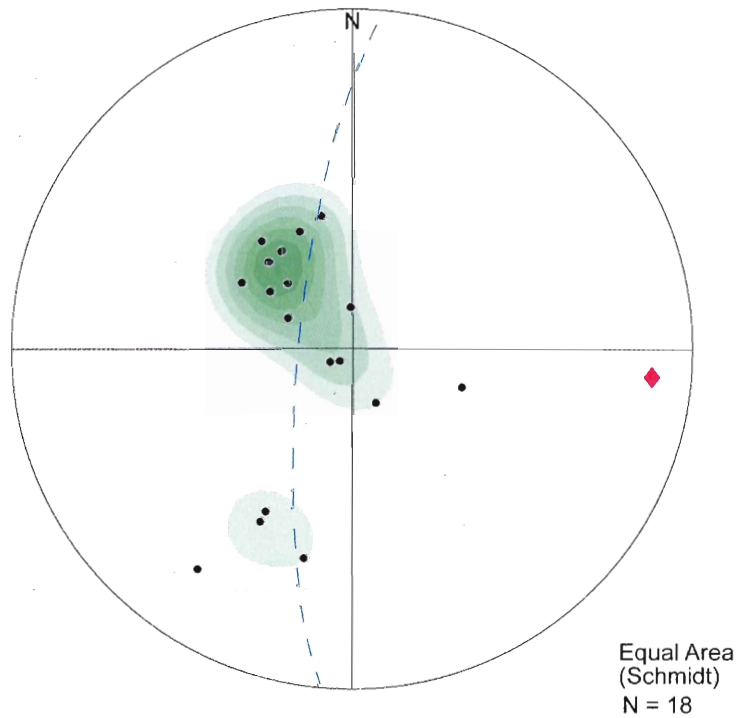


Figure 4.11: S_f for the NW-GHS (Group 2/Area 3). The trend is to the east. This area is on the NW side of the fold.

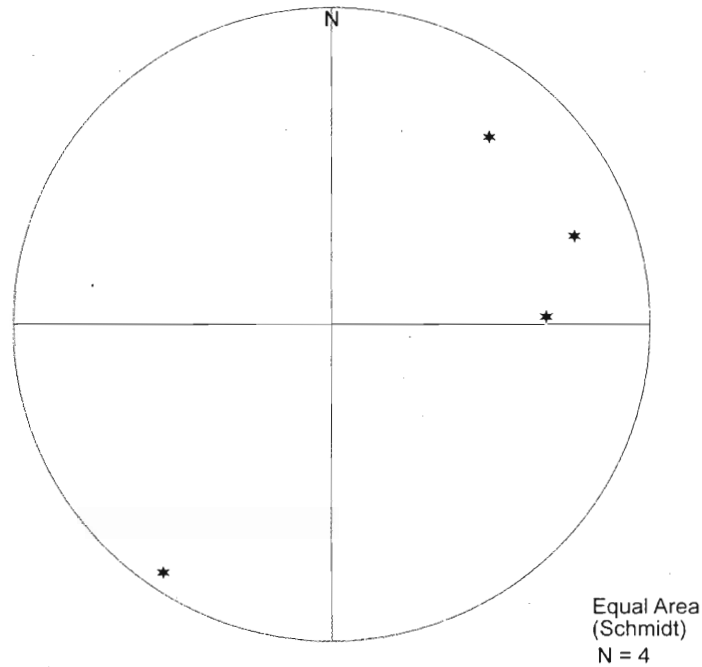
Group 2 / Area 3: Lineations

Figure 4.12: Lineations for the NW-GHS (Group 2/Area 3). There are only a few measurements from the area, but they still have a similar distribution as the lineations in other areas.

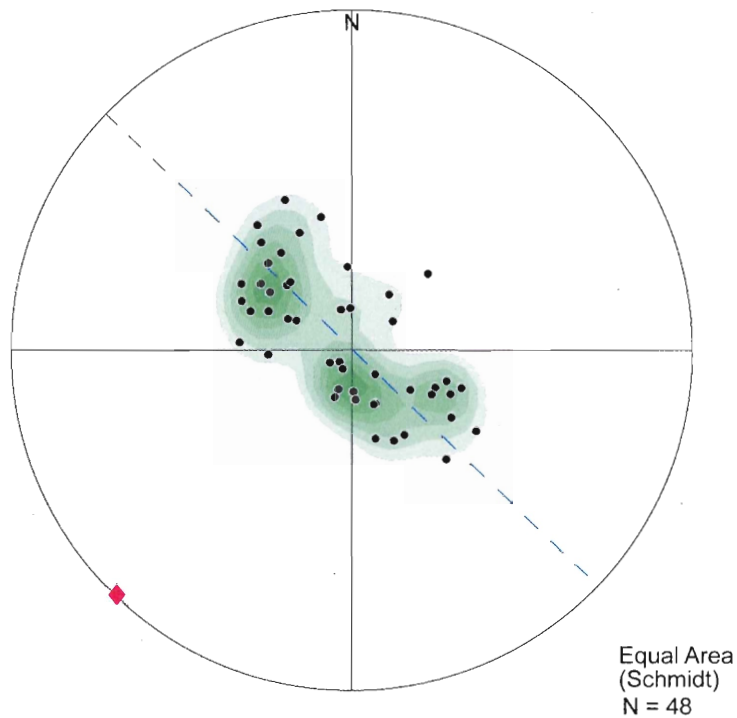
Group 2 / Area 4a: Main Foliation

Figure 4.13: Sf for the NE-GHS (Group 2/Area 4a). These measurements are taken on the NE side of the syncline. The trend of fold axis is to the SW.

Group 2 / Area 4a: Lineations

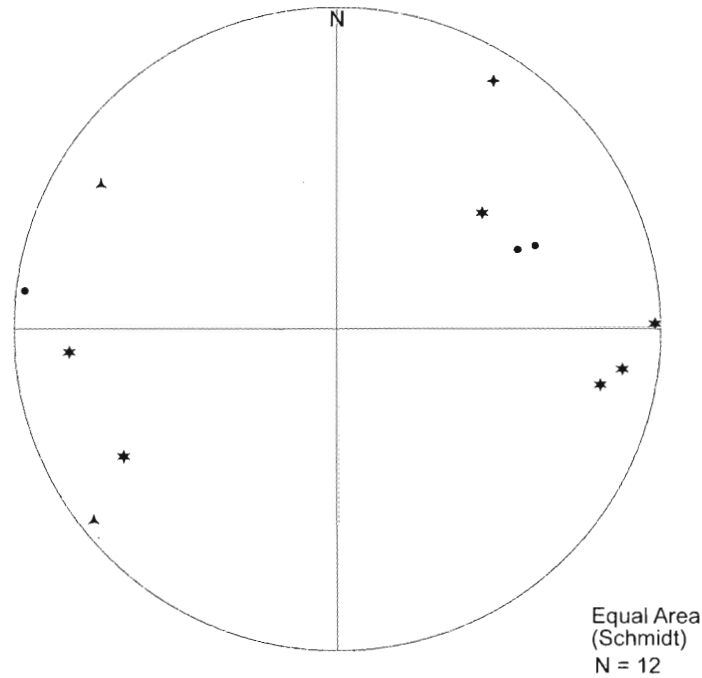


Figure 4.14: Lineations for the NE-GHS (Group 2/Area 4a). The lineations here are more parallel to the statistical fold axis than in the previous areas.

Group 2 / Area 4b: Main Foliation

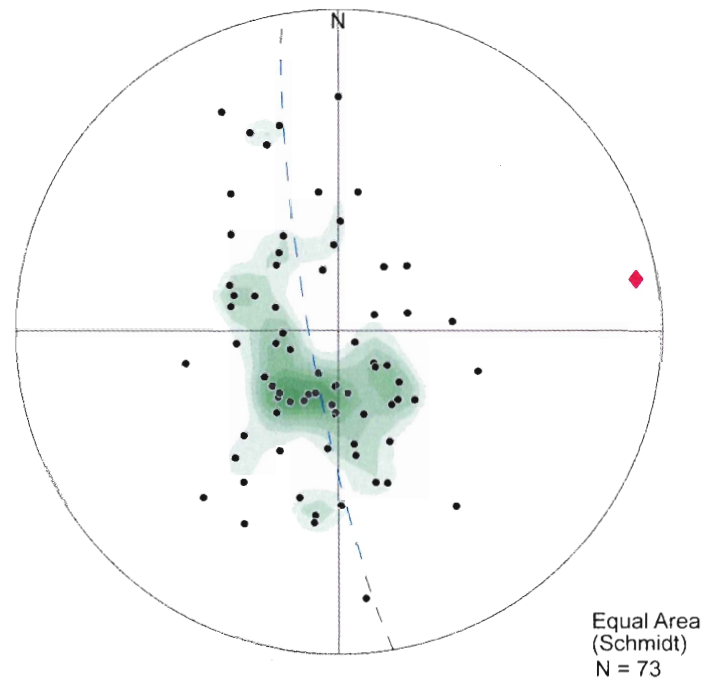


Figure 4.15: Sf for the NE-GH (Group 2/Area 4b). In this area the fold curves into an E-W trend. Thus, the data here are highly scattered, despite division of Area 4 into smaller sub-areas a-c. However, it can be seen that the fold axis has changed orientation to the NE / E.

Group 2 / Area 4b: Axial Planes

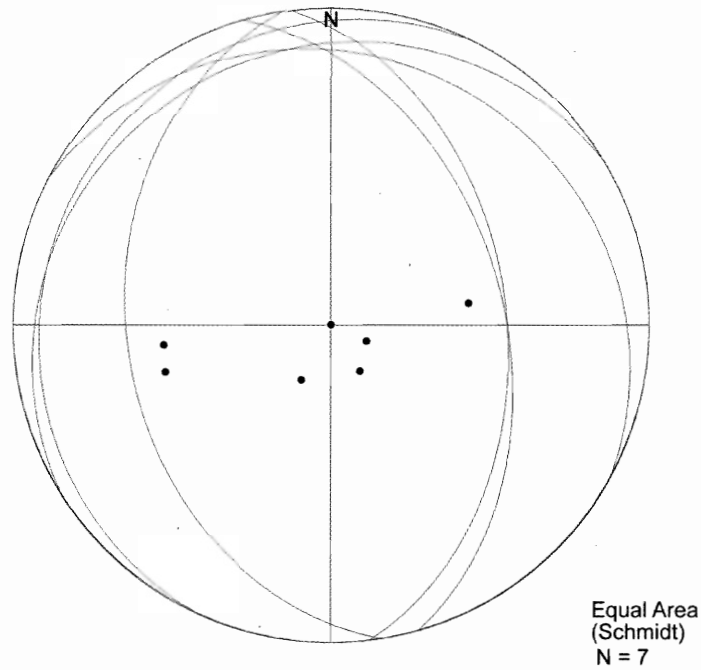


Figure 4.16: Sap for the NE-GHS (Group 2/Area 4b). The individual measurements have the same strike suggesting a fan-shaped distribution around a common, horizontal NNW-SSE trending fold axis. However, the measured fold axis in the area trends E-W (Figure 1.5).

Group 2 / Area 4b: Lineations

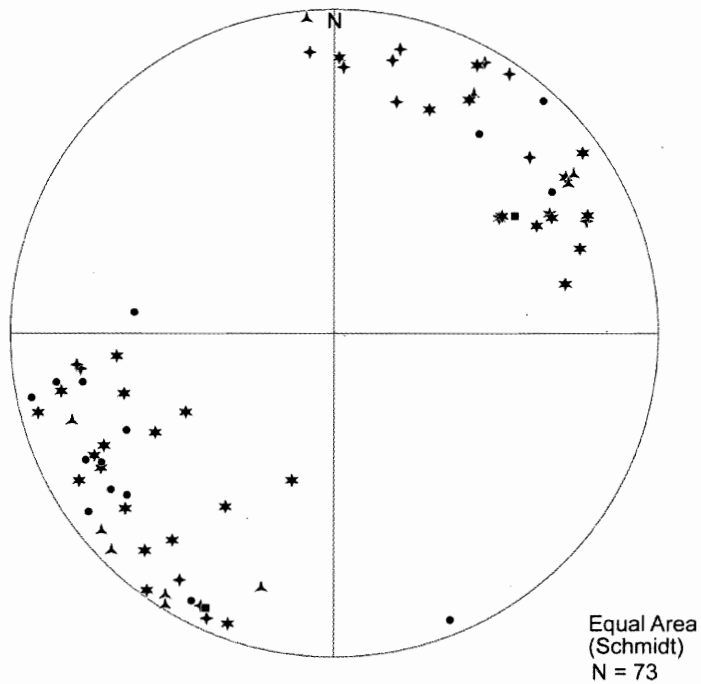


Figure 4.17: Lineations for the NE-GHS (Group 2/Area 4b). These are similar to the lineation attitude in other areas, however here they are starting to follow a trend more parallel to the statistical fold axis.

Group 2 / Area 4c: Main Foliation

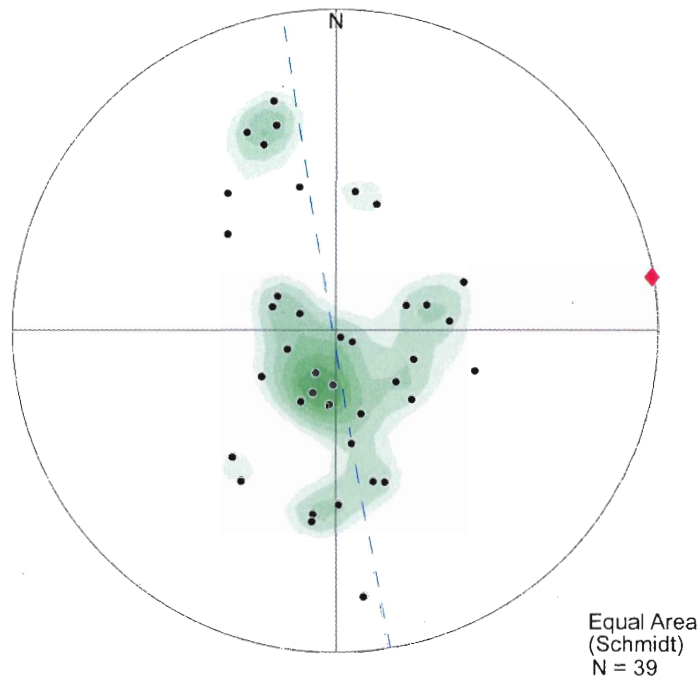


Figure 4.18: *Sf* for the NE-GHS (Group 2/Area 4c). The fold hinge trends to the E-W, as it was in Area 4b (Figure 4.15), but with less scatter in the data.

Group 2 / Area 4c: Lineations

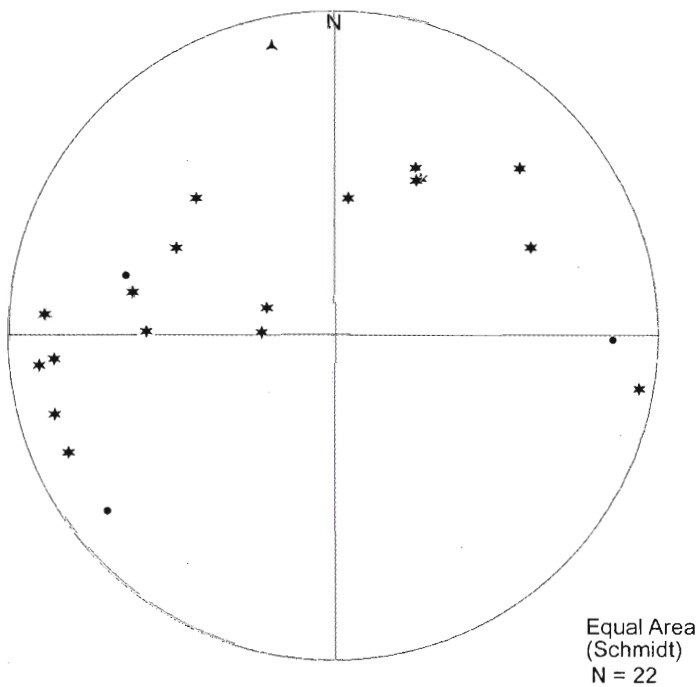


Figure 4.19: Lineations for the NE-GHS (Group 2/Area 4c). The lineations here show evidence of the curvature of the fold; they are distributed along a steeply dipping NW-dipping great circle whose SE dipping pole may be the axis of rotation of the entire area.

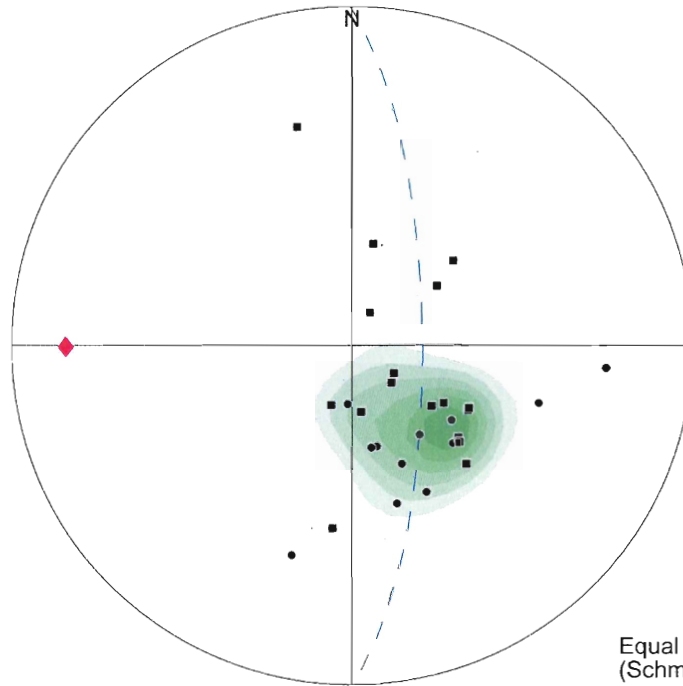
Group 1: Sedimentary Bedding

Figure 4.20: S_s for the entire Chekha formation (Group 1/Areas 1 + 2). In this case the orientation of the S_f of the western side was found to be correlative to the orientation of the S_s , so the measurements were combined for the whole formation.

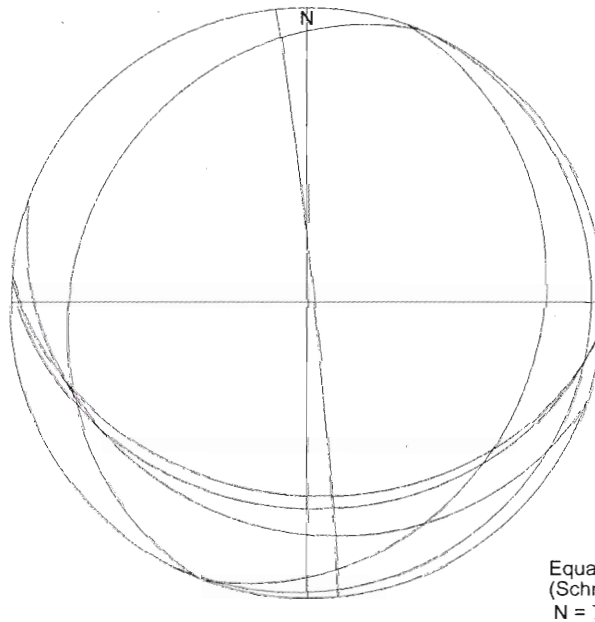
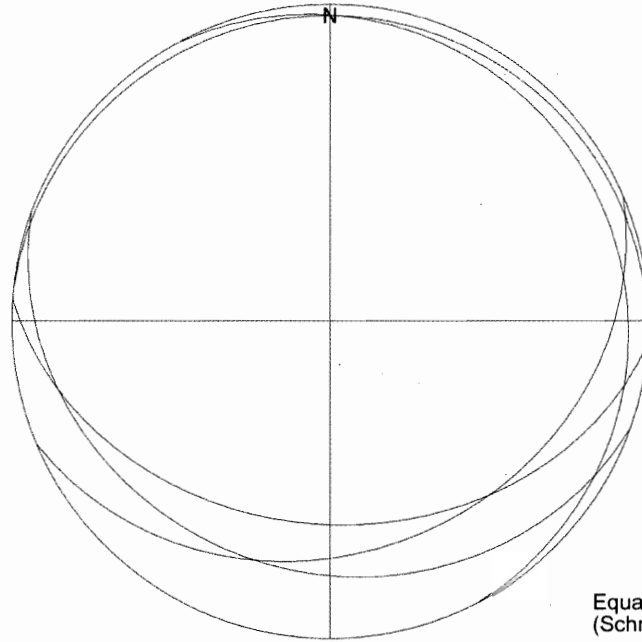
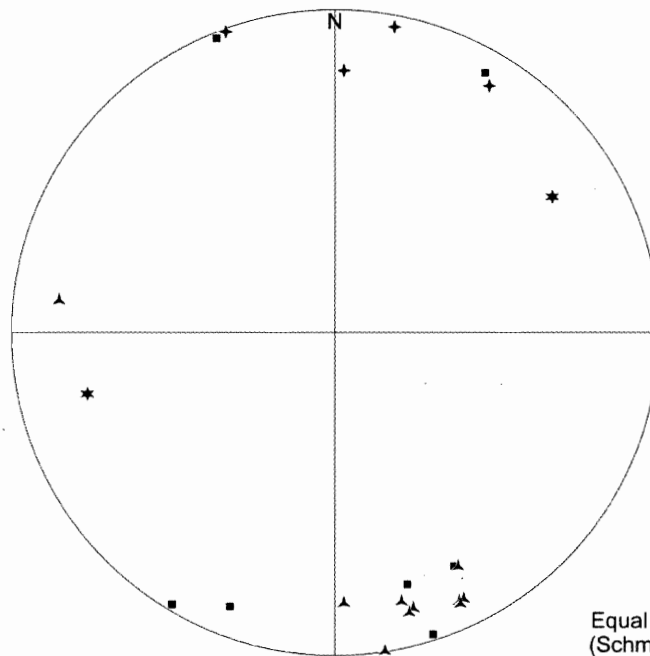
Group 1 / Area 1: Axial Planes

Figure 4.21: S_{ap} for the western portion of the Chekha Formation (Group 1/Area 1). Note that the trend is similar to that displayed by the S_s shown in Figure 4.20.

Group 1 / Area 1: Crenulation Cleavage

Equal Area
(Schmidt)
N = 5

Figure 4.22: *Scr* for the western portion of the Chekha formation (Group 1/Area 1).

Group 1 / Area 1: Lineations

Equal Area
(Schmidt)
N = 24

Figure 4.23: Lineations for the western portion of the Chekha Formation (Group 1/Area 1). Note that there are only a few lineations which correspond to the general trend of fold axis as shown in Figure 4.20. The rest follow a different orientation.

Group 1 / Area 2: Main Foliation

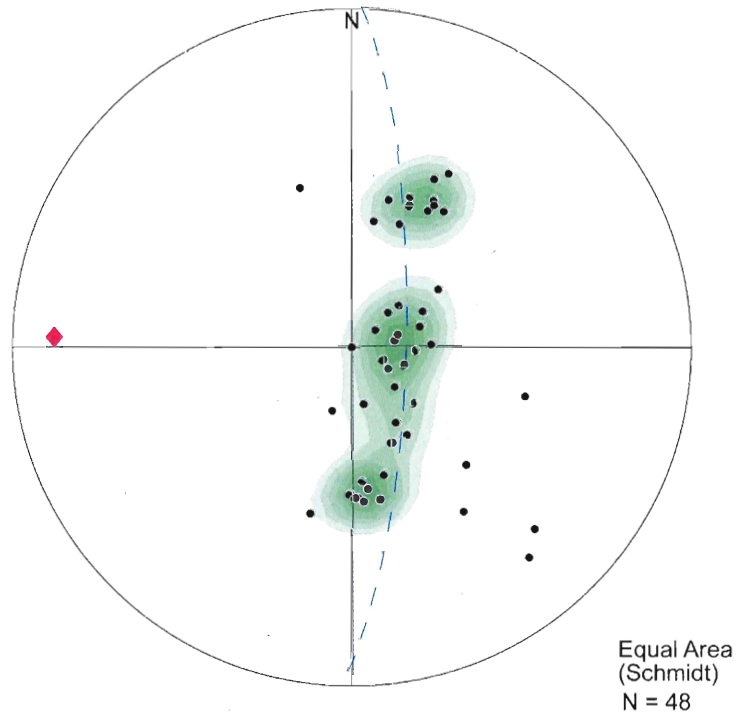


Figure 4.24: S_f for the eastern portion of the Chekha Formation (Group 1/Area 2). The fold axis follows the same trend as the S_s (Figure 4.20), demonstrating that the whole unit follows a similar trend.

Group 1 / Area 2: Axial Planes

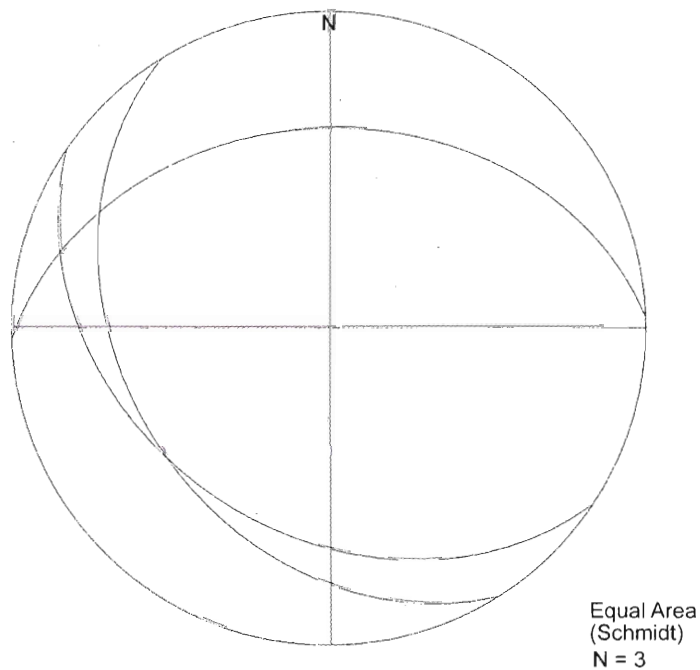


Figure 4.25: S_{ap} for the eastern portion of the Chekha Formation (Group 1/Area 2). Note that they follow the similar trend to that of the S_f (Figure 4.24).

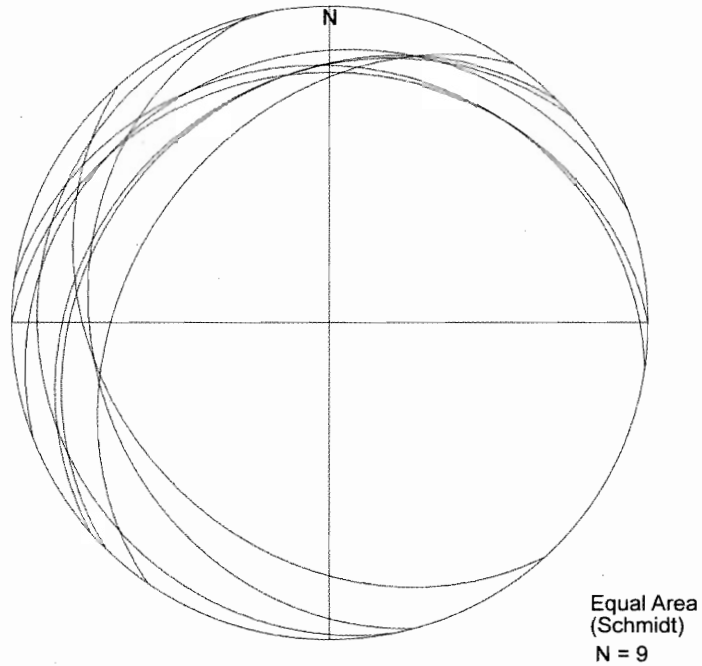
Group 1 / Area 2: Crenulation Cleavage

Figure 4.26: *Scr* for the eastern portion of the Chekha Formation (Group 1/Area 2). There is some scatter in the data, but in general it follows a similar trend to the fold axis (Figure 4.24).

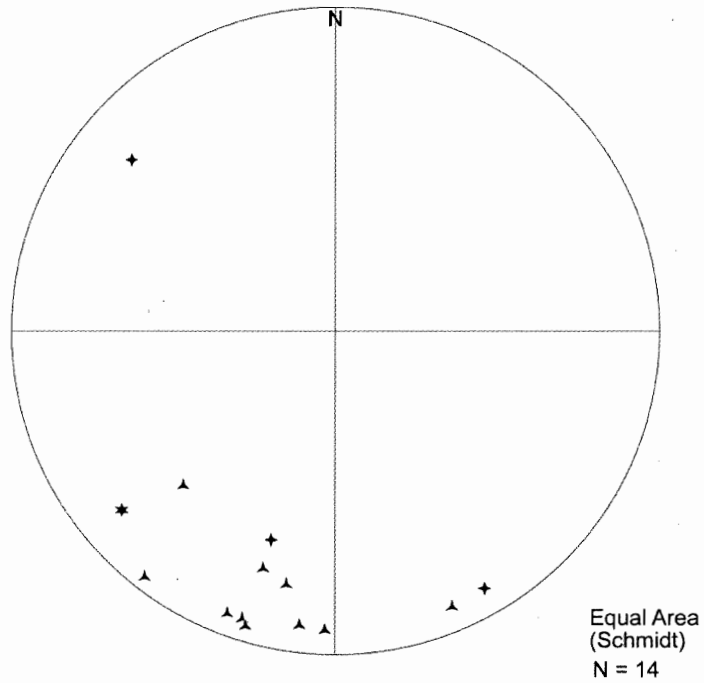
Group 1 / Area 2: Lineations

Figure 4.27: Lineations for the eastern Chekha formation (Group 1/Area 2). Note that they follow the different trend as in the areas to the west (Figure 4.23).

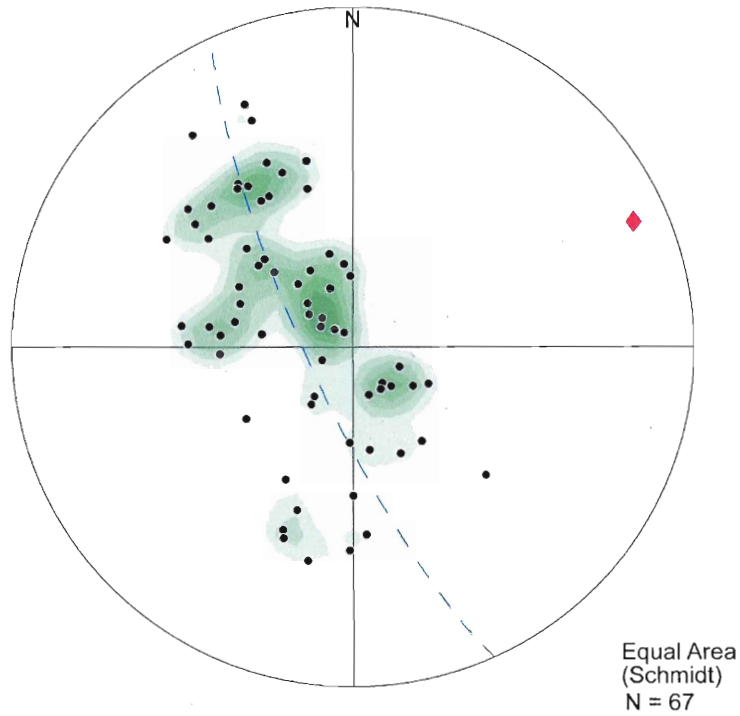
Group 3: Main Foliation

Figure 4.28: S_f for the Tethyan Sequence (Group 3). There is quite a bit of scatter in the data, but the general trend is to the NE, as it was for the NE-GHS (Figures 4.15 & 4.18).

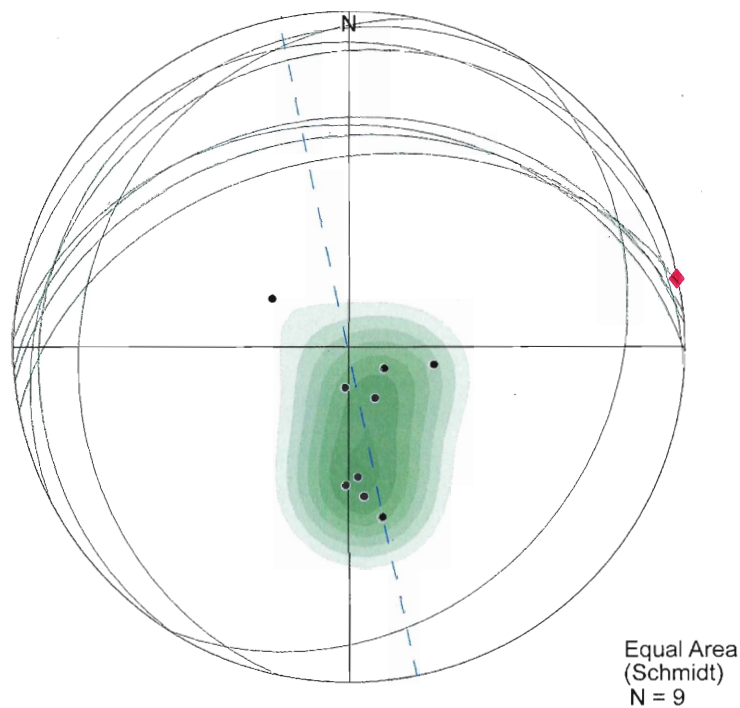
Group 3: Sedimentary Bedding

Figure 4.29: S_s for the Tethyan sequence (Group 3). The bedding shows the same trend as the S_f (Figure 4.28).

Group 3: Lineations

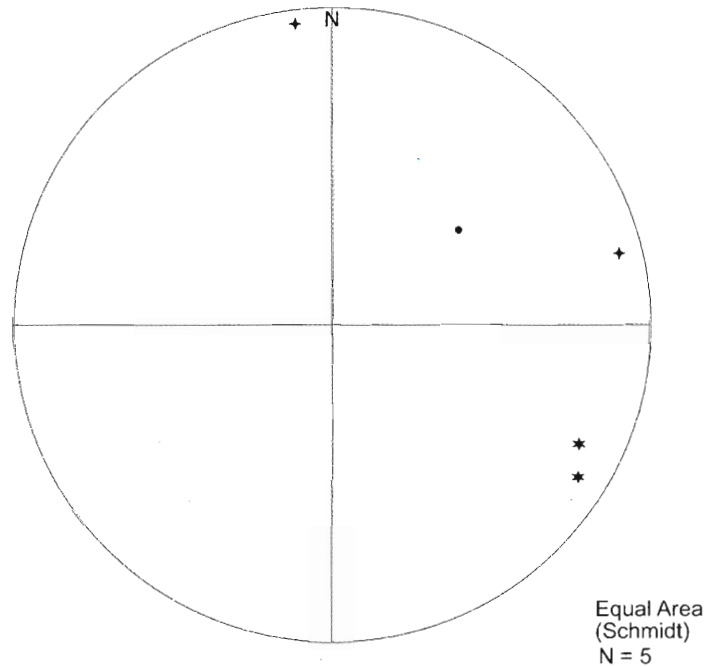


Figure 4.30: Lineations for the Tethyan sequence (Group 3). There were not many measurements, and not enough to notice any sort of trend.

Group 4: Main Foliation

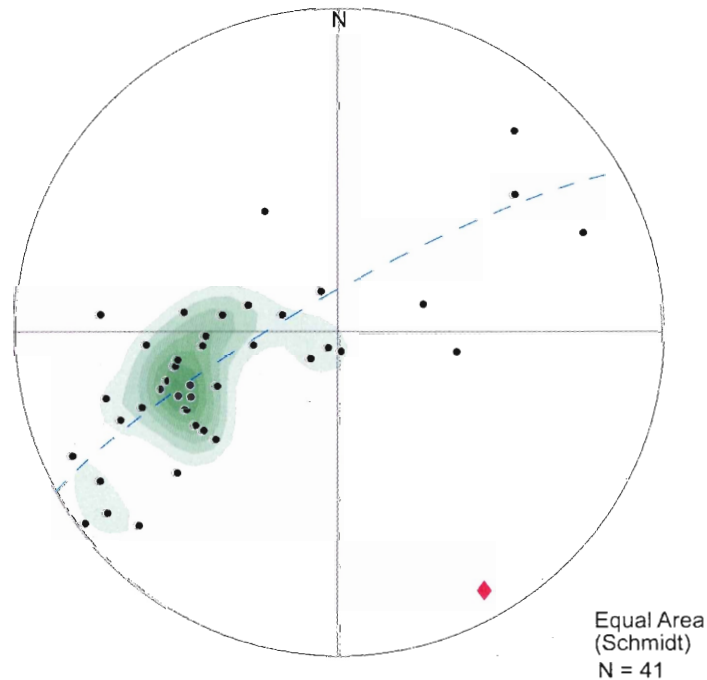


Figure 4.31: S_f for the boundary between leucogranite and the Chekha formation in the west (Figure 4.2). Since this is a contact, the measurements are more complex, and there is more scatter in the data. The scatter is provoked either by intrusion into existing foliation (dykes observed cutting the main foliation), or by faulting along the Lingshi fault (Figure 4.36).

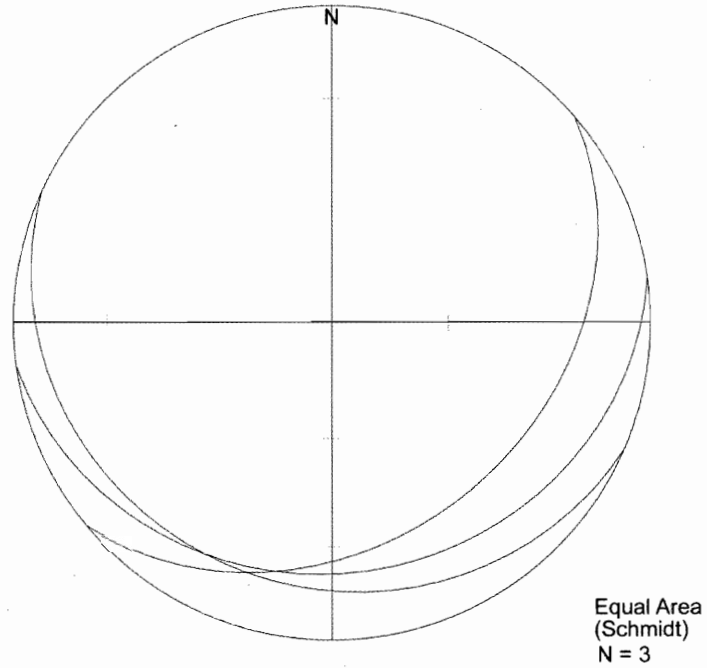
Group 4: Axial Planes

Figure 4.32: Sap for the same contact between leucogranite and the Chekha formation (As in Figure 4.31).

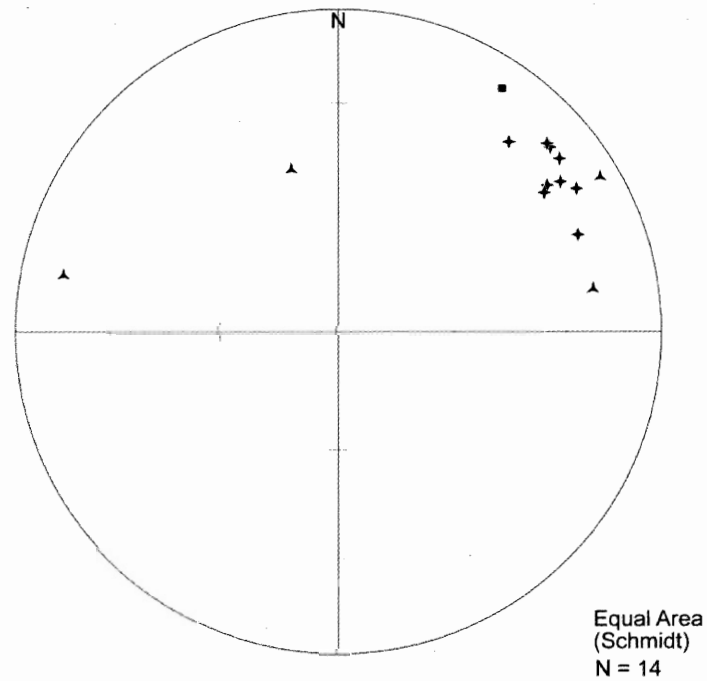
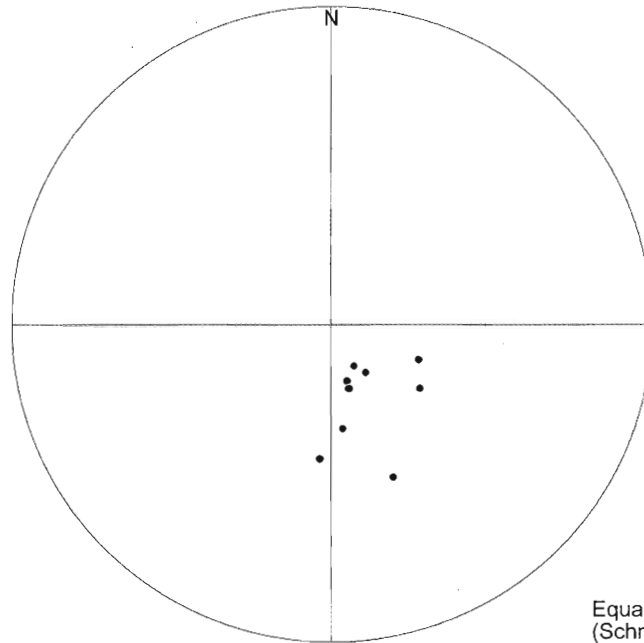
Group 4: Lineations

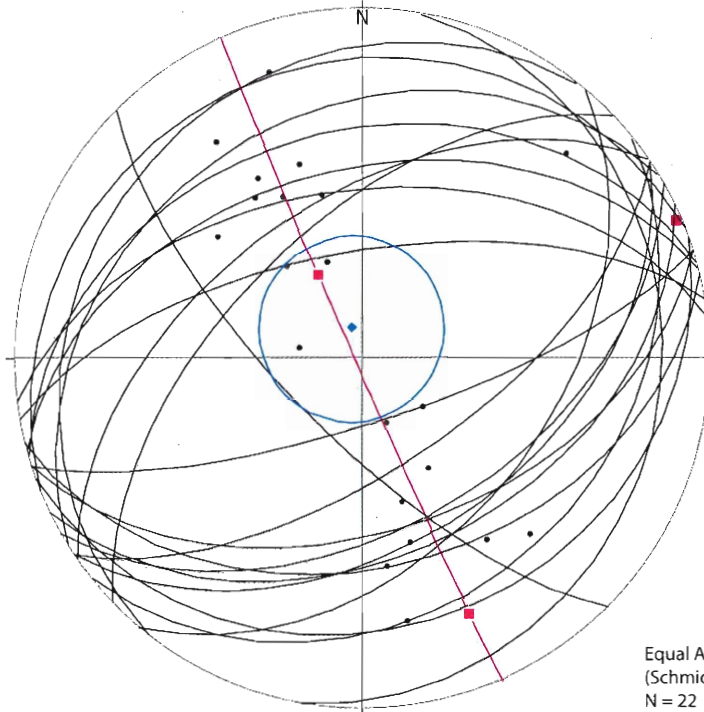
Figure 4.33: Lineations for the same contact between the leucogranite and the Chekha Formation (As in Figure 4.31).

Group 2 / Area 4b: 2nd Foliation

Equal Area
(Schmidt)
N = 9

Figure 4.34: *Sf2* for the NE-GHS (Group 2/Area 4b). This foliation is related to a later tectonic event, most likely a result of movement along the STD (Chakungal, 2006).

Group 2 / Area 4b & c: Shear Bands



Equal Area
(Schmidt)
N = 22

Figure 4.35: Conjugate *Ssb* for the NE-GHS (Group 2/Areas 4b & 4c). One set dips to the NW, with NW directed shearing. The other dips to the south, with SE directed shear sense. The NW dipping set are parallel to the *Sf2* observed in the same area (Figure 4.34).

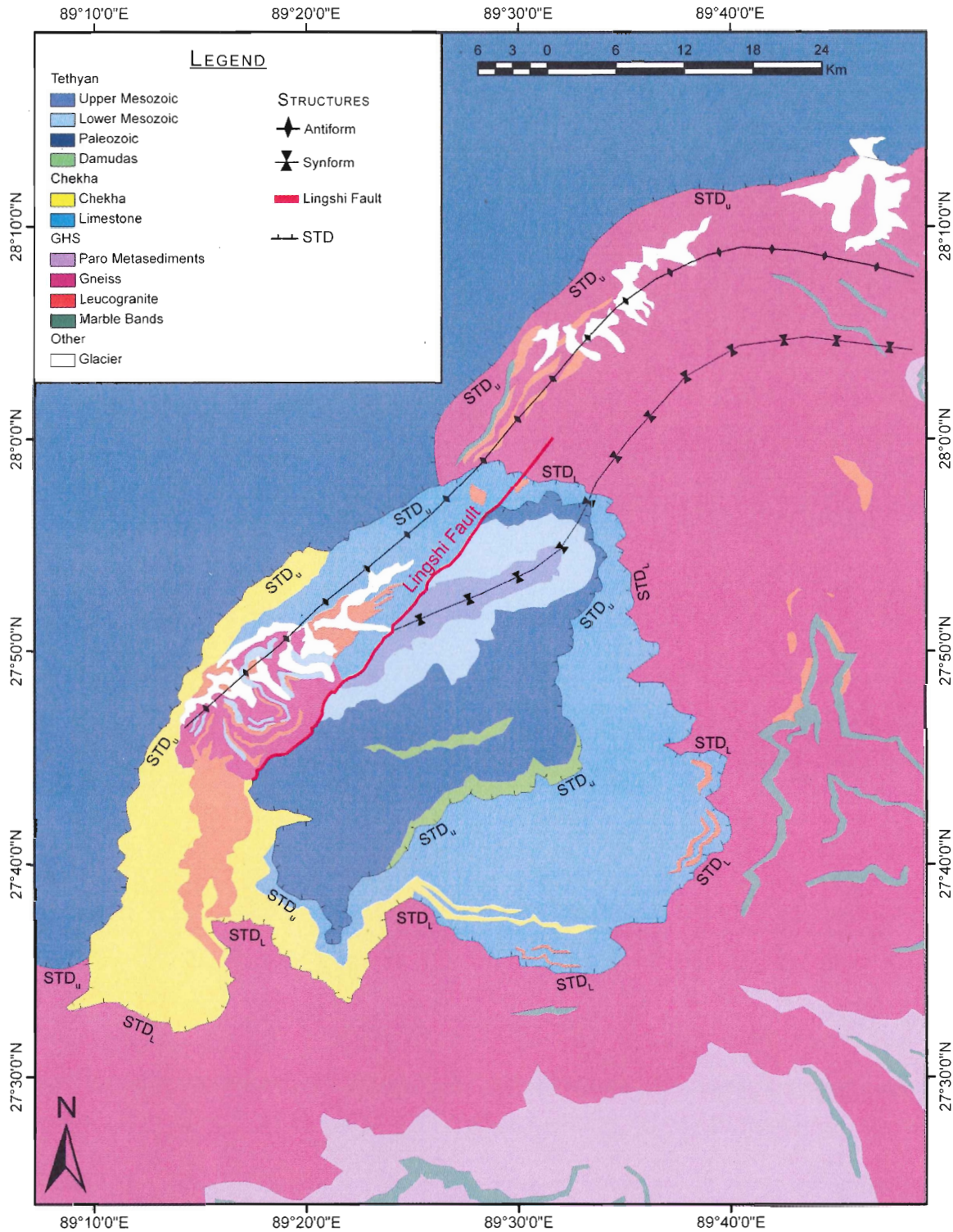


Figure 4.36: Structural map of the Lingshi Klippe. The main contact between the GHS and the Chekha is indicated as STD_L (Lower STD). The contact between the Chekha and the TSS is indicated as STD_U (Upper STD). The traces of the axial planes of the antiform and synform are indicated, as well as the Lingshi Fault.

4.4 SUMMARY OF STRUCTURAL ANALYSIS

This study has revealed the existence of large, open, upright folds affecting the main foliation and bedding of the area. The folds were formed at a later stage of deformation; however the exact mechanism is still unknown. These folds trend along the entire Bhutan Himalaya, however, they are highly non-cylindrical. The fold axes plunge in opposing directions, giving rise to dome-and-basin structures. The trend of the fold hinges is usually parallel to the trend of the orogen (i.e. E-W), but in Bhutan the folds are bent to a NNE-SSW orientation. The origin of this bend is not yet well explained, but may be related to the formation of the Yadong-Gulu graben to the west of the Lingshi Klippe (Hauck et al., 1998; Wu et al., 1998). The field observations and structural analysis suggest that the lineations are largely related to the main foliation, and therefore have been folded as well. Additionally, there is an even younger stage of deformation observed in the rocks in the form of the conjugate S_{sb} and coincident S_{f2} features. Since these features remain relatively undeformed by the regional folding they probably occurred after or during late-stage folding. It is suggested that these structures formed as a result of N-NW shearing and vertical shortening along the STD and may be additionally related to the leucogranite bodies at the top of the GHS (Chakungal, 2006). At the contact of the leucogranites and the Chekha formation in the west (Group 4; Figure 4.2) is the second zone of younger deformation, the contact between the Chekha formation and the GHS in the west. Here, it is clear that the main foliation has been intruded by the leucogranite dykes.

The separate analysis of the three litho-tectonic units (GHS, Chekha, TSS; Sections 4.1 - 4.3) shows that the statistical fold axes define a complex, gentle fold structure, which varies regionally and within each unit. This study has allowed the construction of the local orientation of the fold axes and axial planes. This will ultimately facilitate the further construction of

appropriately oriented cross-sections (perpendicular to the trend of the structures) across the Lingshi Syncline for the purpose of future tectonic studies (e.g. D. Kellett, Ph. D. Thesis).

CHAPTER 5

5.0 CONCLUSION

There are three aspects of this thesis: ASTER analysis (Chapter 2), the construction of a GIS database (Chapter 3) and the structural analysis of field measurements (Chapter 4). Each portion contributes to the overall understanding of the Lingshi Syncline of Bhutan. The ASTER data allows us to map the lithology of the region, the GIS database gives crucial field information for ground-truthing and the detailed structural analysis tells us something about the deformation of the units. The end result is a map of the region which has been improved from the earlier versions. In addition, the technique which has been developed here for mapping lithology can be applied to other areas in the Himalayas which remain incompletely mapped due to their inaccessibility.

5.1 ASTER ANALYSIS

During the course of this study, we were able to develop and test a new technique for determining the lithology of remote areas. Since the ASTER instrument is a relatively new addition to the world of remote sensing, and it has never been applied in Bhutan, the best approach to processing the images for lithological mapping was still quite undetermined. Thus, our analytical methods were obtained for the most part through a trial-and-error process of experimentation with several different techniques. For the purposes of this project, three different methods using ASTER were examined to remotely map lithology. The cluster method was found to be prone to topographical and solar angle variations. This method may be more applicable in areas of flatter topography, and with less vegetation. The method may also prove to be more useful if used in conjunction with a supervised classification procedure; however,

further experimentation will be required to determine this. The PCA (principal component analysis) did not prove to be spectrally discriminative for this data set, and was not explored further. The most efficient method found was the band ratio technique introduced by Perry (2003) and first proposed by Watts et al. (2005) for mapping in the Himalayas. In the future, more sophisticated methods such as a supervised classification could be performed, in order to further refine the map (Section 2.1.4). In addition, measuring the spectral responses in the laboratory of samples taken specifically from a study area and applying the actual sample characteristics to the band-ratio technique could facilitate a more precise identification of the distribution of the sampled lithologies.

Using the band ratio technique, we were able to distinguish between some of the lithologies in the study area. Some of the distinct lithological units were difficult to separate from each other (i.e. the Upper Mesozoic and the Paleozoic TSS carbonates from the Chekha carbonates). The cause could be lack of outcrop in some cases (some lithologies may be more prone to weathering or alteration than others), or spectral similarity to the other units. For example, carbonates are common in several of the units in the klippe, thus the boundaries between these units were very difficult to map precisely. In addition, due to permanent snow and vegetation cover, some of the boundaries cannot be fully defined. However, the technique enables researchers to map areas that were previously inaccessible for field work. Also, due to the wide range of bands to choose from, ASTER data give a level of detail that is not attainable from the human visual range. The use of ASTER imagery has proved to be an invaluable addition to the geological map of this region, and it may also be useful in similar areas. Using the same procedure determined through testing during our study, the Himalayan research group at Dalhousie will apply the technique to the remainder of Bhutan, Sikkim, and perhaps other

countries in the Himalayas as well. Since the procedure has been standardized here, it will make future study more effective and efficient.

Overall, mapping using ASTER data was an interesting and educational process. Initially, problems were encountered with the amount of vegetation present in the image, and interpreting the band-ratios for this study area. Additional ratios were experimented with in order to find a combination that would work well for these lithologies. Consequently, the procedure should now prove to be quite useful for other field areas as well. Nevertheless, some of the issues that were found during the mapping mean that some areas will prove to be unsuitable for mapping using ASTER data. A set of criteria was established to determine the suitability of a given area for ASTER data analysis. The area should:

- Be relatively arid - this will increase the chances that the area will be free from snow, vegetation and clouds
- contain extensive outcrop that is visible from space
- the area should have some ground-truthing capability, or a fairly current geological map available - ASTER imagery will only differentiate between different minerals, the mineralogical compositions of the rocks present should be known
- be a remote location to avoid interference from urban areas (smog, cloud cover and land cover could affect the results) – although ASTER imagery could potentially also be used to map sparsely populated accessible regions more efficiently than field mapping
- have substantial differences in mineralogy between the separate lithological units so that they can be differentiated based on spectral reflectance characteristics

Using these criteria, suitable areas can be chosen and mapped using ASTER band ratios with the procedure outlined in Appendix I. The technique can be used to make mapping more efficient and to determine the geology of inaccessible, remote locations.

5.2 GIS DATABASE

The GIS database created for use during this project compiled data for the whole of Bhutan. As subsequent areas are visited, the database will be added to and expanded. This database now forms a useful, standardized, categorized catalogue of all geological information available from Bhutan. The database is especially functional as an organizational tool as the data now have locations and can be displayed together on a map. There have also been a large number of samples gathered from the various field expeditions, and this database also keeps track of the analyses performed on each sample, and provides important searchable information for each sample. It is also possible to search with complex queries to display only desired information or sub-sets of certain data types. The information available can be used to construct cross-sections, for structural analyses, locate specific samples, locate which samples have been analysed, and refine the geological contacts. The database constructed here provides a very functional tool to be used in future study of Bhutan.

5.3 STRUCTURAL ANALYSIS

It is one thing to map the lithology of the study area, but it is also important to understand the relationship between each of the units. This task is facilitated by the statistical analysis of the structures measured in the field. Additionally, the analysis condensed the available data into a more concise format from which trends could be derived. This makes understanding and

constructing the regional structures easier and more accurate. Since the gathered data had never been analysed in this way before, it offers valuable insight into the nature of deformation in this area. The structural analysis revealed the precise trends of the folding which have affected the region. We were able to successfully separate the data into areas of structural homogeneity, and map the variation in trend of fold axis throughout a large area, and at different structural levels. The study confirmed the presence of the large syncline which comprises the Lingshi Klippe, along with the anticline pair to the north and uncovered further information on the shape and geometry of the folds. A younger stage of deformation was also discovered due to presence of several structures that were apparently not folded. The structural trends can now be used to construct cross-sections and perform further structural analyses in other studies.

5.4 FUTURE WORK

During the course of this study, we were able to contribute to the understanding of the processes needed for mapping using ASTER data in Bhutan and other areas of the Himalayas. The information was successfully applied to another area in Sikkim, proving the usefulness of the technique. However, the procedure can still be refined. Future useful studies may involve measuring spectral characteristics of the rock samples from the study area to refine the band-ratios used for mapping. Also, potential future expeditions to the locations mapped can assess the accuracy of the mapping technique and any problems that may be present themselves can be resolved. Supplementary ASTER images can be acquired and processed to further refine the geological contacts. This will help to further refine the geological boundaries and expand the study areas. Eventually, it is desired to have a complete current geological map for Bhutan and Sikkim, which has been digitized, geo-referenced and updated with more recent geological maps

of smaller areas by Dalhousie or other research groups. Now that the data and processes have finally been computerized, the Dalhousie Himalayan research group has truly been modernized for 21st century geology.

REFERENCES

- Abrams, M. 2000. The advanced spaceborne thermal emission and reflection radiometer (ASTER): Data products for the high spatial resolution imager on NASA's terra platform. *International Journal of Remote Sensing*, **21 (5)**: 847-859.
- Abrams, M., Hook, S., and Ramachandran, B. ASTER users handbook, 3rd ed. Jet Propulsion Laboratory, Pasadena, CA, USA.
- Abrams, M., and Hook, S.J. 1995. Simulated ASTER data for geologic studies. *IEEE Transactions on Geoscience and Remote Sensing*, **33 (3)**: 692-699.
- Aichison, J. C., Ali, J. R., and Davis, A. M. 2007. When and where did India and Asia collide? *Journal of Geophysical Research*, **112(B05423)**: 1-19.
- Beaumont, C., Jamieson, R.A., Nguyen, M.H. and Lee, B. 2001. Himalayan tectonics explained by extrusion of a low-viscosity crustal channel coupled to a focused surface denudation. *Nature*, **414**: 738-742.
- Beaumont, C., Jamieson, R.A., Nguyen, M.H., and Medvedev, S. 2004. Crustal channel flows: 1. numerical models with applications to the tectonics of the Himalayan-Tibetan orogen. *Journal of Geophysical Research*, **109**: 1-29.
- Beaumont, C., Nguyen, M.H., Jamieson, R.A., and Ellis, S. 2006. Crustal flow models in large hot orogens. In *Channel flow, ductile extrusion and exhumation in continental collision zones*. Edited by R. D. Law, M. P. Searle and L. Godin. Geological Society, London, Special Publication, **268**. pp. 91-145.
- Bhargava, O.N. 1995. The Bhutan Himalaya: a geological account. In: *Geological Survey of India, Special Publication*, **39**. pp. 245.
- Bilham, R., Larson, K., Freymueller, J., and Project Idylhim members. 1997. GPS measurements of present-day convergence across the Nepal Himalaya. *Nature*, **386 (6)**: 61-64.
- Bookhagen, B., Thiede, R. C., and Strecker, M. R. 2005. Abnormal Monsoon Years (AMVs) and their control on erosion and sediment flux in the high, arid northwest Himalaya. *Earth and Planetary Science Letters*, **231**: 131-146.

- Brunel, M., Dominguez, S., and Mascle, G. 2005. The formation of the Himalayas. In Himalayas (geological aspects), Volume 3. Edited by P. S. Sakalani, Prof. Satish Serial Publishing House, India. pp. 1-17.
- Campbell, J. B. 2007. Introduction to remote sensing. 4th ed. New York-London: The Guilford Press.
- Carosi, R., Montomoli, C., Rubatto, D., and Visona, D. 2006. Normal sense shear zone in the core of the higher Himalayan crystallines (Bhutan Himalaya): Evidence for extrusion? In Channel flow, ductile extrusion and exhumation in continental collision zones. Edited by R. D. Law, M. P. Searle and L. Godin. Geological Society, London, Special Publication, **268**. pp. 425-444.
- Catlos, E. J., Dubey, C. S., Harrison, T. M., and Edwards, M. A. 2004. Late Miocene movement within the Himalayan Main Central Thrust shear zone, Sikkim, north-east India. *Journal of Metamorphic Geology*, **22**: 207-226.
- Chakungal, J. 2006. Geochemistry and metamorphism of metabasites and spatial variation of P-T paths across the Bhutan Himalaya: Implications for the exhumation of the Greater Himalayan Sequence. Ph. D. thesis, Department of Earth Sciences, Dalhousie University, Halifax, N.S.
- Cheeny, R.F. 1983. Statistical methods in geology for field and lab decisions. George Allen & Unwin, London. pp. 169.
- Daniel, C.G., Hollister, L.S., Parrish, R.R., and Grujic, D. 2003. Exhumation of the Main Central Thrust from lower crustal depths, eastern Bhutan Himalaya. *Journal of Metamorphic Geology*, **21**: 317-334.
- Davidson, C., Grujic, D., Hollister, L.S., and Schmid, S. 1997. Metamorphic reactions related to decompression and synkinematic intrusion of leucogranite, high Himalayan crystallines, Bhutan. *Journal of Metamorphic Geology*, **15**: 593-612.
- DeCelles, P. G., Gehrels, G. E., Quade, J., LaReau, B., and Spurlin, M. 2000. Tectonic implications of U-Pb zircon ages of the Himalayan orogenic belt in Nepal. *Science*, **288(5465)**: 497-499.
- Drupka, D., Velasco, A.A., Doser, D.I. 2006. Seismicity in the Kingdom of Bhutan (1937-2003): Evidence for crustal transcurrent deformation. *Journal of Geophysical Research*, **111(B6)**: 1-14.

- Edwards, M.A., Kidd, W.S.F., Li, J., Yue, Y., and Clark, M. 1996. Multi-stage development of the southern Tibet detachment system near Khula Kangri, new data from Gonto La. *Tectonophysics*, **260**: 1-19.
- Edwards, M.A., and Harrison, T.M. 1997. When did the roof collapse? Late Miocene north-south extension in the high Himalayas revealed by Th-Pb monazite dating of the Khula Kangri granite. *Geology*, **25(6)**: 543-546.
- Edwards, M.A., Pêcher, A., Kidd, W.S.F., Burchfiel, B.C., and Royden, L.H. 1999. Southern Tibet detachment system at Khula Kangri, eastern Himalaya: A large-area, shallow detachment stretching into Bhutan? *The Journal of Geology*, **107**: 623-631.
- EOS Data Gateway. Land Processes Distributed Active Archive Center, Version 3.6.5. <http://edcimswww.cr.usgs.gov/pub/imswelcome/>.
- ERSDAC. 2005. ASTER User's Guide, Part I, General: Version 4.0. www.science.aster.ersdac.or.jp/en/documnts/users_guide/.
- ERSDAC. 2007. ASTER User's Guide, Part II, Level 1 Data Products: Version 5.1. www.science.aster.ersdac.or.jp/en/documnts/users_guide/.
- Gansser, A. 1964. *Geology of the Himalayas*. Wiley, Interscience Publishers, London. pp. 289.
- Gansser, A. 1983. *Geology of the Bhutan Himalaya*. Birkhäuser Verlag, Basel-Boston-Stuttgart.
- Godin, L., Grujic, D., Law, R.D., and Searle, M.P. 2006. Channel flow, ductile extrusion and exhumation in continental collision zones: An introduction. In *Channel flow, ductile extrusion and exhumation in continental collision zones*. Edited by R. D. Law, M. P. Searle and L. Godin. Geological Society, London, Special Publication, **268**. pp. 1-23.
- Gomez, C., Delacourt, C., Allemand, P., Ledru, P., and Wackerle, R. 2005. Using ASTER remote sensing data set for geological mapping, in Namibia. *Physics and Chemistry of the Earth*, **30**: 97-108.
- Grujic, D., Casey, M., Davidson, C., Hollister, L.S., Kündig, R., Pavlis, T., and Schmid, S. 1996. Ductile extrusion of the higher Himalayan crystalline in Bhutan: Evidence from quartz microfabrics. *Tectonophysics*, **260**: 21-43.
- Grujic, D., Hollister, L.S., and Parrish, R.R. 2002. Himalayan metamorphic sequence as an orogenic channel: Insight from Bhutan. *Earth and Planetary Science Letters*, **198**: 177-191.

- Grujic, D., Coutand, I., Bookhagen, B., Bonnet, S., Blythe, A., and Duncan, C. 2006. Climatic forcing of erosion, landscape and tectonics in the Bhutan Himalaya. *Geology*, **34**: 801–804.
- Guillot, S., Garzanti, E., Baratoux, D., Marquer, D., Mahéo, G., and de Sigoyer, J. 2003. Reconstructing the total shortening history of the NW Himalaya. *Geochemistry, Geophysics, Geosystems*, **4(7)**: 1-50.
- Guillot, S., Replumaz, A., Hattori, K. H., and Strzeczynski, P. 2007. Initial geometry of western Himalaya and ultrahigh-pressure metamorphic evolution. *Journal of Asian Earth Sciences*, **30**: 557-564.
- Harrison, M. T. 2006. Did the Himalayan Crystallines extrude partially molten from beneath the Tibetan Plateau? In *Channel flow, ductile extrusion and exhumation in continental collision zones*. Edited by R. D. Law, M. P. Searle and L. Godin. Geological Society, London, Special Publication, **268**. pp. 237–254.
- Hauck, M. L., Nelson, K. D., Brown, L. D., Zhao, W. & Ross, A. R. 1998. Crustal structure of the Himalayan orogen at ~90° east longitude from Project INDEPTH deep reflection profiles. *Tectonics*, **17(4)**: 481-500.
- Herring, D. NASA's Earth Observing System: EOS AM-1 brochure.
<http://terra.nasa.gov/Brochure/brochure.pdf>
- Hodges, K.V., Hubbard, M.S., Silverberg, D.S., Treloar, P.J., and Mohan, A. 1988. Metamorphic constraints on the thermal evolution of the central Himalayan orogen [and discussion]. *Philosophical Transactions of the Royal Society of London. Series A, Mathematical and Physical Sciences*, **326 (1589)**: 257-280.
- Hodges, K.V. 2000. Overview: Tectonics of the Himalayas and southern Tibet from two perspectives. *Geological Society of America Bulletin*, **112 (3)**: 324-350.
- Hollister, L.S., and Grujic, D. 2006. Pulsed channel flow in Bhutan. In *Channel flow, ductile extrusion and exhumation in continental collision zones*. Edited by R. D. Law, M. P. Searle and L. Godin. Geological Society, London, Special Publication, **268**. pp. 415-423.
- Jamieson, R. A., Beaumont, C., Medvedev, S., and Nguyen, M.H. 2004. Crustal channel flows: 2. numerical models with implications for metamorphism in the Himalayan-Tibetan orogen. *Journal of Geophysical Research*, **109**: 1-24.
- Jamieson, R. A., C. Beaumont, C., Nguyen, M.H., and Grujic, D. 2006. Provenance of the Greater Himalayan Sequence and associated rocks: Predictions of channel flow models. In *Channel flow, ductile extrusion and exhumation in continental collision zones*. Edited by R.

- D. Law, M. P. Searle and L. Godin. Geological Society, London, Special Publication, **268**. pp. 165-182.
- Kellett, D. A., Grujic, D., and Warren, C. 2008. Testing predictive models of collisional orogenesis: a case study from the Himalayan orogen. In: Geological Association of Canada annual meeting, Québec City.
- Klootwijk, C.T., Gee, J.S., Peirce, J.W., Smith, G.M., and McFadden, P.L. 1992. An early India-Asia contact: Paleomagnetic constraints from Ninetyeast Ridge, ODP Leg 121. *Geology*, **20**: 395-398.
- Kohn, M. J. 2008. P-T-t data from central Nepal support critical taper and repudiate large-scale channel flow of the Greater Himalayan Sequence. *GSA Bulletin*, **120(3/4)**: 259–273.
- Leech, M.L., Singh, S., Jain, A.K., Klemperer, S.L., and Manickavasagam, R.M. 2005. The onset of India-Asia continental collision: Early, steep subduction required by the timing of UHP metamorphism in the western Himalaya. *Earth and Planetary Science Letters*, **234**: 83-97.
- Meyer, M.C., Wiesmayr, G., Brauner, M., Häusler, H., and Wangda, D. 2006. Active tectonics in eastern Lunana (NW Bhutan): Implications for the seismic and glacial hazard potential of the Bhutan Himalaya. *Tectonics*, **25(1)**: 21.
- Najman, Y. 2006. The detrital record of orogenesis: A review of approaches and techniques used the in the Himalayan sedimentary basins. *Earth-Science Reviews*, **74**: 1-72.
- Nelson, K.D., Zhao, W., Brown, L.D., Kuo, J., Che, J., Liu, X., Klemperer, S.L., et al. 1996. Partially molten middle crust beneath southern Tibet: Synthesis of project INDEPTH results. *Science, New Series*, **274 (5293)**: 1684-1688.
- Parrish, R.R., Warren, C., Searle, M., Grujic, D., and Brown, R. 2004. The chronology of exhumation/extrusion in the Bhutan Himalaya and the Oman Mountains during contrasting tectonic events – relevance to mechanics of channel flow. Channel Flow Conference, Royal Society, December 2004.
- Ramsay, J.G., and Huber, M.L. 1987. The techniques of modern structural geology. Volume 2: Folds and Fractures. Academic Press.
- Richards, A., Parrish, R.R., Harris, N., Argles, T., and Zhang, L. 2006. Correlation of lithotectonic units across the eastern Himalaya, Bhutan. *Geology*, **34 (5)**: 341-344.

- Ritchie, L. 2004. Tectonic history of the sole and roof of the Greater Himalayan Sequence: Structural and metamorphic observations of garnet-staurolite schists from the Bhutan Himalaya. Honours Thesis, Department of Earth Sciences, Dalhousie University, Halifax, N.S.
- Rowley, D.B. 1996. Age of initiation of collision between India and Asia: A review of stratigraphic data. *Earth and Planetary Science Letters*, **145**: 1-13.
- Searle, M. P., Simpson, R.L., Law, R.D., Parrish, R.R., and Waters, D.J. 2003. The structural geometry, metamorphic and magmatic evolution of the Everest massif, High Himalaya of Nepal-south Tibet. *Journal of the Geological Society, London*, **160**: 345-366.
- Stesky, R.M. 1996. SpheriStat™ 2 for Windows® 3.1 User's Manual. Pangaea Scientific, Brockville, ON, CA.
- Swapp, S.M., and Hollister, L.S. 1991. Inverted metamorphism within the Tibetan slab of Bhutan: Evidence for a tectonically transported heat-source. *Canadian Mineralogist*, **29**: 1019-1041.
- Tapponnier, P., Xu, Z., Roger, F., Meyer, B., Arnaud, N., Wittlinger, G, and Jingsui, Y. 2001. Oblique stepwise rise and growth of the Tibet Plateau *Science*, **294(5547)**: 1671-1677.
- Vincent, R.K. 1997. Fundamentals of geological and environmental remote sensing. Prentice-Hall, Inc., Upper Saddle River, N.J.
- Watts, D.R., Harris, N.B.W, and the 2002 NASA GLENN SOARS Working Group. 2005. Mapping granite and gneiss in domes along the north Himalayan antiform with ASTER SWIR band ratios. *Geological Society of America Bulletin*, **117 (7/8)**: 879-886.
- Webb, A. A. G., Yin, A., Harrison, M. T., C el erier, J., and Burgers, W. P. 2007. The leading edge of the Greater Himalayan Crystalline complex revealed in the NW Indian Himalaya: Implications for the evolution of the Himalayan orogen. *Geology*, **35(10)**: 955-958.
- Wesnousky, S.G., Kumar, S., Mohindra, R., and Thakur, V.C. 1999. Uplift and convergence along the Himalayan frontal thrust of India. *Tectonics*, **18 (6)**: 967-976.
- Wu, C., Nelson, K.D., Wortman, G., Samson, S.D., Yue, Y., Li, J., Kidd, W.S.F. & Edwards M.A. 1998. Yadong cross structure and South Tibetan detachment in the east central Himalaya (89° - 90° E). *Tectonics*, **17(1)**: 28-45.
- Yin, A., and Harrison, T. M. 2000. Geologic evolution of the Himalayan-Tibetan orogen. *Annual Review of Earth and Planetary Sciences*, **28**: 211-280

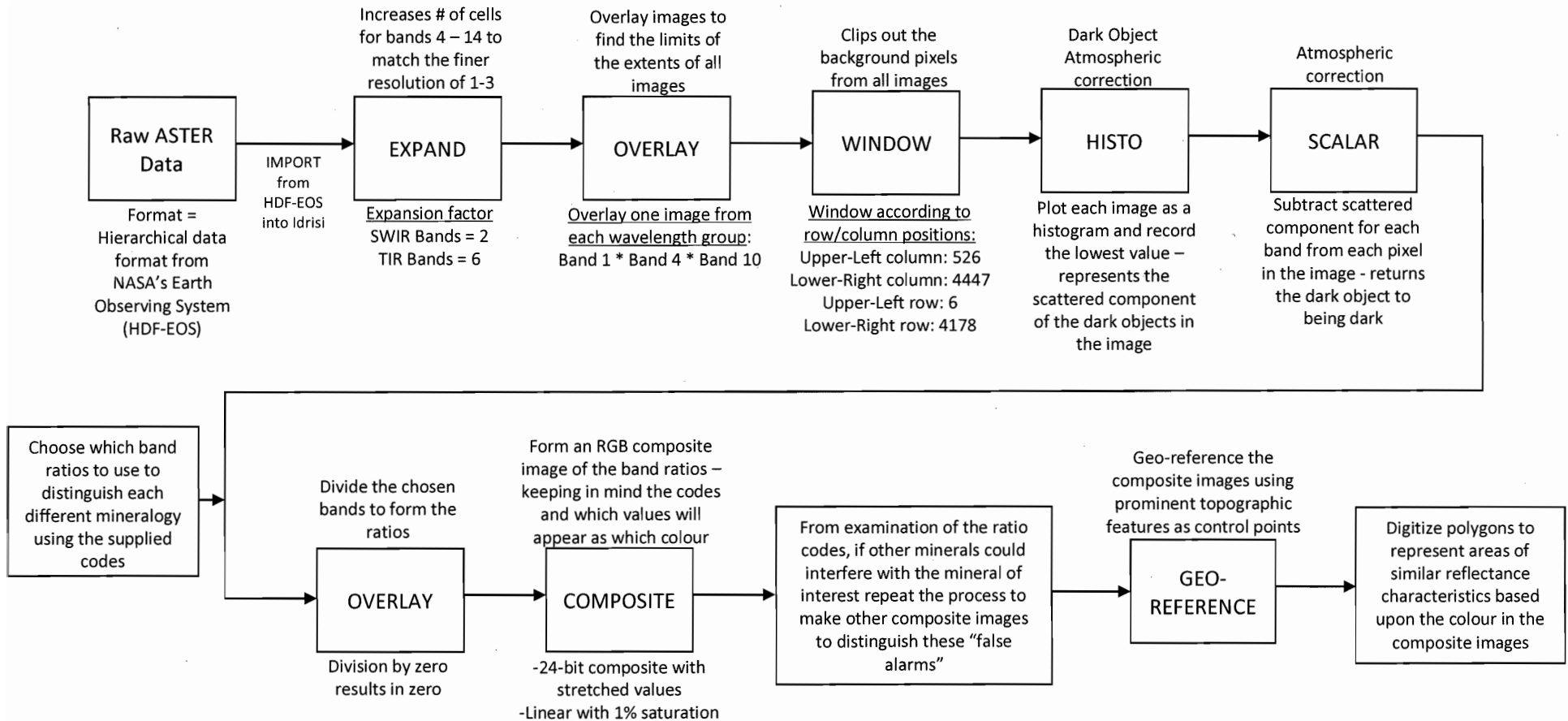
- Yin, A. 2006. Cenozoic tectonic evolution of the Himalayan orogen as constrained by along-strike variation of structural geometry, exhumation history, and foreland sedimentation. *Earth-Science Reviews*, **76**: 1-131.
- Zhang, P.Z., Shen, Z., Wang, M., Gan, W., Bürgmann, R., Molnar, P., Wang, Q., et al. 2004. Continuous deformation of the Tibetan plateau from global positioning system data. *Geology*, **32 (9)**: 809-812.

IV. TABLE OF SOFTWARE PROGRAMS USED

Software	Provider	Version
GoogleEarth™	Google	4.2
ArcMAP™ License Type: ArcView	ESRI®	9.1 Build: 766
Idrisi Kilimanjaro	Clark Labs	14.02
SpheriStat™	Pangaea Scientific	2.1
GeoMapApp©	Marine Geoscience Data System	1.6.4

APPENDIX I: CARTOGRAPHIC MODEL

The exact steps taken to process the ASTER images are outlined here:



To make vegetation and snow overlays:

